



# BRNO UNIVERSITY OF TECHNOLOGY

VYSOKÉ UČENÍ TECHNICKÉ V BRNĚ

## FACULTY OF MECHANICAL ENGINEERING

FAKULTA STROJNÍHO INŽENÝRSTVÍ

## INSTITUTE OF PHYSICAL ENGINEERING

ÚSTAV FYZIKÁLNÍHO INŽENÝRSTVÍ

# PHASE-RESOLVED BRILLOUIN LIGHT SCATTERING: DEVELOPMENT AND APPLICATIONS

MĚŘENÍ FÁZE SPINOVÝCH VLN POMOCÍ BRILLOUINOVA ROZPTYLU SVĚTLA: VÝVOJ ZAŘÍZENÍ A JEHO APLIKACE

## MASTER'S THESIS

DIPLOMOVÁ PRÁCE

### AUTHOR

AUTOR PRÁCE

Bc. Ondřej Wojewoda

### SUPERVISOR

VEDOUCÍ PRÁCE

Ing. Michal Urbánek, Ph.D.

BRNO 2020



# Specification Master's Thesis

Department: Institute of Physical Engineering  
Student: **Bc. Ondřej Wojewoda**  
Study programme: Applied Sciences in Engineering  
Study field: Physical Engineering and Nanotechnology  
Supervisor: **Ing. Michal Urbánek, Ph.D.**  
Academic year: 2019/20

Pursuant to Act no. 111/1998 concerning universities and the BUT study and examination rules, you have been assigned the following topic by the institute director Master's Thesis:

## **Phase-resolved Brillouin light scattering: development and applications**

### **Concise characteristic of the task:**

Spin wave logic devices are promising candidates for low power data processing. Information can be written either in the amplitude or phase of the spin wave. To be able to engineer such devices, it is essential to measure these properties. With the classic micro BLS setup it is possible to measure only intensity of the spin waves. But if we add a reference signal with constant phase from an electro-optical modulator the full phase of the spin wave can be reconstructed.

### **Goals Master's Thesis:**

Perform literature search and describe current state of the art of BLS measurements.

Build and characterize a setup for phase resolved BLS measurement.

Prove the functionality of the setup with series of experiments.

### **Recommended bibliography:**

SEBASTIAN, Thomas, Katrin SCHULTHEISS, Björn OBRY, Burkard HILLEBRANDS a Helmut SCHULTHEISS. Micro-focused Brillouin light scattering: imaging spin waves at the nanoscale. *Frontiers in Physics* [online]. 2015, 3 [cit. 2019-10-31]. DOI: 10.3389/fphy.2015.00035. ISSN 2296-424X.

Deadline for submission Master's Thesis is given by the Schedule of the Academic year 2019/20

In Brno,

L. S.

---

prof. RNDr. Tomáš Šikola, CSc.  
Director of the Institute

---

doc. Ing. Jaroslav Katolický, Ph.D.  
FME dean

## Abstract

Spin waves have the potential to be used as a new platform for data transfer and processing as they can reach wavelengths in the nanometer range and frequencies in the terahertz range. To be able to design the spin-wave devices and logic circuits we need to be able to gather the information about spatial distribution of the spin-wave intensity and if possible, also their phase. This can be measured with the use of phase-resolved micro-Brillouin-light-scattering ( $\mu$ -BLS) setup. The presented work deals with extending the existing intensity resolved setup with the possibility to also acquire the spin-wave phase. The upgraded Brillouin light scattering setup is thoroughly described and its performance is characterized. The capabilities of the developed setup are demonstrated in the study of propagation of spin waves through a Néel domain wall. The acquired 2D spin-wave intensity maps reveal that spin-wave transmission through a domain wall is influenced by a topologically enforced circular Bloch line in the domain wall center and that the propagation regime depends on the spin-wave frequency. In the first regime, two spin-wave beams propagating around the circular Bloch line are formed, whereas in the second regime, spin waves propagate in a single central beam through the circular Bloch line. Phase-resolved  $\mu$ -BLS measurements reveal a phase shift upon transmission through the domain wall for both regimes. Micromagnetic modelling of the transmitted spin waves unveils a distortion of their phase fronts which needs to be taken into account when interpreting the measurements and designing potential devices. Moreover, we show, by means of micromagnetic simulations, that an external magnetic field can be used to move the circular Bloch line within the domain wall to manipulate spin-wave propagation.

## Abstrakt

Spinové vlny mají potenciál být použity jako nová platforma pro přenos a zpracování dat, protože mohou dosáhnout vlnových délek v rozsahu nanometrů a frekvencí v rozsahu terahertzů. K tomu, aby bylo možné navrhnout zařízení a logické obvody založené na spinových vlnách, je zapotřebí získat informace o prostorovém rozložení intenzity spinové vlny a pokud je to možné, také o jejich fázi. To lze měřit pomocí fázově rozlišeného fokusaného Brillouinova rozptylu světla ( $\mu$ -BLS). Předložená práce se zabývá rozšířením stávající optické sestavy o možnost měření fáze, kde doposud bylo možné měřit pouze intenzitu. Toto rozšíření sestavy je důkladně popsáno a charakterizováno. Schopnosti optické sestavy jsou demonstrovány ve studii šíření spinových vln skrz Néelovu doménovou stěnu. Získané 2D mapy intenzity spinových vln ukazují, že propagace přes doménovou stěnu je ovlivněna topologicky vynucenou kruhovou Blochovou čarou ve středu doménové stěny a že režim propagace závisí na frekvenci spinových vln. V prvním režimu propagace se vytvoří dva svazky spinových vln šířící se kolem kruhové Blochovy čáry, zatímco ve druhém režimu se spinové vlny šíří pouze středem. Fázově rozlišené  $\mu$ -BLS měření odhaluje fázový posun spinových vln pro oba režimy. Mikromagnetické modelování spinových vln ukazuje rozrušení jejich fázových vlnoploch, které je třeba brát v úvahu při interpretaci měření a navrhování potenciálních zařízení. Mikromagnetické simulace ukazují, že vnější magnetické pole může být použito k pohybu kruhové Blochovy čáry ve stěně domény, a tedy k manipulaci spinových vln.

## Keywords

magnonics, spin wave, light scattering, optical setup, Brillouin light scattering

**Klíčová slova**

magnonika, spinové vlny, rozptyl světla, optická sestava, Brillouinův rozptyl světla

WOJEWODA, Ondřej. *Phase-resolved Brillouin light scattering: development and applications*. Brno, 2020. 66 p. Master's thesis. Brno University of Technology. Faculty of Mechanical Engineering. Supervised by Michal URBÁNEK.

I hereby declare that I have written my master's thesis on the theme of *Phase-resolved Brillouin light scattering: development and applications* independently, under the guidance of the master's thesis supervisor, Ing. Michal Urbánek, Ph.D., and using the technical literature and other sources of information which are all properly quoted in the thesis and detailed in the list of literature at the end of the thesis.

.....  
Place and date

.....  
Bc. Ondřej Wojewoda

## ACKNOWLEDGMENT

I am really grateful to Dr. Michal Urbánek for excellent supervision, a lot of advice, technical help in the laboratory, and a lot of lessons (not only) in physics. He has had an exceptional daily interest in all research projects which I was part of. My thanks also go to Dr. Lukáš Flajšman, who taught me basics in spin waves, optics, and much more. I wish to be able to fulfill the same role for the next younger students. I am obliged to Marek Vaňatka, who introduced me to the field of magnetism. He also taught me a lot about scientific writing. I want to thank Igor Turčan for his comments on this thesis and creating good (procrastination) mood every morning during the few last days of writing. I would like to thank Dr. Michal Staňo for proofreading the thesis and his outstanding attention to detail and diligence. My thanks also goes to Libor Vojáček who proofread this thesis and taught me a lot of things not only about Arduino. I am also thankful to the rest of the magnetism group for making an ideal working environment and a lot of discussion during the coffee breaks. I am also grateful to my fellow students (Jakub Holobrádek, Andrej Tripský, Jan Tesař, Ivan Mohelský, Katarína Rovenská, and Tomáš Láznička) who shared the writing relating suffering during the few last days. I appreciate the knowledge and life-lessons which were given to me by Dr. Helmut Schultheiss. I am also thankful to Tobias Hula and the rest of the magnonic group in Helmholtz zentrum Dresden-Rosendorf for showing me different approaches in scientific life. I would especially point out Tillmann Weinhold, who helped me a lot not only with this thesis; Vielen Danken, Tillmann. My thanks also go to my girlfriend Michaela Chmelová for support and great understanding during work on this thesis. Mé největší díky ovšem směřují k mojí rodině, speciálně mým rodičům. Děkuji Vám, že jsem měl možnost naplno se věnovat tomu, co mě baví.

Bc. Ondřej Wojewoda

CzechNanoLab project LM2018110 funded by MEYS CR is gratefully acknowledged for the financial support of the measurements/sample fabrication at CEITEC Nano Research Infrastructure.

# Contents

<b>Introduction</b>	<b>1</b>
<b>1. Basics of micromagnetic theory and spin waves</b>	<b>3</b>
1.1. Energies in magnetism	3
1.1.1. Exchange energy	3
1.1.2. Zeeman energy	3
1.1.3. Dipolar energy	4
1.1.4. Anisotropy energy	4
1.2. Effective field	5
1.3. Magnetization dynamics	5
1.4. Ferromagnetic resonance	6
1.5. Spin waves	6
1.5.1. Group velocity and propagation length of spin waves	8
1.6. Materials used in spin-wave research	10
<b>2. Theory of light scattering</b>	<b>13</b>
2.1. Classical treatment	13
2.1.1. Rayleigh scattering	13
2.1.2. Mie scattering	14
2.1.3. Doppler shift of the scattered light	14
2.2. Quantum treatment	15
2.2.1. Quasi-elastic scattering	15
2.2.2. Raman scattering	16
2.2.3. Brillouin light scattering	16
Scattering on magnons	17
2.3. Interferometers for measuring BLS	18
2.3.1. Virtually imaged phased array Brillouin light scattering	18
Applications of VIPA BLS	19
2.3.2. Fabry-Perot Brillouin light scattering	20
Tandem Fabry-Perot interferometer	21
2.4. $k$ -resolved Brillouin light scattering	23
2.4.1. Tilting of sample approach	24
2.4.2. Large aperture approach	24
2.4.3. Applications of $k$ -resolved BLS	24
Material properties	24
Dispersion relation	25
DMI measurement	25
2.5. $\mu$ BLS	25
2.5.1. Applications of $\mu$ BLS	26

Spin-wave waveguide . . . . .	27
Magnonic crystals . . . . .	27
Guiding of spin waves . . . . .	27
Spin-wave splitters . . . . .	28
Spin-wave amplifiers . . . . .	28
Spin-wave sources . . . . .	28
2.6. Phase-resolved $\mu$ BLS . . . . .	29
2.6.1. Application of phase-resolved $\mu$ BLS . . . . .	32
Material characterization . . . . .	33
Phase of excited spin waves . . . . .	33
2.7. Time-resolved BLS . . . . .	34
2.7.1. Application of time-resolved $\mu$ BLS . . . . .	34
Group velocity . . . . .	34
Non-linear processes . . . . .	35
Bose-Einstein condensation . . . . .	35
<b>3. Construction and characterization of the phase-resolved BLS setup</b>	<b>37</b>
3.1. General overview . . . . .	37
3.2. Light source . . . . .	37
3.2.1. Faraday isolator . . . . .	38
3.2.2. Fabry-Perot etalon . . . . .	39
3.2.3. Adjusting of incident laser intensity . . . . .	39
3.3. Electro-optic modulator . . . . .	40
3.4. Microscope module . . . . .	41
3.4.1. Electromagnet . . . . .	41
3.5. Tandem-Fabry-Perot interferometer . . . . .	42
3.6. Verification of the setup . . . . .	43
<b>4. Propagation of spin waves through Neél domain wall</b>	<b>45</b>
4.1. Sample preparation . . . . .	45
4.2. Static characterization . . . . .	46
4.2.1. Stabilization of the domain wall . . . . .	46
4.2.2. Characterization of the type of the domain wall . . . . .	47
4.3. Dynamic characterization . . . . .	47
4.3.1. Thermally excited spin waves . . . . .	47
4.3.2. Propagation of coherent spin waves . . . . .	48
Dispersion measurement . . . . .	49
Frequency sweep . . . . .	49
Spatially-resolved BLS scans . . . . .	50
Phase-resolved linescans . . . . .	50
4.3.3. Micromagnetic simulations . . . . .	51
4.4. Displacement of the circular Bloch line . . . . .	53
<b>Conclusion</b>	<b>54</b>
<b>References</b>	<b>56</b>
<b>List of abbreviation and symbols</b>	<b>66</b>

<b>A. Matlab code for calculation of the dispersion relation</b>	<b>i</b>
<b>B. Group velocity and lifetime of spin waves</b>	<b>iii</b>
B.1. Group velocities of spin waves . . . . .	iii
B.2. Lifetime of spin waves . . . . .	iii
<b>C. Dependency of group velocity, lifetime, and frequency of spin waves     on thickness and external magnetic field</b>	<b>iv</b>
<b>D. Analytic modeling of phase resolved signals</b>	<b>vi</b>
D.1. Signal without thermal background . . . . .	vi
D.2. Signal with thermal background . . . . .	vi

# Introduction

Current computers are based on von Neumann's architecture [1], the principles of which have remained unchanged since its inception in 1945. Since the invention of the silicon chip, the density of transistors has been guided by Moore's law: the density of transistors on a silicon chip is doubled every two years [2]. However, this economic law is approaching its limits. Further increase in the density requires miniaturization of transistors down to the atomic scale [3, 4]. Such task is extremely challenging from the technical point of view.

Unconventional physical phenomena can be used to design new approaches to computation architecture, such as non-linear processes or non-reciprocal dispersion relations [5–8]. The spin-wave framework, provides these phenomena [9–11], while offering wavelength spanning from nanometers to millimeters and frequency range from gigahertz to terahertz. The non-linear regime is accessible even with relatively small power, and the dispersion dramatically changes in the dependence on the direction of the propagation [12, 13]. The typical energy of the spin-wave excitation is lower by several orders of magnitude when compared to current electric circuits. This allows us to design novel computation elements with low power consumption [14].

Spin waves were intensively studied since the previous century, and several applications in high-frequency electronics were developed [15]. Nevertheless, the majority of these studies used only one material - yttrium iron garnet. It is an insulator with low magnetic damping, but it is difficult to prepare. This makes it not ideal for applications. Nowadays, the interest in spin-wave research is moving towards metallic materials. These materials offer compatibility with the current technology and allow for easy nano-patterning of the magnetic structures. To investigate these nanostructures, the requirement for a versatile tool with sub-micrometer resolution occurs. For this purpose, the micro-Brillouin-light scattering was developed [16]. This technique allows for the investigation of the spatial distribution of the intensity and the phase of the spin waves, as well as allows time-resolved experiments.

This thesis describes the construction and characterization of a Brillouin light scattering setup with phase-resolved measurement capabilities. The setup is then used to study spin-wave propagation through the Néel domain wall.

The thesis consists of 4 chapters. The first chapter discusses the basic theory of magnetism and spin waves in order to lay sufficient foundations for the experimental work. The general law of dipole-exchange dispersion of spin waves in a thin film is introduced. This dispersion law is used to predict group velocities of the spin waves, their lifetime, and resulting propagation length in various materials.

The following chapter summarizes the theory of light scattering. The chapter starts with the classical treatment of Rayleigh and Mie scattering. Then, the inelastic scattering is explained by the Doppler shift of the light on a moving periodic change of the index of refraction. Later in this chapter, a quantum mechanical treatment is used to find

formulas for cross-sections of the quasi-elastic, Raman, and Brillouin scattering. The last section is devoted to reviewing the current state of the art in the Brillouin light scattering applications, mainly in the spin-wave research.

The third chapter shows the design and characterization of the Brillouin light scattering setup. The schematic of the whole setup is presented. Then we describe the individual parts and the performance of the setup. At the end of the chapter, we verify the setup with full phase reconstruction on the well-known system of permalloy thin film.

In the last chapter, we present recently published results [17], where we investigate the propagation of spin waves through a domain wall. We perform static characterization employing micromagnetic simulations, magnetic force microscopy, and thermal Brillouin light scattering experiments. We reveal that the type of the domain wall is Néel wall with topologically enforced circular Bloch line. We measure the propagation of spin waves through the wall with intensity and phase-resolved Brillouin light scattering. We further explain and confirm the obtained results with micromagnetic simulations. At the end of the chapter, we propose the possibility to displace the circular Bloch line towards the edges of the waveguide to manipulate spin-wave propagation.

# 1. Basics of micromagnetic theory and spin waves

This chapter briefly introduces the basics of energies in micromagnetic theory and the concept of the effective field. Then the general law of dipole-exchange dispersion of spin waves will be used to explore dependencies of propagation lengths on thin film properties. In the last section the properties of chosen materials used in spin wave research will be shown.

## 1.1. Energies in magnetism

The four main sources of energies can be recognized in magnetic systems: exchange energy, Zeeman energy, dipolar energy and anisotropy energy. In specific systems other energy terms such as magnetoelastic energy can be added.

### 1.1.1. Exchange energy

The exchange energy ( $E_{\text{ex}}$ ) originates from quantum-mechanical interactions. The energy contribution can be written as

$$E_{\text{ex}} = A_{\text{ex}} \iiint_V \left( \nabla \cdot \frac{\vec{M}}{M_s} \right)^2 dV, \quad (1.1)$$

where  $A_{\text{ex}}$  is the exchange constant and  $V$  is the volume of magnetic material. In ferromagnetic materials the exchange constant is positive and yields parallel spin configuration which is illustrated in Figure 1.1 (a). On the contrary, in antiferromagnetic systems the exchange constant is negative and the spins are aligned antiparallel.

### 1.1.2. Zeeman energy

The energy between the magnetization and the external field is called the Zeeman energy. The contribution of this energy is

$$E_Z = -\mu_0 \iiint_V \vec{M} \cdot \vec{H}_{\text{ext}} dV, \quad (1.2)$$

where  $\vec{H}_{\text{ext}}$  is the external field. This energy is minimized, when the external field and the magnetization are parallel.

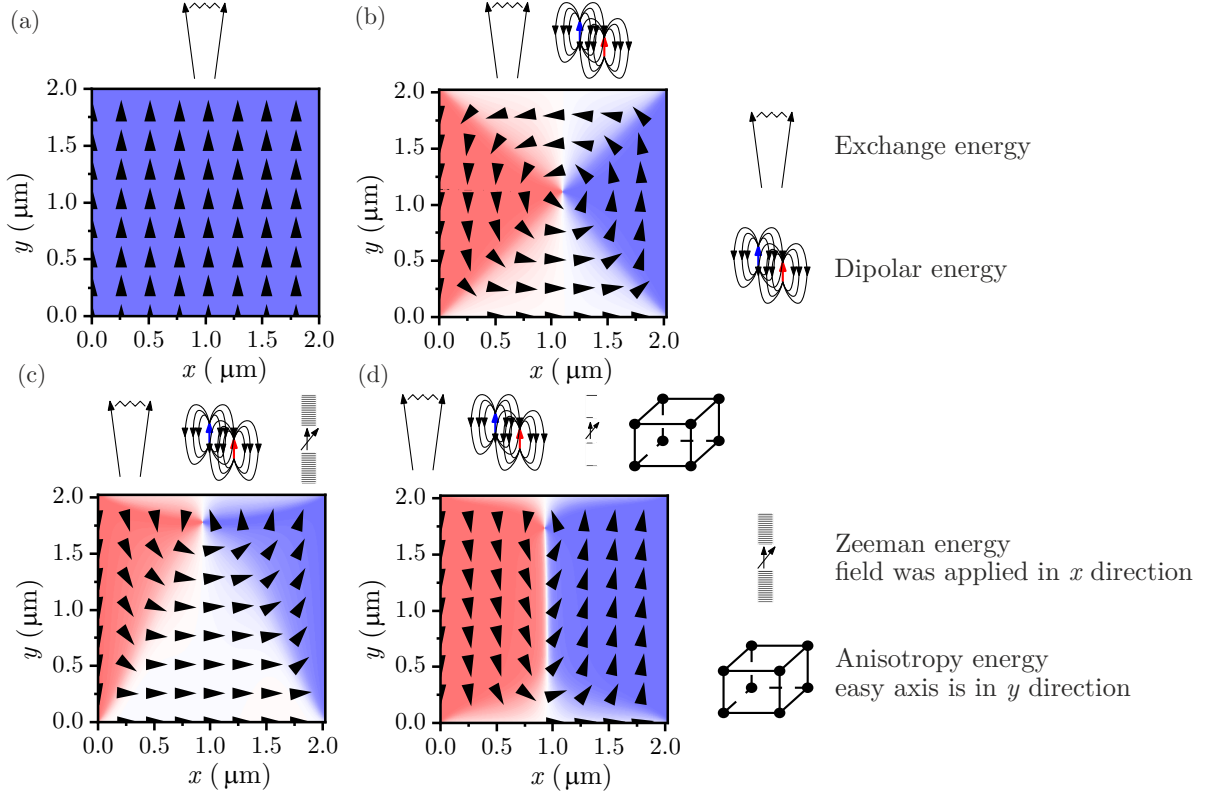


**Figure 1.1:** Micromagnetic simulations, where the energies are gradually taken into account. (a) exchange energy. (b) exchange + dipolar energy. (c) exchange + dipolar + Zeeman energy. (d) exchange + dipolar + Zeeman + anisotropy energy. The spatial distribution was obtained using MuMax3, with cell size  $4^3 \text{ nm}^3$ , total area  $2^2 \mu\text{m}^2$  and material parameters for permalloy (see the Table 1.1).

### 1.1.3. Dipolar energy

The dipolar energy is in principle the same as the Zeeman energy, but instead of an external field, the field created by the magnetization is assumed

$$E_d = -\frac{1}{2}\mu_0 \iiint_V \vec{M} \cdot \vec{H}_d dV, \quad (1.3)$$

where prefactor  $\frac{1}{2}$  is present to avoid counting one interaction twice. The  $\vec{H}_d$  is demagnetizing field and is given by

$$\nabla \cdot \vec{H}_d + \nabla \cdot \vec{H}_{\text{ext}} = -\nabla \cdot \vec{M}. \quad (1.4)$$

From equations 1.3 and 1.4 we can conclude that this energy will be minimized when so called magnetic charges ( $\nabla \cdot \vec{M}$ ) are avoided. The resulting reduction of these charges can be seen in Figure 1.1 (b). Figure 1.1 (c) shows the magnetic ordering when also the Zeeman energy is considered<sup>1</sup>.

### 1.1.4. Anisotropy energy

Due to the crystallographic structure of the material, an additional energy term can arise. This term is called the anisotropy energy ( $E_{\text{anis}}$ ). The form of this term can vary, but

<sup>1</sup>In the simulation an external magnetic field of 2 mT was applied.

in the simplest case it can be described as an uniaxial anisotropy ( $E_{\text{u-anis}}$ ), with one preferable direction (easy axis)

$$E_{\text{u-anis}} = \iiint K_{\text{u}} \sin^2 \vartheta dV, \quad (1.5)$$

where  $K_{\text{u}}$  is uniaxial anisotropy constant and  $\vartheta$  is the angle between the magnetization and the easy axis. The corresponding anisotropy field can be expressed as

$$H_{\text{u-anis}} = \frac{2K_{\text{u}}}{\mu_0 M_{\text{s}}}. \quad (1.6)$$

The contribution of this energy to the magnetic state is depicted in Figure 1.1 (d).

## 1.2. Effective field

These overall contributions can be expressed as an effective field  $\vec{H}_{\text{eff}}$ , which accounts for all energy contributions. This field describes how all energy terms influence the magnetization. The global energy minimum is reached when the magnetization is pointing in the direction of this field. First, we have to get the total energy ( $E_{\text{tot}}$ ) of the system

$$E_{\text{tot}} = E_{\text{ex}} + E_{\text{Z}} + E_{\text{d}} + E_{\text{anis}}. \quad (1.7)$$

The effective field is then obtained as

$$\vec{H}_{\text{eff}} = -\frac{1}{\mu_0} \frac{\partial E_{\text{tot}}}{\partial \vec{M}}, \quad (1.8)$$

where  $\frac{\partial E_{\text{tot}}}{\partial \vec{M}}$  is a directional derivation and can be computed as

$$\frac{\partial E_{\text{tot}}}{\partial \vec{M}} = \frac{1}{M_{\text{s}}^2} (\nabla E_{\text{tot}}) \cdot \vec{M}. \quad (1.9)$$

The torque ( $T$ ) which will act on magnetization can be expressed as follows

$$T = \vec{M} \times \vec{H}_{\text{eff}}. \quad (1.10)$$

From this equation it is apparent, that the equilibrium is reached when the magnetization and the effective field are parallel.

## 1.3. Magnetization dynamics

Energy minimization techniques can describe only static configurations of magnetization while an equation of motion is needed in order to tackle the magnetization dynamics. The equation of motion can be derived from the quantum mechanics [18, 19].

The form of this equation is similar to the momentum equation, and can be written in the following form

$$\frac{d\vec{M}}{dt} = -\gamma \mu_0 \vec{M} \times \vec{H}_{\text{eff}}, \quad (1.11)$$

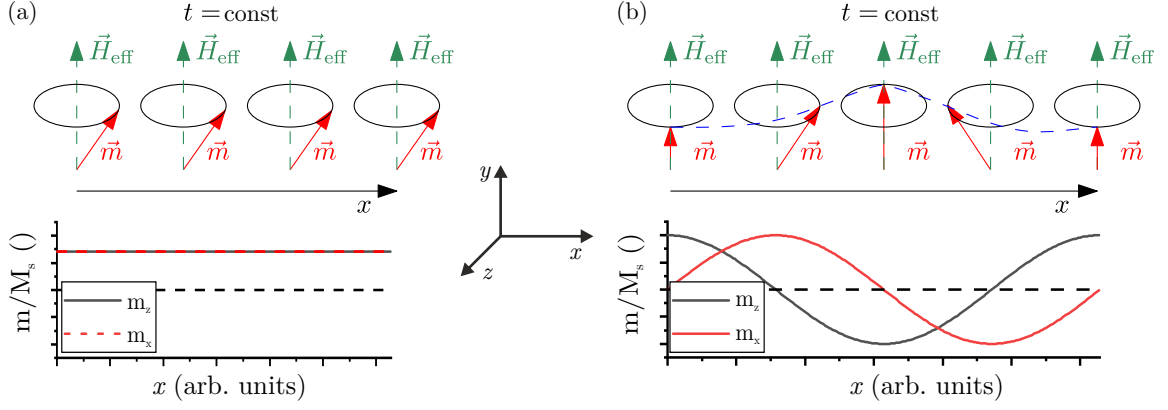


**Figure 1.2:** (a) The schematic of ferromagnetic resonance. The upper panel shows the oscillation of the magnetic moments of the ferromagnetic mode ( $k = 0$ ). The lower panel shows a spatial evolution of the dynamic components of the magnetization. (b) Schematic of a spin waves. The upper panel shows oscillations of the magnetization with  $k \neq 0$ . The lower panel shows the spatial evolution of dynamic components.

where  $\gamma$  is the gyromagnetic ratio. This equation is called Landau-Lifschitz equation. The form including energy dissipation can be derived from the first principles and spin-orbit coupling [20]

$$\frac{d\vec{M}}{dt} = -\gamma\mu_0\vec{M} \times \vec{H}_{\text{eff}} + \frac{\alpha}{M_s}\vec{M} \times \frac{d\vec{M}}{dt}, \quad (1.12)$$

where  $\alpha$  is Gilbert damping. This form of the damping term was first phenomenologically added by Gilbert, thus it is called Landau-Lifschitz-Gilbert equation.

## 1.4. Ferromagnetic resonance

The solutions of (1.11) in a form of coherent oscillation is called ferromagnetic resonance (FMR). In this case wavenumber is assumed as  $k = 0$ , the whole magnetization oscillates in phase. The frequency of FMR ( $\omega_{\text{FMR}}$ ) is given by [21, 22]

$$\omega_{\text{FMR}}^2 = \omega_{\text{H}}(\omega_{\text{M}} + \omega_{\text{H}}), \quad (1.13)$$

where  $\omega_{\text{H}} = \mu_0\gamma H_{\text{eff}}$  and  $\omega_{\text{M}} = \mu_0\gamma M_s$ .  $\omega_{\text{H}}$  accounts only for the contribution of the effective field, while  $\omega_{\text{M}}$  is dependent only on material parameters. The FMR mode is illustrated in Figure 1.2 (a).

## 1.5. Spin waves

The oscillation with  $k \neq 0$  [which is shown in Figure 1.2 (b)] are called spin waves. The modes of the fully saturated homogeneous media was derived by Walker

$$(1 + \xi) \left[ \frac{\partial^2 \psi}{\partial x^2} \frac{\partial^2 \psi}{\partial y^2} \right] + \frac{\partial^2 \psi}{\partial z^2} = 0, \quad (1.14)$$

where  $\psi$  is susceptibility tensor and  $\psi$  is magnetostatic potential. We can recognize two major geometries for in-plane magnetization. The so-called Damon-Eshbach geometry,

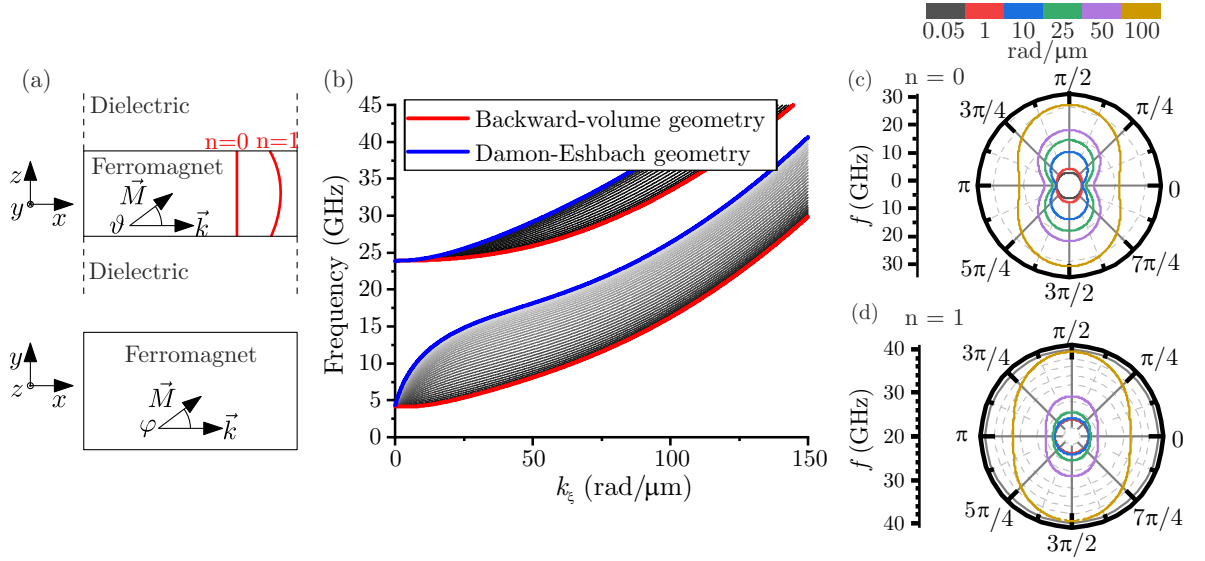


**Figure 1.3:** (a) Schematics of geometry used in 1.17. The upper panel shows the view from the side (thin film cross-section). The bottom panel shows a top view of a thin film. (b) Computed dispersion relation for thin permalloy film ( $t = 30$  nm). The spin waves with  $k$  perpendicular (parallel) to the static magnetization  $\vec{M}$  are depicted in blue (red) color. The lines in gray shades show angles in between these two geometries. The first two thickness modes are shown. (c) (d) Polar plots of frequency depending on the direction of propagation. The zero-order thickness mode  $n = 0$  (c) and first thickness mode  $n = 1$  (d) are shown.

where the magnetization is perpendicular to the direction of the spin wave propagation and Backward-volume geometry, where the magnetization and direction of the spin waves are co-linear. The derivation of dispersion of both of these geometries can be found in [13, 23].

The dispersion of the Damon-Eshbach mode is [23–25]

$$\omega_{\text{DE}}^2 = \omega_{\text{H}} (\omega_{\text{M}} + \omega_{\text{H}}) + \frac{\omega_{\text{M}}^2}{4} [1 - \exp(-2kt)], \quad (1.15)$$

where  $t$  is the film thickness.

The dispersion relation for the case of Backward-volume geometry is [13]

$$\omega_{\text{BV}}^2 = \omega_{\text{H}} \left[ \omega_{\text{M}} \left( \frac{1 - \exp(-kt)}{kt} \right) + \omega_{\text{H}} \right]. \quad (1.16)$$

These two equations take only dipolar interaction into account. More general law describing the dispersion relation of spin waves can be obtained if also the exchange interaction is considered. The complete dipole-exchange spectrum was derived by Kalinikos and Slavin [26]

$$\omega^2 = (\omega_{\text{H}} + A\omega_{\text{M}}k^2) (\omega_{\text{H}} + A\omega_{\text{M}}k^2 + \omega_{\text{M}}F_n), \quad (1.17)$$

where

$$F_n = P_n + \sin(\vartheta)^2 \left( 1 - P_n (1 + \cos(\varphi)^2) \right) + \frac{\omega_{\text{M}}P_n(1 - P_n) \sin(\varphi)^2}{\omega_{\text{H}} + A\omega_{\text{M}}k^2}, \quad (1.18)$$

with

$$P_n = \begin{cases} \frac{k_\xi^2}{k^2} - \frac{k_\xi^4}{k^4} \frac{1}{2} \left[ \frac{2}{k_\xi t} (1 - \exp(-k_\xi t)) \right] & n = 0 \\ \frac{k_\xi^2}{k^2} - \frac{k_\xi^4}{k^4} \left[ \frac{2}{k_\xi t} (1 - \exp(-k_\xi t)) \right] & n \neq 0 \end{cases} \quad (1.19)$$

for the case of totally unpinned surface spins, or

$$P_n = \frac{k_\xi^2}{k^2} - \frac{k_\xi^2}{k^2} (1 - \exp(-k_\xi t)), \quad (1.20)$$

for the totally pinned surface spins. The  $k_\xi$  stands for the magnitude of the wavevector in the in-plane direction of propagation of spin waves, while the  $k$  is overall magnitude of wavevector as can be seen in the upper panel in Figure 1.3 (a). The magnitude of the  $k$  can be calculated from

$$k = \sqrt{k_\xi^2 + \left(\frac{n\pi}{t}\right)^2 + \left(\frac{n_w\pi}{w_{\text{eff}}}\right)^2}, \quad (1.21)$$

where  $n = 0, 1, 2, \dots$  and stands for the number of the thickness mode and  $n_w = 0, 1, 2, \dots$  is quantization number in the transversal direction in the case of the magnetic waveguide. The  $t$  is the film thickness and the  $w_{\text{eff}}$  is the effective width and will be discussed later. The  $\vartheta$  is out-of-plane angle of magnetization and  $\varphi$  is an in-plane angle between the magnetization and the direction of propagation of the spin wave. Both are depicted in Figure 1.3 (a). The parameter  $A$  is equal to

$$A = \frac{A_{\text{ex}}^2}{\mu_0 M_s^2}. \quad (1.22)$$

The difference between the two aforementioned boundary conditions (totally pinned and totally unpinned surface spins) is, in most cases, negligible. The discrepancy arises only where some confinement is present ( $n \neq 0$ ,  $n_T \neq 0$ ). Usually, the totally pinned boundary condition is closer to reality, and a slight deviation from this case can be compensated by choosing a slightly bigger effective width ( $w_{\text{eff}}$ ) or thickness ( $t$ ) than the nominal width or thickness.

Dispersions of the 30 nm thick permalloy layer for the first two thickness modes are shown in Figure 1.3 (b). The Damon-Eshbach geometry and Backward-volume geometry are shown in blue or red, respectively. The iso- $k$  polar graphs are shown for zero-order thickness mode in Figure 1.3 (c) and for the first-order thickness mode in Figure 1.3 (d). The anisotropic behavior of the spin waves in an in-plane magnetized thin film for zero-order thickness mode is visible. When the magnitude of  $\vec{k}$  increases, this anisotropic behavior becomes less pronounced. The first-order thickness mode is isotropic for experimentally accessible magnitudes of wavevectors ( $k < 50 \text{ rad}/\mu\text{m}$ ). The used Matlab function is presented in appendix A.

### 1.5.1. Group velocity and propagation length of spin waves

The group velocity ( $v_g$ ) can be calculated from the dispersion relation as

$$v_g = \frac{\partial \omega}{\partial k}. \quad (1.23)$$

The calculated group velocities of spin waves in a thin permalloy film are shown in Figure 1.4 (a). For higher  $k$  values, where exchange interaction dominates, both modes have

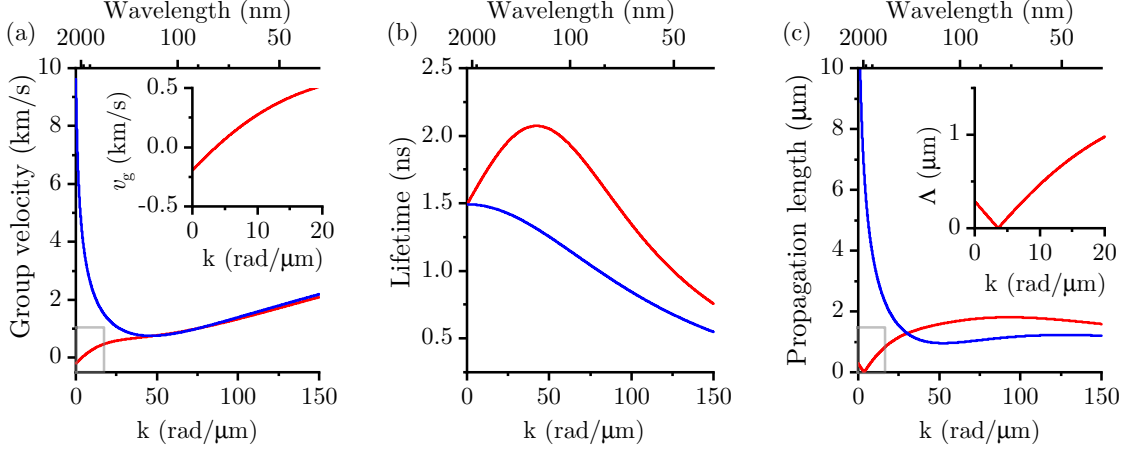


**Figure 1.4:** Blue (red) curves show characteristics for spin waves with  $\vec{k}$  perpendicular (parallel) to the equilibrium direction of the magnetization. (a) The group velocity of spin waves. Inset shows detail of negative group velocity in Backward-volume geometry. (b) The lifetime of spin waves. (c) Propagation length of spin waves. The inset shows detail of the zero propagation length in Backward-volume geometry. All calculations are done for thin permalloy ( $t = 30$  nm) layer in external field of 20 mT.

similar group velocity. The Damon-Eshbach mode exhibits a minimum in the dipole-exchange part of the spectrum. As can be seen in the inset, the Backward-volume mode's group velocity is negative for the dipole part (low  $k$  values) of the spectrum. The derived analytic formulas for group velocities in Damon-Eshbach and Backward-volume geometry are given in appendix B.

The spin-wave lifetime is given by [10, 13]

$$\tau = \alpha\omega \frac{\partial\omega}{\partial\omega_H}. \quad (1.24)$$

The derived formulas for a lifetime in Damon-Eshbach and Backward-volume geometries are shown in appendix B. An interesting fact is that the lifetime of the Damon-Eshbach mode is not dependent on the thickness of the film. On the other hand, there is a dependence for Backward-volume waves. In the exchange dominated part of the spectrum, the lifetimes of both modes are again similar, as can be seen in Figure 1.4 (b). The dependencies of both, the group velocity and the lifetime of spin waves on the thickness and the external field are shown in appendix C.

Now the propagation length  $\Lambda$ , which is the distance where the signal drops to  $\frac{1}{e}$  of its maximal value, can be obtained as a product of the spin-wave lifetime and the group velocity

$$\Lambda = \tau v_g. \quad (1.25)$$

The propagation lengths for both modes are shown in Figure 1.4 (c). The Backward-volume mode exhibits zero propagation length in the position of global frequency minimum<sup>2</sup>. The longest propagation length is reached for the  $k \rightarrow 0$  in Damon-Eshbach geometry.

The dependence of the propagation length on the external field is shown in Figure 1.5 (a). The propagation length for Damon-Eshbach mode decreases with a higher

<sup>2</sup>Where the group velocity is equal to zero

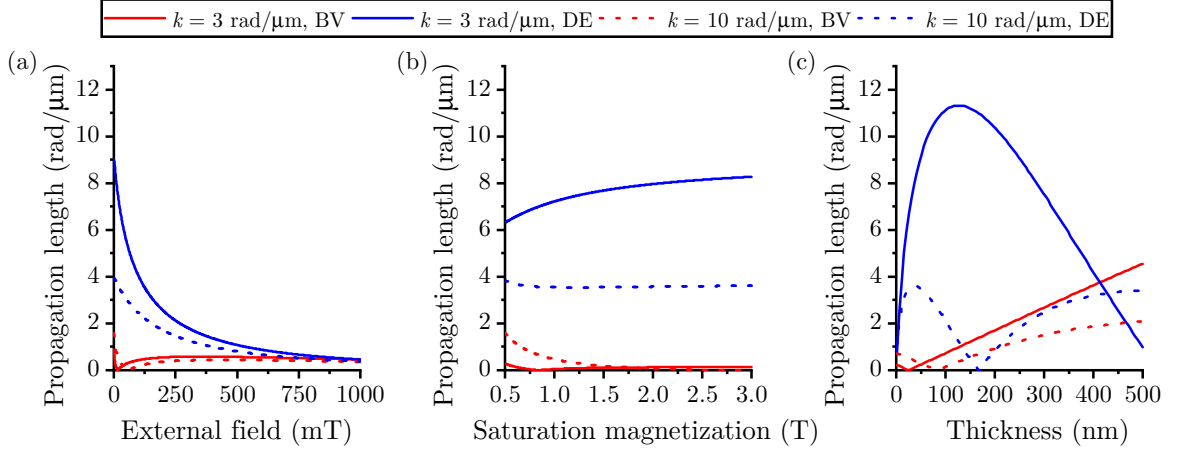


**Figure 1.5:** Blue (red) curves show characteristics for spin waves with  $\vec{k}$  perpendicular (parallel) to the static magnetization. Solid (dashed) line shows  $k = 3 \frac{\text{rad}}{\mu\text{m}}$  ( $k = 10 \frac{\text{rad}}{\mu\text{m}}$ ). (a), (b), (c) The dependence of the propagation length on external field, saturation magnetization and thickness of the layer. Fixed parameters are same as in Figure 1.4.

external field, while the Backward-volume mode has zero propagation length in the position of the global frequency minimum.

The Figure 1.5 (b) shows the dependence of the propagation length on the saturation magnetization. For Damon-Eshbach mode, the dependence is rather weak. For low  $k$  vectors, the propagation length is increasing, but on the other hand, for the high  $k$  vectors, the propagation length decreases with the saturation magnetization. Again, the propagation length in Backward-volume is affected by the existence of the global frequency minimum. Before reaching the aforementioned minimum, the propagation length is decreasing, while after this minimum, it is increasing. One can see that this point is moved further for higher  $k$  vectors. In other words, the higher saturation magnetization moves this minimum towards a higher  $k$ .

The dependence of propagation length on the thickness of the film is shown in Figure 1.5 (c). For Damon-Eshbach mode, a clear maximum is visible. This maximum is moved towards low thicknesses for higher  $k$  values. For films with high thicknesses, the propagation length exhibits for certain  $k$ -vectors values zero propagation length caused by a change in group velocity towards negative values. In the Backward-volume geometry in the dipole part of the spectrum, lower thicknesses will result in longer propagation lengths. In contrary the exchange dominated part of the spectrum will provide longer propagation lengths for the higher thicknesses.

## 1.6. Materials used in spin-wave research

The spin waves are usually studied in thin magnetic films. As was discussed in the previous section, to assure high propagation length, low Gilbert damping is necessary. Also to have a sufficient signal either in magneto-optical or in electrical experiments a high saturation magnetization is favorable. Several materials fulfill these demands. The most commonly used materials in spin wave research are shown in Table 1.1.

The first material shown is nm-thick Yttrium Iron Garnet. It is a magnetic insulator and single-crystal. It is widely used in research, mainly because of low Gilbert damping

## 1.6. MATERIALS USED IN SPIN-WAVE RESEARCH

**Table 1.1:** A selection of materials which are used in spin-wave research. The material parameters and spin wave characteristic for  $k = 3 \text{ rad}/\mu\text{m}$  ( $\lambda \approx 2 \mu\text{m}$ ), external field of  $B_{\text{ext}} = 20 \text{ mT}$  and film thickness of  $t = 15 \text{ nm}$  are given for each material. The external field was applied in easy-axis direction for metastable iron. Inspired by [10, 11].

	nm-thick Yttrium Iron Garnet (YIG)	Permalloy (Py, NiFe)	CoFeB	Metastable iron (FeNi)
<b>Chemical composition</b>	$\text{Y}_3\text{Fe}_5\text{O}_{12}$	$\text{Ni}_{81}\text{Fe}_{19}$	$\text{Co}_{40}\text{Fe}_{40}\text{B}_{20}$	$\text{Fe}_{78}\text{Ni}_{22}$
<b>Gilbert damping</b> $\alpha$ ( $\cdot 10^{-4}$ )	2	70	40	80
<b>Sat. magnetization</b> $M_s$ , (kA/m)	140	800	1250	1410
<b>Exchange constant</b> $A_{\text{ex}}$ , (pJ/m)	3.6	16	15	11
<b>Typical film thickness</b> $t$ (nm)	5-100	5-100	5-100	5-20
<b>Anisotropy field</b> (mT)	$\approx 0$	$\approx 0$	$\approx 0$	$\approx 25$
<b>Frequency</b>	2.0	6.0	8.5	11.3
<b>DE/BV</b> (GHz)	1.8	4.2	5.2	8.3
<b>Group velocity</b>	0.37	3.2	5.44	5.2
<b>DE/BV</b> (km/s)	0.06	0.06	-0.002	-0.13
<b>Lifetime DE/BV</b>	251	1.49	1.69	0.73
(ns)	256	1.52	1.73	0.75
<b>Propagation</b>	95.0	4.8	9.2	3.8
<b>length DE/BV</b>	14.8	0.09	0.003	0.1
( $\mu\text{m}$ )				
<b>References</b>	[27–33]	[34–37]	[38–40]	[37, 41]

constant and thus long lifetime and propagation length of spin waves. On the other hand, low saturation magnetization and the fact that it is transparent for visible light makes the application of this material cumbersome, especially for Brillouin light scattering (BLS) experiments.

Permalloy is a polycrystalline material. It has typically very low anisotropy field  $\approx 0 \text{ mT}$ . The Gilbert damping is approximately one order of magnitude higher than in the case of YIG, which results in a shorter spin-wave lifetime. However, the shorter lifetime is partially compensated by higher group velocities. Also, the higher saturation magnetization and easiness of fabrication of micro/nano-structures make this material a good candidate for future magnonic applications.

The CoFeB is new promising material. It is an amorphous material; thus, the anisotropy field is usually below  $2 \text{ mT}$ . It has higher saturation magnetization and lower damping than permalloy, which results in relatively long propagation distances.

The last material discussed in this thesis is metastable iron [37, 42–45]. It is a crystalline material that is epitaxially grown on a copper single crystal. After the growth of the layer, it is in a metastable paramagnetic fcc state. If momentum is provided to the lat-

## 1.6. MATERIALS USED IN SPIN-WAVE RESEARCH

tice, e.g., by hitting by heavy ions, it can recrystallize to the ferromagnetic bcc phase. It is possible to imprint uniaxial anisotropy in different orientations by choosing specific ways of irradiating the sample. This can be used to produce magnonic waveguides that allow propagation in Damon-Eshbach mode in zero-magnetic-field, where longer propagation length is reached [41].

## 2. Theory of light scattering

Since the times of ancient Greek, people were fascinated by the blueness of the sky [46]. They believed that the blue shade of the sky could protect them from evil. Nevertheless, one of the first explanations came from Leonardo da Vinci, who observed that the sky's brightness is decreasing with higher altitude. From this, he deduced that the heated moisture in the air seems luminous against the above darkness.

In this chapter, we will examine the light scattering from the point of view of both, classical and quantum mechanical approaches. In the classical approach, the Rayleigh and the Mie scattering will be discussed. The inelastic scattering will be described as a Doppler shift of incident light on the propagating wave in the material. The cross-sections of quasi-elastic, Brillouin, and Raman scattering will be depicted in the section dedicated to quantum treatment. Later in the chapter, the experimental setups and applications of Brillouin light scattering will be described.

### 2.1. Classical treatment

We will start the treatment of scattering with a classical approach. This approach considers light as an electromagnetic wave, and quasi-particles are treated as a wave of an index of refraction.

#### 2.1.1. Rayleigh scattering

Explanation of the blueness of the sky based on classical theory was provided by J.W. Strutt commonly known as Lord Rayleigh. He assumed spherical particles with a diameter much smaller than the wavelength of the incident light [47]. With these assumptions, he found that the scattered light intensity has to be proportional to  $\lambda^{-4}$ . The full formula for scattered intensity could be found e.g., in [48]

$$I_{\text{RS}} = I_0 \left( \frac{2\pi n_0}{\lambda} \right)^4 \frac{r^6}{2D^2} \left( \frac{\varepsilon - \varepsilon_0}{\varepsilon + 2\varepsilon_0} \right)^2 (1 + \cos^2 \Theta), \quad (2.1)$$

where  $I_{\text{RS}}$  is the Rayleigh scattered intensity,  $I_0$  is the incidence intensity,  $D$  is the distance between the observer and the particle,  $r$  is the diameter of particle,  $\varepsilon$  is the dielectric constant,  $\varepsilon_0$  is the vacuum permittivity,  $\Theta$  is the scattering angle and  $\lambda$  is the wavelength of incidence light. The geometry is depicted in Figure 2.1 (c). From this equation, one could see that there is also dependency on the scattering angle. The forward and backward scattered light has two times higher intensity than the light scattered to perpendicular direction.

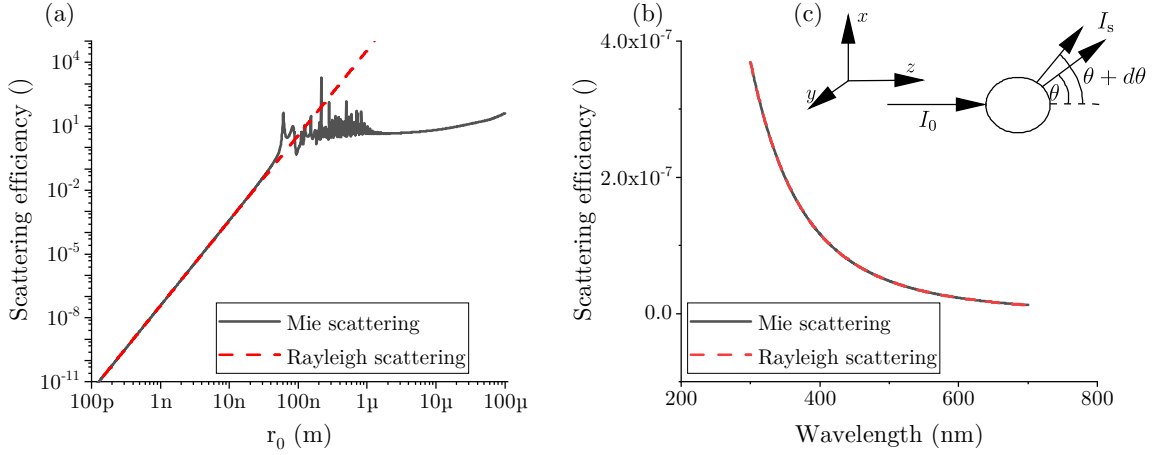


**Figure 2.1:** (a) The dependency of scattering efficiency on the radius of the particle on which light is scattered. Both axes are in logarithmic scale. The black solid line shows the Mie model, and the dashed red line shows the Rayleigh model. (b) The dependency of scattering efficiency on the wavelength of the incident light. (c) The schematic of scattering geometry.

The differential cross section expresses the probability of scattering to infinitesimally small angle. The integration over all angles is called total cross-section ( $\sigma$ ). For Rayleigh scattering we obtain [49]

$$\sigma_{\text{RS}} = \frac{8\pi}{3} \left( \frac{2\pi n_0}{\lambda} \right)^4 r^6 \left( \frac{\varepsilon - \varepsilon_0}{\varepsilon + 2\varepsilon_0} \right)^2. \quad (2.2)$$

If we consider visible light, we would find that the scattering efficiency, which is the ratio of the scattering cross-section to the geometric cross-section; for the blue light it is approximately ten times higher than for the red light, as can be seen in Figure 2.1 (b). This is the reason why the sky seems blue during the day. Contrary to that, during the sunset, more blue light is scattered out of the beam path, and the sky has a red color.

### 2.1.2. Mie scattering

Mie considered a more complex case, when the size of the particle can be arbitrary. For the limiting case when  $r \ll \lambda$  both theories are in a good agreement as can be seen from Figure 2.1 (a). This calculation assumes, that the incident wave is spherical as well as the scattered one. The resulting total cross section ( $\sigma_{\text{MS}}$ ) is expressed in the form of infinite series [49]

$$\sigma_{\text{MS}} = \frac{\lambda}{2\pi n_0^2} \sum_i^{\infty} \left[ \left( 2 \frac{n}{n_0} + 1 \right) \left( |a_i(2\pi n_0 r / \lambda)|^2 + |b_i(2\pi n_0 r / \lambda)|^2 \right) \right], \quad (2.3)$$

where  $a_i$  and  $b_i$  are spherical Hankel functions and spherical Bessel functions, respectively.

### 2.1.3. Doppler shift of the scattered light

If the particle on which the light is scattered is in motion, then one can observe a change in the frequency of the scattered light. This change in frequency can be expressed as

$$\Delta f = \pm 2\lambda v, \quad (2.4)$$

where  $\Delta f$  is a change in the frequency of the scattered light,  $v$  is the projection of the velocity of the particle to the direction of the incident light. The plus and minus sign is for the case when the particle is moving towards and from the light source, respectively. So if we take this effect into account, and consider that the particle velocities have a random direction, we will obtain a frequency broadening of the scattered light [50].

In some situations, the particle motion is not completely random. In this case, we can think of the movement of particles as an acoustic wave. Such an acoustic wave would result in a periodic change of index of refraction of the medium. This periodic modulation would behave like Bragg crystal, thus it will reflect light when the projection of the incident  $k$ -vector of light and  $k$ -vector of the acoustic wave will match. In this case we can substitute the velocities in the equation (2.4)  $v = \frac{f_p}{k_p}$ . With this substitution, we get that the frequency shift is exactly equal to the acoustic wave frequency when Bragg's condition is fulfilled.

## 2.2. Quantum treatment

To get a better insight, we can also treat scattering from the quantum point of view. In this case, we will consider light as a particle with the momentum and energy. This allows us to find the value of frequency shift only based on the laws of conservation of momentum and energy in the system of interacting particles and quasi-particles.

### 2.2.1. Quasi-elastic scattering

We will write down equations for conservation of momentum and for conservation of energy. We will consider the energy of incident photon and the kinetic energy of the particle on which the photon is scattered

$$hf_1 + \frac{1}{2}mv_p^2 = hf_1' + \frac{1}{2}mv_p'^2, \quad (2.5a)$$

$$h\vec{k}_1 + m\vec{k}_p = h\vec{k}_1' + m\vec{k}_p', \quad (2.5b)$$

where  $h$  is the Planck constant,  $f_l$  is the frequency of light,  $m$  is the mass of the particle on which the light is scattered. Usually, the kinetic energy of particles is much lower than that of the incident light, so this will result in small broadening of the frequency of the scattered light. This process is called quasi-elastic scattering. The total cross-section is proportional to [51][45]

$$\sigma_{\text{QES}} \sim \frac{\gamma}{(\omega_i - \omega_s)^2 + \gamma^2}, \quad (2.6)$$

where  $\omega_i$  is incident frequency of light,  $\omega_s$  is scattered frequency of light and  $\gamma$  is a broadening parameter which is dependent on thermal energy, entropy, heat capacity, etc. One can see, that the highest scattering efficiency is reached when the scattered light has the same frequency as the incident light.

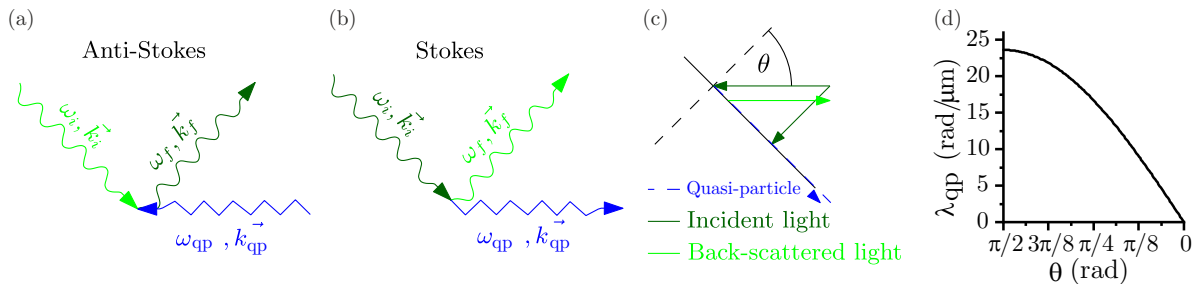


**Figure 2.2:** The Stokes (a) and anti-Stokes (b) processes are schematically shown. (c) The schematic of back-scattering geometry. (d) Detectable spin-wave wavenumber depending on the angle of incidence of light with a wavelength of 532 nm.

### 2.2.2. Raman scattering

The light can also be scattered on intrinsic vibrational, rotational or higher excited states of particles. This scattering will also be ruled by the equations of conservation of energy and momentum. The cross section is given by [52, p. 379],

$$\sigma_{R-aS} \sim \sum_{\omega_t} \frac{\omega_l(\omega_l + \omega_t)^3}{(\omega_l - \omega)^2 + \gamma_R^2}, \quad (2.7a)$$

$$\sigma_{R-S} \sim \sum_{\omega_t} \frac{\omega_l(\omega_l - \omega_t)^3}{(\omega_l - \omega)^2 + \gamma_R^2}, \quad (2.7b)$$

where  $\omega_t$  is frequency of transition and  $\gamma_R^2$  is damping parameter. We can see, that Raman resonances can occur for several frequencies, depending on the number of allowed transitions. Typically, the frequencies of these transitions are in the terahertz range, as can be seen in Figure 2.3 (c).

In the experiment, the light is angularly divided by the dispersive grating, and then the intensity distribution is measured in a charge-coupled device (CCD) camera. One of the camera dimensions will be then proportional to the frequency shift.

Raman scattering can be used for analysis of substances because transition frequencies are intrinsic properties of molecules. Also, a number of layers in graphene or binding parameters between layers could be determined [53]. The Raman scattering is also widely used in biology and pharmaceutical research [54, 55].

### 2.2.3. Brillouin light scattering

Now we will consider the case where the photon is scattered on a quasi-particle, e.g., a phonon or a magnon. This scattering happens in a frequency range between hundreds of megahertz to hundreds of gigahertz. Schematic of a typical Brillouin light spectrum is shown in Figure 2.3 (c). In this case, we get this set of energy and momentum conservation equations

$$hf_1 + hf_{qp} = hf'_1 + hf'_{qp}, \quad (2.8a)$$

$$h\vec{k}_1 + h\vec{k}_{qp} = h\vec{k}'_1 + h\vec{k}'_{qp}, \quad (2.8b)$$

where  $h$  is the Planck constant,  $f_1$  is the frequency of light and  $f_{qp}$  is the frequency of quasi-particle. To conserve both the energy and the momentum, only two cases are

allowed. In the first one, the quasi-particle's final energy is zero, the quasi-particle is annihilated, and the energy of the scattered light is increased, which results in a shift towards higher frequency. This is called the Anti-Stokes process, and it is schematically shown in Figure 2.2 (a). In the second case, if the initial energy and momentum of the quasi-particle are equal to zero, then the energy and momentum of the incident light are used for the creation of a quasi-particle, thus the frequency of the scattered light is lower. This is called the Stokes process, and it is shown in Figure 2.2 (b).

Typically, the back-scattering geometry is used in experiments, as shown in Figure 2.2 (c). In the thin film, the probed quasi-particle wavenumber is then equal to twice the in-plane component of the wavenumber of the light. The limit of maximal probed  $k$ -vector versus angle of incidence using 532 nm laser is shown in Figure 2.2 (d). The maximal value of wavenumber is reached in the case where the laser beam is parallel with the surface of the sample. Again, in the case of the green light (532 nm), the maximal value of probed wavenumber is  $23.6 \text{ rad} \cdot \mu\text{m}^{-1}$ , which is equal to the wavelength of 266 nm.

### Scattering on magnons

To obtain the cross section, we will restrict only to the scattering of the light on magnons. It was shown by Cottam [56] that scattering cross section is proportional to the population of magnons, which is determined by Bose-Einstein distribution and by the imaginary part of the Green function of the spin wave response

$$\sigma_{\text{B-aS}} \sim \frac{P_i \omega_l (\omega_l + \omega_{\text{qp}})^3}{\exp(\frac{\hbar \omega_{\text{qp}}}{k_b T}) - 1} \text{Im} \{G\}, \quad (2.9)$$

for the anti-Stokes and

$$\sigma_{\text{B-S}} \sim \frac{P_i \omega_l (\omega_l - \omega_{\text{qp}})^3}{\exp(\frac{\hbar \omega_{\text{qp}}}{k_b T})} \text{Im} \{G\}, \quad (2.10)$$

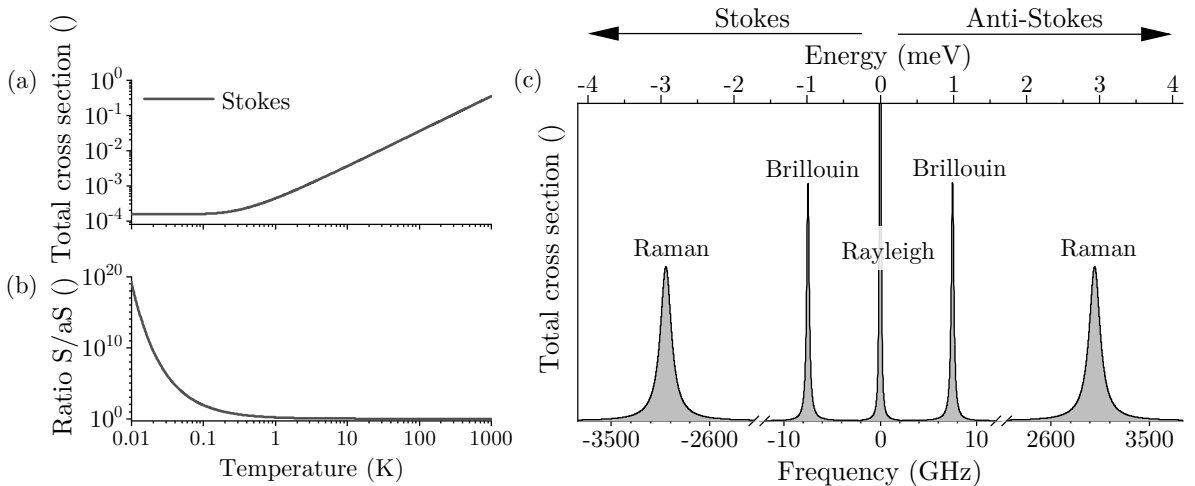


**Figure 2.3:** The calculated total cross-section of the Stokes magnon-photon process is shown in (a) in dependence on temperature for the NiFe layer. The material parameters can be found in Table 1.1. The thickness is 40 nm, and spin waves are propagated in Damon-Eshbach geometry. (b) The ratio of the cross-section of Stokes and anti-Stokes processes. The calculation parameters were the same as for (a). (c) The schematic of the light scattering processes.

for the Stokes process, where  $k_b$  is the Boltzmann constant,  $P_i$  is incident power and  $\text{Im}\{G\}$  is the imaginary part of Green function of the spin wave response. We modeled the total cross section of Brillouin processes for different temperatures. In Figure 2.3 (a), dependency of the Stokes signal on the temperature is shown. With decreasing the temperature of the sample under investigation, the signal strength could be decreased by three orders of magnitude.

The ratio between Stokes and anti-Stokes signal strength is shown in Figure 2.3 (b). If the temperature reaches absolute zero, the population of magnons is rapidly decreased, which results in a drastic decrease of signal for the Anti-Stokes process. On the other hand, the Stokes signal remains almost unchanged. Other asymmetries can arise, because of other effects, such as localization of some modes of a spin wave on a specific surface [57–59].

## 2.3. Interferometers for measuring BLS

Two main approaches for measuring Brillouin spectra are used. They differ in the spectrometer used for scattered light analysis. The Virtually imaged phased array is mainly used in biological applications, while the Tandem-Fabry-Perot technique is prevalently used in material science.

### 2.3.1. Virtually imaged phased array Brillouin light scattering

This setup uses a Virtually imaged phased array (VIPA) for resolving the frequency shifts. VIPA is a device that angularly separates the light in the dependence on its frequency, similar to a prism or diffraction grating. In comparison with regular diffraction grating or prism, it has a much smaller free spectral range (FSR), which is the range of detectable frequency shifts, but it can resolve smaller shifts [61]. Typically, FSR for VIPA BLS setups is around 30 GHz [60].

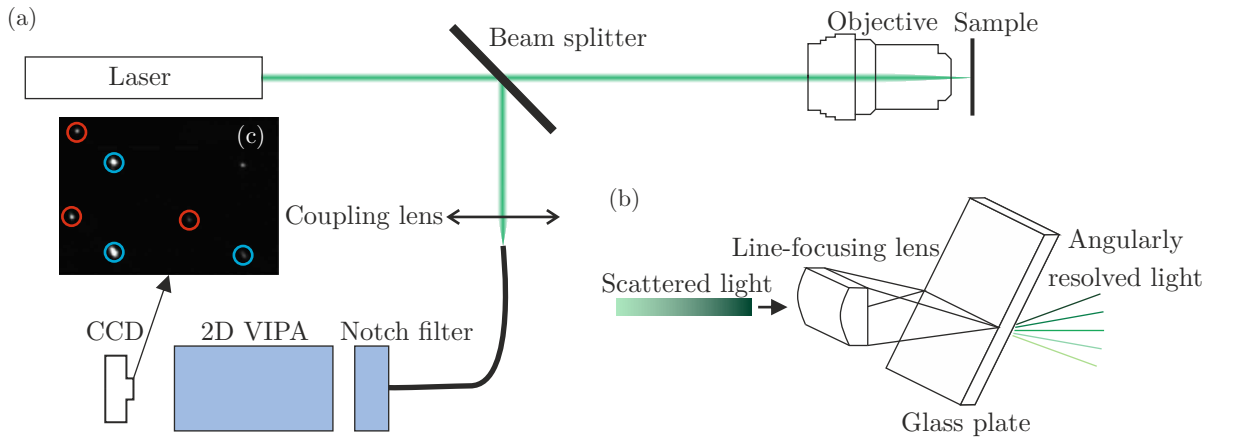


**Figure 2.4:** (a) Schematic of whole VIPA setup for measuring Brillouin spectra. (b) Working principle of VIPA. (c) Experimentally observed image on CCD camera of acetone [60]. Stokes (anti-Stokes) peaks are marked with red (blue) circles. Elastic peak is not visible because this peak is suppressed in notch filter.

The schematic of the whole setup is shown in Figure 2.4 (a). Usually, a green laser with the wavelength of 532 nm is used. It passes through a beam-splitter to the microscopic objective, which focuses the light to a spot on the sample. On the sample, the light is back-reflected and passes the objective again. The back-scattered light is coupled to the fiber, which goes through a notch filter where the elastically scattered light (Rayleigh line) is suppressed. This filter consists of a heated cell with iodine gas (in the case of the 532 nm laser). Then frequencies are angularly divided in the 2D VIPA. The 2D VIPA consists of a glass plate, which is tilted with respect to the incident light, as can be seen in Figure 2.4 (b). In contrast to the diffraction grating, the VIPA creates phase array in the virtual image, which allows us to observe the interference. After the VIPA, the image is recorded in the CCD/CMOS. An example of such an image is shown in Figure 2.4 (c). To interpret this image, further analysis is required [62]. This involves the identification of Rayleigh line, filtering, and extraction to a line graph.

Typically achievable contrast<sup>1</sup> in the VIPA BLS is in the order of 55 dBm [63]. The main advantage of the VIPA BLS is fast acquisition time, which is in the order of milliseconds [63]. This makes VIPA BLS a useful tool for investigating samples, which are not in an equilibrium state or suffer from heating induced by laser.

### Applications of VIPA BLS

The acquisition of single spectra takes hundreds of millisecond [64], thus it is an optimal technique for imaging of cells and slowly moving (drifting) objects. In Figure 2.5 (a) the 2D image of sheath cells from zebrafish is shown [64]. This measurement was performed *in vivo*, where the acquisition speed is crucial. From the magnitude of the Brillouin shift, one could deduce the mechanical properties of the extracellular matrix (ECM), which is apparent between the vacuole and surrounding muscle. Another application of the VIPA BLS is in clinical testing for keratoconus (thinning of the cornea). It was shown that

<sup>1</sup>In interferometry contrast means the ratio between the highest signal (usually Rayleigh line) and the lowest detectable signal (e.g. Brillouin signal).

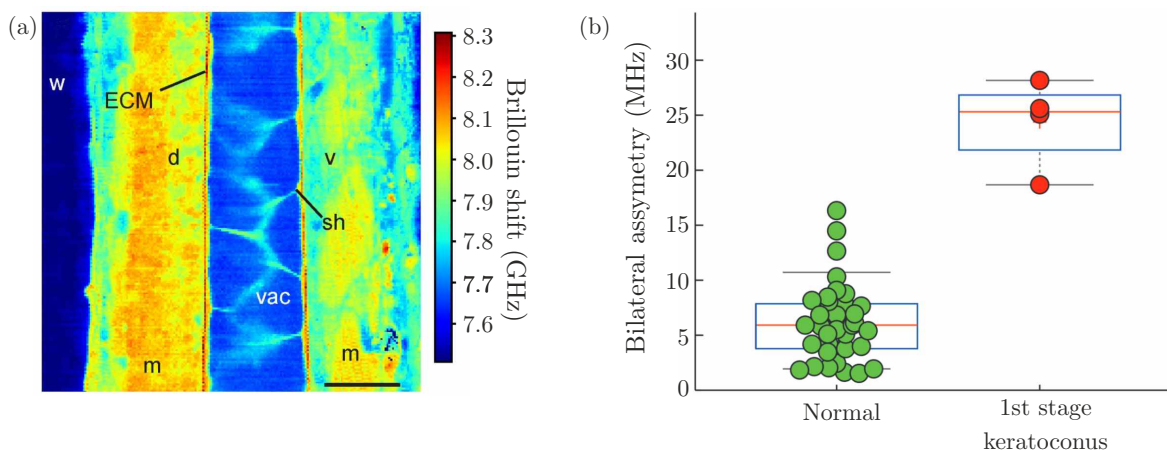


**Figure 2.5:** (a) 2D map of Brillouin shift of sheath cells from zebrafish. The scale bar in the down right corner is equal to 20  $\mu\text{m}$ . Taken from [64]. (b) Differences in Brillouin frequency between left and right eye for normal people and with 1st stage of keratoconus. The orange bars show mean value, while the gray bar shows standard deviation. Taken from [65].

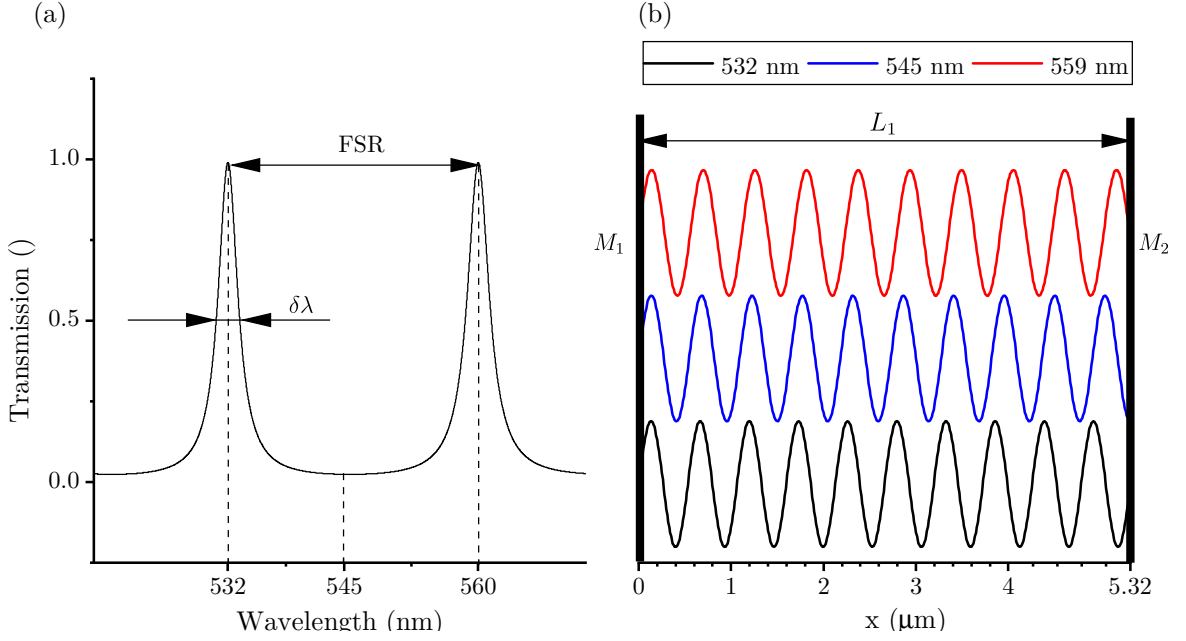


**Figure 2.6:** (a) Transmission of single FP. The parameters are  $\tau_0 = 0.99$ ,  $F = 10$  and  $L_1 = 5.32 \mu\text{m}$ . The corresponding FSR is shown. (b) The cavity of FPi. Black and red curve are standing waves, where transmission maxima occurs. The blue curve is in the middle where almost not any intensity can pass.

patients with the first stage of keratoconus disease have a significant change in Brillouin frequency between their left and right eye, as is shown in Figure 2.5 (b) [65, 66].

### 2.3.2. Fabry-Perot Brillouin light scattering

The second approach uses a Fabry-Perot interferometry. Fabry-Perot interferometer (FPi) consists of two parallel mirrors with high reflectivity, which are separated by a distance of  $L_1$ . The transmission through FPi can be expressed as [67, p. 5]

$$T = \frac{\tau_0}{1 + (4F^2/\pi^2) \sin^2(2\pi L_1/\lambda)}, \quad (2.11)$$

where  $\tau_0$  is the maximum possible transmission determined by losses of the system and  $F$  is the finesse of the mirrors. The finesse depends on flatness and reflectivity of the used mirrors. The transmission in dependence on the wavelength of light is plotted in Figure 2.6 (a). The distance between two transmission maxima is called free spectral range (FSR) and is given by

$$\text{FSR} = \frac{\lambda^2}{2L_1}. \quad (2.12)$$

The full width at half maximum is  $\delta\lambda$ , which is usually called resolution. From these two variables we can compute the finesse

$$F = \frac{\text{FSR}}{\delta\lambda}. \quad (2.13)$$

The peak in the transmission occurs when a standing wave is formed, so the cavity length is equal to an integer multiply of the wavelength. These cases are shown as the black and red lines in Figure 2.6 (b). On the other hand, if this condition is not fulfilled, the

transmission is suppressed. This is shown by the blue line in Figure 2.6 (b). To resolve the frequencies of the transmitted light, one mirror is on a piezo attenuator and the length  $L_1$  is varied in the range of one FSR. To increase the FSR, one has to decrease the cavity length  $L_1$ , but this will also increase  $\delta\lambda$ . So the resolution is increased as a trade-off with measurement range.

### Tandem Fabry-Perot interferometer

To overcome this issue A. S. Pine joined two FPIs in series [68], which increased FSR, with the same resolution. The resulting transmission is the convolution of transmission functions of both interferometers. The transmission functions dependencies on the wavelength are shown for two cavity lengths  $L_1 = 5.32$  mm and  $L_2 = 5.05$  mm in Figure 2.7 (a) and (b). The cavity length  $L_2$  is exactly 90 % of  $L_1$ . The corresponding FSR are 281 MHz for  $L_1 = 5.32$  mm and 296 MHz for  $L_2 = 5.05$  mm, which is visible in Figure 2.7 (d) and (e). The  $x$ -axis is shown as a frequency shift from 532 nm. The transmission maximum occurs for both cavity lengths at 0 frequency shift, but the neighboring maxima are shifted by 15 MHz. When we perform convolution of these functions, these neighboring maxima are suppressed, as can be seen in Figure 2.7 (c). After 20 FSRs of FPI<sub>1</sub> and 19 FSRs of FPI<sub>2</sub>, there is again a coincidence of transmission maxima and the light can pass through both FPIs. This spectral distance will be called FSR of tandem Fabry-Perot interferometer (TFPI) and in this case, it will be 5.63 GHz, as can be seen in Figure 2.7 (f).

The transmission does not go directly to zero, but small so-called ghosts remain in the spectrum. These ghosts are visible in a detailed picture of the TFPI transmission function. Again the  $x$ -axis represents the frequency shift from 532 nm. The  $y$ -axis is zoomed to the region near zero transmission. The transmission of these ghosts is higher in the vicinity of the central peak and they are in a maximum of 1 %.

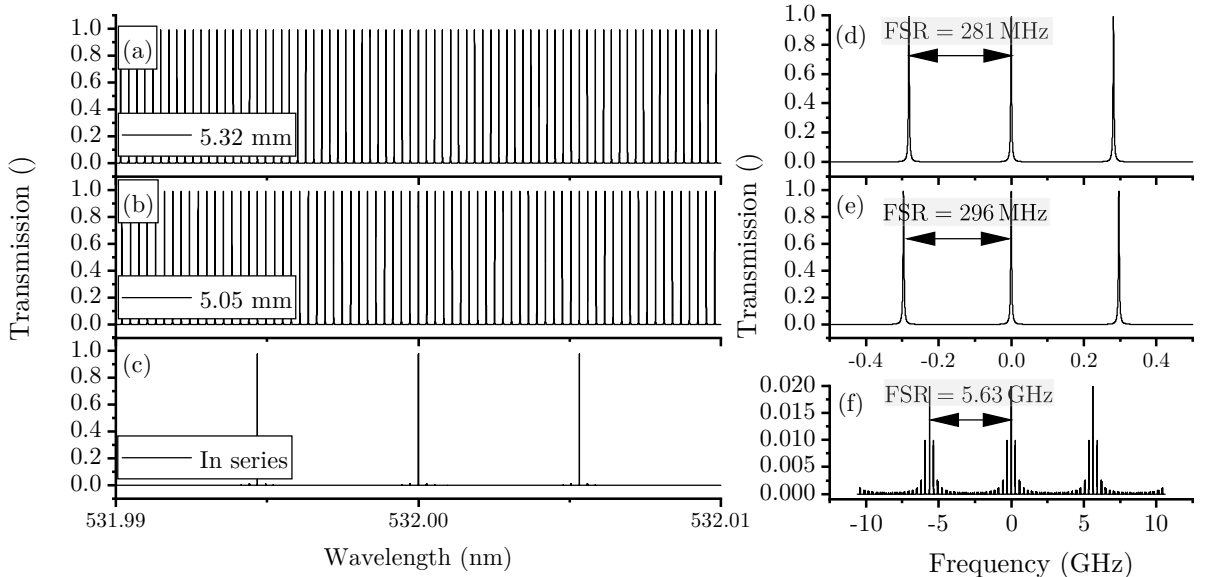


**Figure 2.7:** (a), (b), (c) Transmission depending on the wavelength for FPIs with (a)  $L_1 = 5.32$  mm, (b)  $L_1 = 5.05$  mm and (c) both in tandem operation. (d), (e) and (f) detail of (a), (b) and (c).

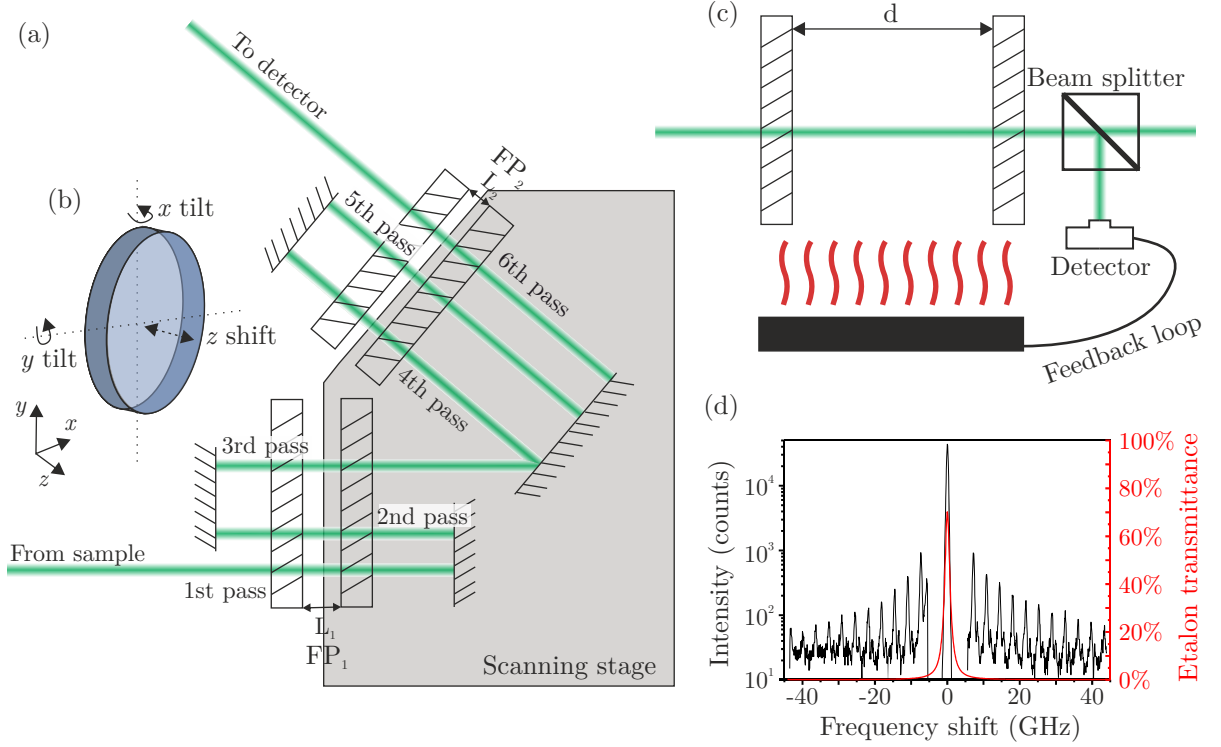


**Figure 2.8:** (a) Schematic of the six-pass Tandem Fabry-Perot interferometer. (b) The schematic of the mirror and its degrees of freedom, which are compensated by piezo actuators. (c) Schematic of the Fabry-Perot etalon with cavity length change based on the heating by Peltier element. (d) The black curve represents the spectra of commercial laser obtained by the TFPi. The red curve represents the theoretical transmission function of etalon developed by J. Sandercock.

To use the TFPi as a spectrometer, synchronous scanning of both FPIs is essential. The increments of cavity lengths of both FPIs have to fulfill this ratio

$$\frac{\delta L_1}{\delta L_2} = \frac{L_1}{L_2}, \quad (2.14)$$

where  $\delta L_1$  and  $\delta L_2$  are changes in cavity lengths.

This can be done by changing the optical path between mirrors with a change of pressure, thus refractive index of filled gas [69]. But usually, it is not possible to achieve big enough change in pressure and the corresponding change in optical length.

J. Sandercock came with a stable mechanical solution, where both FPIs share the same scanning stage [70–72]. The first FPI is in the direction of the scanning stage. The second FPI is tilted by a fixed angle  $\vartheta$ .

The change in cavity length  $L_1 = \Delta$  will result in change in  $L_2 = \Delta \cos \vartheta$ . This relationship will satisfy the equation (2.14).

To further improve contrast, the light is guided several times through FPI in different positions of mirrors. In the case of the TFPi designed by J. Sandercock, three passes through each FPI are realized, as is depicted in Figure 2.8 (a).

Another challenge is to keep mirrors parallel during long measurements, because of thermal fluctuations and mechanical vibration. This was solved by the active stabilization of mirrors during measurement. The two moving mirrors have piezo actuators for compensation of tilt and  $z$  shift, as is depicted in Figure 2.8 (b). Also, the cavity lengths of both

FPis are compensated with respect to each other and the position of elastic laser peak. These piezo are optimized depending on the strength of the so-called reference beam. This beam is divided by beam-splitter from the main source of light and then guided to TFPi. During the scanning of TFPi, the input shutter continuously switches between the sample signal and this reference beam to maintain the stability of the measurement.

To be able to resolve and correctly interpret the signal, a coherent and stable light source is needed. Usually, solid-state lasers are used. The laser has to have the only first transverse mode (TEM00) and any higher mode of operation (laser modes) have to be suppressed. To further suppress these modes, a Fabry-Perot etalon can be placed after the laser to act as a narrow band-pass filter.

In the solution developed by J. Sandercock, the cavity length of the etalon is changed via heating using the Peltier unit, as is shown in Figure 2.8 (c). This system is also actively stabilized with a feedback based on the transmission of the laser light. The spectra of a commercially available laser source together with the theoretical transmission function of the etalon, are shown in Figure 2.8 (d).

## 2.4. $k$ -resolved Brillouin light scattering

This technique is used for the measurement of BLS spectra with a specific  $k$ -vector. Back-scattering geometry is used, as is shown in Figure 2.2 (c). Due to the low signal strength, it is necessary to use a lens for focusing and collecting the light. This will blur the resolution in  $k$ -space but increase the signal dramatically.

Because of the used back-scattering geometry, the incident and scattered light share the same beam path. The separation can be realized either with beam-splitter or with a so-called catching-mirror. The catching mirror can couple all the light from the laser source onto the sample, and approximately 90 % of scattered light passes to TFPi. This is possible because the diameter of the laser beam is in order of hundreds of micrometers,

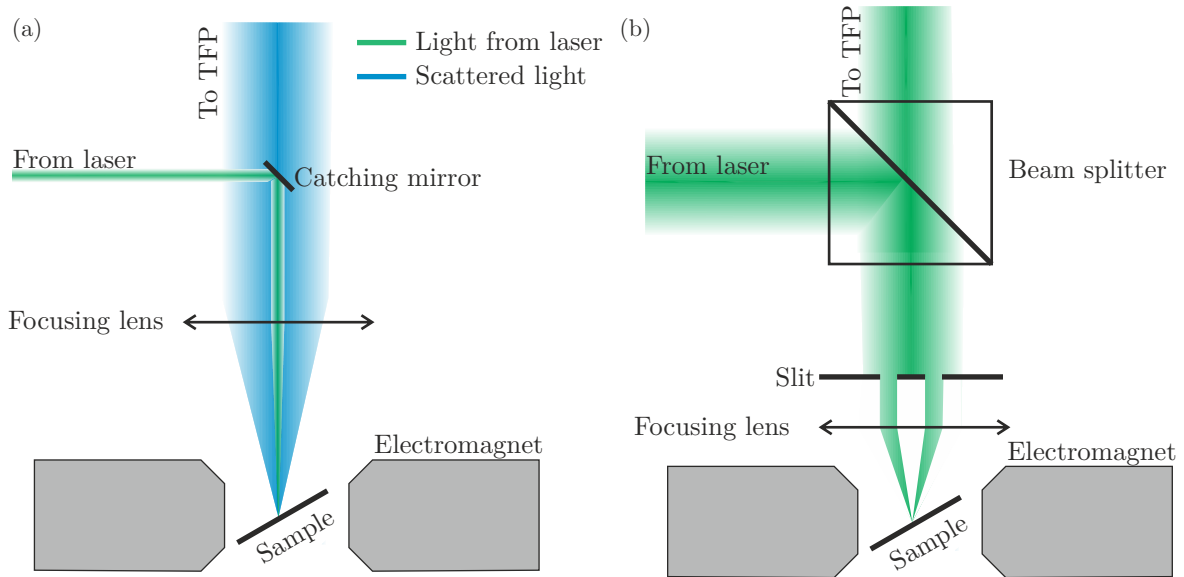


**Figure 2.9:** (a) The schematic of  $k$ -resolved setup, which uses the tilting of the sample. (b) The large aperture BLS setup schematic.

and after reflecting from catching mirror and after scattering, it is usually expanded for two-inch optics (52 mm), and only the small center area is lost.

It is a very challenging task to design a setup that allows convenient changing of the sample and simultaneously easy change of the angle of incidence. To tackle this challenge, two main approaches are used.

### 2.4.1. Tilting of sample approach

The first approach uses the tilt of the sample. The focusing lens has a focal point in the order of tens of millimeters [73]. The schematic of the setup is shown in Figure 2.9 (a). If the central point of the rotation is not coincidental with the laser spot on the surface of the sample, the focus has to be found after each change of the tilt of the sample. The focus is usually found with the thermal spin-wave signal strength in the TFPi. This procedure requires a lot of time, thus measuring a lot of  $k$ -vectors could be cumbersome, but on the other hand,  $k$ -resolution is limited only by the selection of the lens. The  $k$ -resolution can be improved by using a lens with a smaller numerical aperture, but this will sacrifice the signal strength.

### 2.4.2. Large aperture approach

The second approach uses a diaphragm and a lens with short focal length [74]. The laser light irradiates the sample with a variety of angles because of the high numerical aperture of the used lens. After the scattering, the laser beam passes through a diaphragm with a changeable diameter. The schematic of the setup is shown in Figure 2.9 (b). The maximal detectable  $k$ -vector is set depending on the opening of the diaphragm.

The selectivity of the direction of spin waves can be implemented by employing a narrow slit. This slit is mounted in a rotatable holder, which allows an easy change of the detected direction of spin waves. The resolution is affected by the width of the slit.

### 2.4.3. Applications of $k$ -resolved BLS

This chapter will discuss the typical applications of  $k$ -resolved BLS. In the past, the main focus was in material properties and the investigation of dispersion relations. Nowadays, the main focus is shifted to the Dzyaloshinskii-Moriya interaction studies.

#### Material properties

$k$ -resolved BLS can be used for obtaining dynamic magnetic properties of material [76, 77]. In this type of measurement, BLS thermal spectra are acquired for different angles of incidence ( $k$ -vectors of spin waves). For each angle of incidence, a sweep of the external field is performed. These points are then fitted with a model based on the calculation of the dispersion relation.

This could be used for the measurement of the change of magnetic properties in multi-layer systems [75]. Measured data for a system of cobalt layers and palladium spacers are shown in Figure 2.10 (a). This data was fitted with a theoretical model, and parameters such as saturation magnetization, gyromagnetic ratio, or layer thickness were obtained.

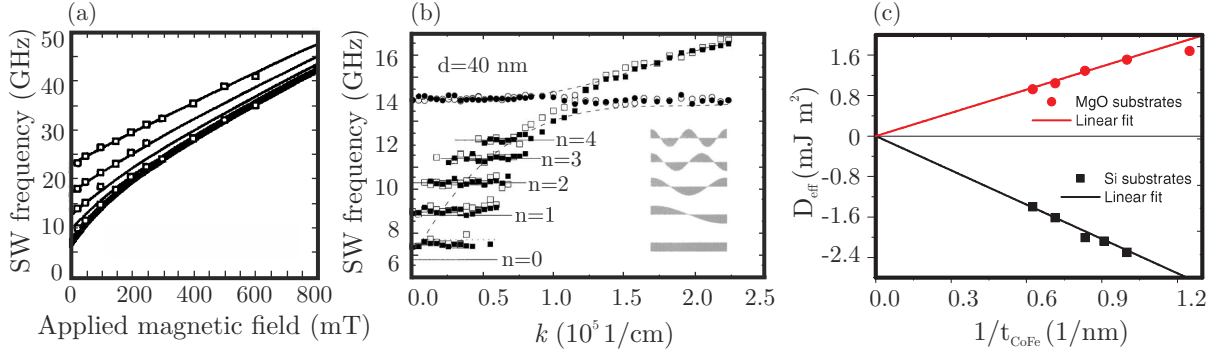


**Figure 2.10:** (a) Measured data (squares) and fitted model (solid curves) of spin-wave frequencies vs. applied field. The measured multi-layer system consists of 10 bilayers of 10 nm Co layer, and 12 nm Pd layer. Adapted from [75]. (b) Measured and calculated dispersion relation of the array of magnetic permalloy wires. The thickness was 40 nm, the wire width  $1.8 \mu\text{m}$  and gap between them  $0.7 \mu\text{m}$  (open symbols) and  $2.2 \mu\text{m}$  (solid symbols). (c) The strength of DMi constant in dependence of layer thickness. Solid lines are linear fits of experimental data.

### Dispersion relation

Even dispersion from more complex systems such as microstructures [78, 79], or magnonic crystals [80–82] can be investigated. In a study conducted by Jorzick et al. [83], the dispersion of an array of permalloy wires was investigated. The wires were 40 nm thick, with a width of  $0.7 \mu\text{m}$ . In Figure 2.10 (b), the first two thickness modes are visible. Moreover, four other width modes are apparent.

### DMI measurement

Since Dzyaloshinskii-Moriya interaction (DMI) [84] causes non-reciprocity of dispersion in both, direction of magnetic field and spin waves, it is possible to measure its strength with  $k$ -resolved BLS [85–88]. By observing the value of the frequency shift with fixed  $k$ -vector during external field reversal, the strength of DMi could be resolved.

In work done by Belmeguenai [89], the dependency of DMi on the thickness of  $\text{Co}_{0.5}\text{Fe}_{0.5}$  ultrathin layers was investigated. The result is shown in Figure 2.10 (c). It is apparent that with increasing thickness of the layers, the strength of DMi becomes larger (smaller) for Si (MgO) substrate.

## 2.5. $\mu$ BLS

If we use an objective with a high numerical aperture instead of the focusing lens, a bunch of  $k$ -vectors will be probed at the same time, as is shown in Figure 2.11 (a). One cannot distinguish between the different  $k$ , or between different directions of spin waves. But it is possible to get information about the density of states. On the other hand, the spatial resolution is increased, and it is only limited by the diffraction limit of the used light.

To properly understand the signal from  $\mu$ BLS one can consider this relationship for BLS cross section

$$\sigma_{\mu\text{BLS}} \sim \frac{1}{\exp(\frac{\hbar\omega_{\text{SW}}}{k_{\text{b}}T}) - 1} D(\omega), \quad (2.15)$$

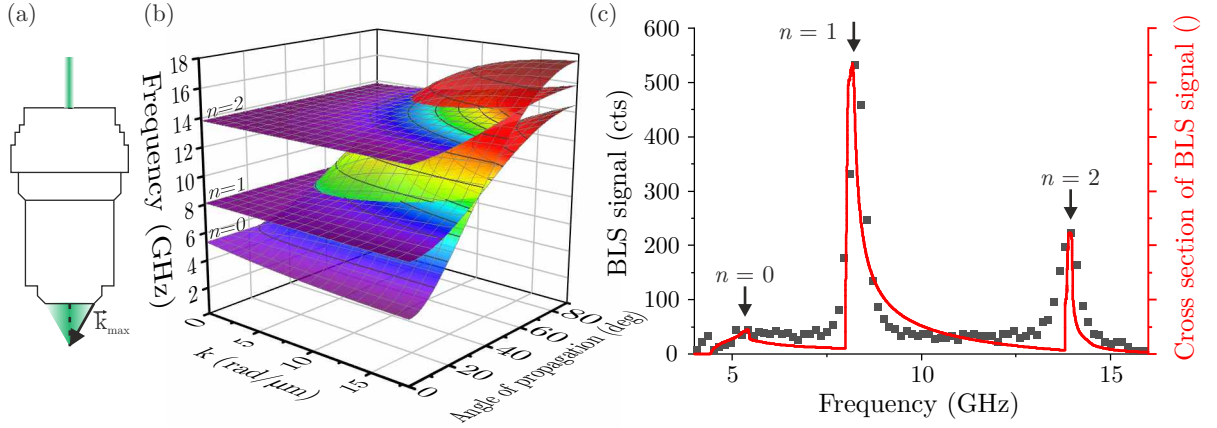


**Figure 2.11:** (a) Schematic of  $\mu$ BLS objective. (b) Calculated dispersion relation of spin waves in 82 nm permalloy thin film. (c) The measured and modeled cross section of  $\mu$ BLS for permalloy layer with thickness 82 nm. The thickness modes are marked by arrows.

where  $D(\omega)$  is density of states of spin waves and  $\omega_{\text{SW}}$  is spin-wave frequency. The dispersion for permalloy layer with the thickness of 82 nm calculated for frequencies ranging from 1 to 18 GHz is shown in Figure 2.11 (b). In this frequency range we can see three thickness modes. From this dispersion relation we compute group velocity as

$$v_g = \frac{\partial \omega}{\partial k}, \quad (2.16)$$

for each individual thickness mode. From the group velocity, one can obtain the density of states [90, p. 110]

$$D(\omega)d\omega = \frac{V}{8\pi^3} \frac{1}{v_g} d\omega, \quad (2.17)$$

where  $V$  is volume. Because the equation 2.15 gives only proportional value, we can use the following equation:

$$D(\omega)d\omega \sim \frac{1}{v_g} d\omega. \quad (2.18)$$

The density of states is numerically computed for all angles of propagation and the three lowest thickness modes and numerically integrated. This density of states [ $D(\omega)$ ] is then used for calculation of the theoretically modeled cross section which is shown in Figure 2.11 (c). In the frequency around 5 GHz the first ( $n = 0$ ) thickness mode is visible. The higher thickness modes ( $n = 1$  and  $n = 2$ ) are visible around 8 GHz and 14 GHz. The measured data for the same system are shown as black squares, showing good agreement with the theoretical prediction.

### 2.5.1. Applications of $\mu$ BLS

Nowadays, the  $\mu$ BLS is a crucial tool in spin-wave research because of its versatility and easiness of measurements. The applications of  $\mu$ BLS in the investigation of waveguides, magnonic crystals, guiding of spin waves, spin-wave splitters, amplifiers, and spin-wave sources will be discussed in the following sections.

## Spin-wave waveguide

The diffraction-limited resolution allows for a spatial investigation of spin-wave waveguides with widths in the order of several micrometers. The study of two counter-propagating spin waves was utilized in [91]. Spin waves were emitted from two antennas separated by a  $14\ \mu\text{m}$  long gap. The interference pattern was observed, as is shown in Figure 2.12 (a). These measured data were confirmed by the micromagnetic calculation which is shown in Figure 2.12 (b).

The excitation and propagation of spin waves with the wavevector confined to the width of the waveguide (waveguide modes) were studied in [27, 93]. The interference patterns, which are caused by this mode beating, were investigated in [94].

The external magnetic field generated by passing an electric current in a conductor beneath the magnonic waveguide can change the magnetic state of the whole system. This behavior could be used for steering of spin waves [92] as can be seen in Figure 2.12 (b), (c). The branch with applied DC is in Damon-Eshbach like geometry, thus spin waves prefer this branch over the other one, which is in backward volume geometry. Furthermore, the spin waves could be guided by, e.g., changes in the width of waveguide [34, 95] or led by curved waveguide [96, 97].

## Magnonic crystals

As the signal from  $\mu$ BLS is proportional to the density of states of spin waves, this technique can be used for measuring band gaps of magnonic crystals [98, 99]. The band gaps would be apparent as a drop of BLS signal in forbidden frequencies, as can be seen in Figure 2.13 (a). The presented crystal was created with ion irradiation of the permalloy layer, which caused periodic modulation of the saturation magnetization.

## Guiding of spin waves

The guiding of spin waves with sufficient propagation length is a big challenge. Flajsman et al. [41] achieved this in zero magnetic field with the use of the metastable iron system,

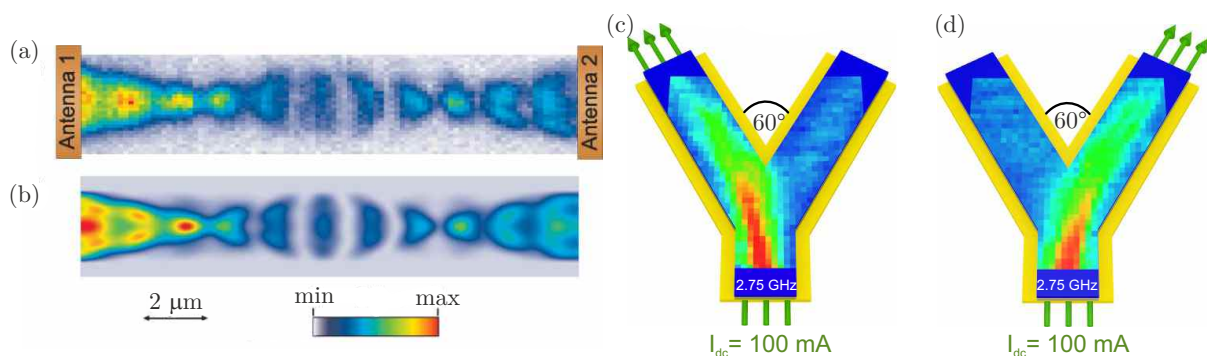


**Figure 2.12:** (a) Measured 2D map of the interference pattern from two counter-propagating spin-wave beams. Both beams are excited by antennas, which are shown as orange rectangles. (b) Calculated pattern of interfering spin waves for modes with  $n = 1, 3, 5, 7$ . Both figures are taken from [91]. The  $\mu$ BLS intensity maps of permalloy waveguides for DC applied in the left (c) and right (d) branch of the underlying electric waveguide. Taken from [92].

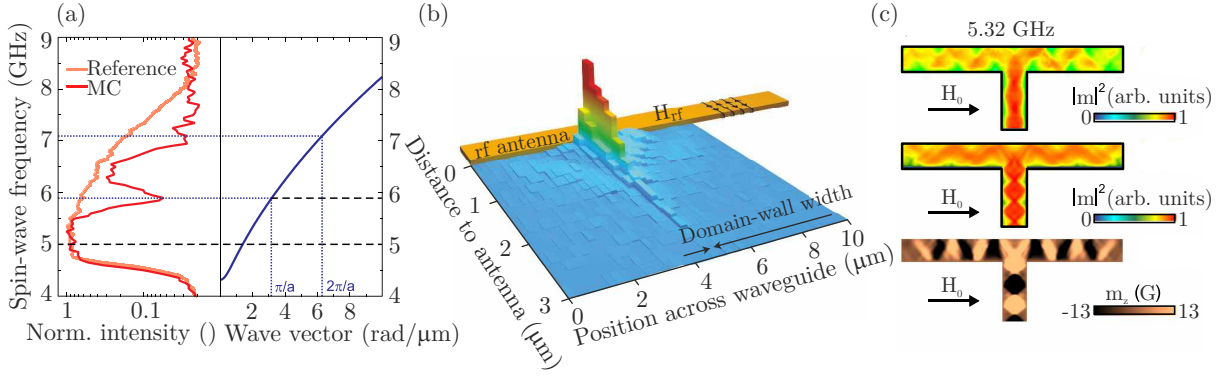


**Figure 2.13:** (a) In the left panel  $\mu$ BLS signals of reference permalloy layer and magnonic crystal with modulated saturation magnetization are shown. In the right panel, analytically calculated dispersion relation for the corresponding thin layer of permalloy is shown. The boundaries of the two Brillouin zones are marked. Taken from [98]. (b) Two-dimensional distribution of BLS intensity of spin waves coupled into a Néel domain wall. Taken from [100]. (c) T-based magnonic beam splitter realized with YIG waveguides. Taken from [101].

where uniaxial magnetic anisotropy can be imprinted. In these circumstances, Damon-Eshbach like propagation could be achieved even in a narrow magnetic waveguide without the use of the external field.

Another approach is to couple spin waves into topological waveguides such as Néel domain walls [100, 102]. This is shown in Figure 2.13 (b), where spin waves are excited with a microstrip antenna and then propagate in a nanochannel created by the Néel domain wall.

### Spin-wave splitters

Another difficult task is the splitting of spin-waves beams in magnonic circuitry. The T-based spin-wave beam splitter was demonstrated in YIG [101, 103]. The measured BLS intensity is shown in Figure 2.13 (c) in the upper panel. The middle panel shows the spin-wave intensity obtained from the micromagnetic simulation. The lower panel shows a snapshot of out-of-plane magnetization.

### Spin-wave amplifiers

To have sufficient signal even after the splitting of spin-wave beams, amplification is needed. The spin waves exhibit parametric pumping, which can be used for this purpose [104, 106, 107]. In the case shown in Figure 2.14 (a), the spin waves are amplified by the external magnetic field created by the underlying electric waveguide. In the position of the amplification area, the lateral dimension of the waveguide is restricted, thus the current density is remarkably increased. This results in the higher amplitude of the magnetic amplification field in this area and amplification of spin-wave intensity, as can be seen in Figure 2.14 (b).

### Spin-wave sources

Also, the integration of spin-wave circuits into DC CMOS technology is possible through spin Hall nano oscillators (SHNO) [105, 108]. In Figure 2.14 (c), a schematic of the

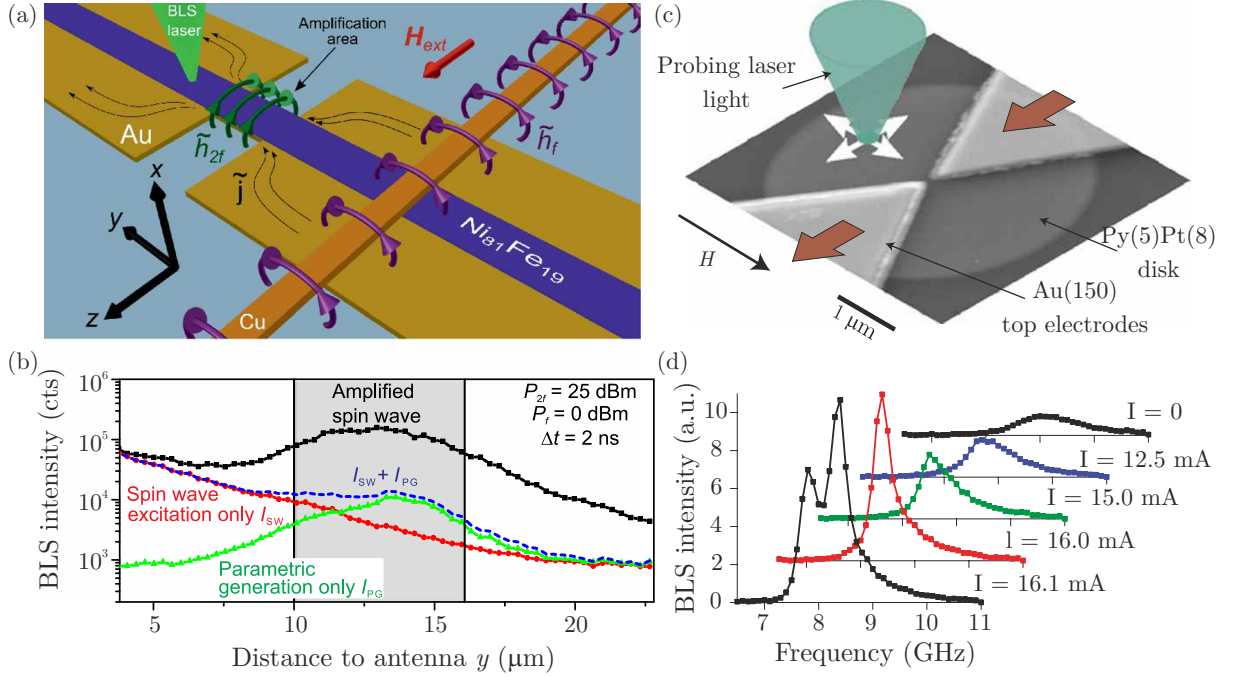


**Figure 2.14:** (a) Schematic of parametric amplification of spin waves. The blue rectangle is permalloy magnonic waveguide. Spin waves are excited in a copper microstrip antenna. The alternating current with twice higher frequency than the frequency of spin-wave is flowing through a golden pad under the permalloy waveguide. (b) Measured BLS intensity for cases with only excited spin waves (red curve), only parametrically pumped spin waves (green curve), the numerical summation of these two is (blue curve) and both cases combined (black curve). Both figures are taken from [104]. (c) Experimental schematic of the generation of spin waves through spin-transfer torque. The BLS intensities measured for different DC, as is shown in panel (c). Taken from [105].

experimental realization of SHNO is presented. DC is applied to the gold electrodes. Spin waves are then emitted to the direction perpendicular to current flow and probed by means of  $\mu$ BLS. The measured BLS intensities for different current values are shown in Figure 2.14 (d).

## 2.6. Phase-resolved $\mu$ BLS

In  $\mu$ BLS, the  $k$ -resolution is sacrificed in order to achieve a high spatial resolution. The objective with high numerical aperture integrates over a wide variety of angles, as was discussed in section 2.5. This sacrifice allows achieving a high, diffraction-limited resolution. However, the Brillouin light scattering is a phase-sensitive process, thus a phase information can be obtained from spin waves. To get this information, another reference signal with the same frequency, sufficient coherency, and constant phase has to interfere with the inelastically scattered light. This allows observing an interference pattern between these two signals which can be used for an investigation of the spin-wave phase. This experimental technique was developed in the research group led by prof. Hillebrands [109, 110].

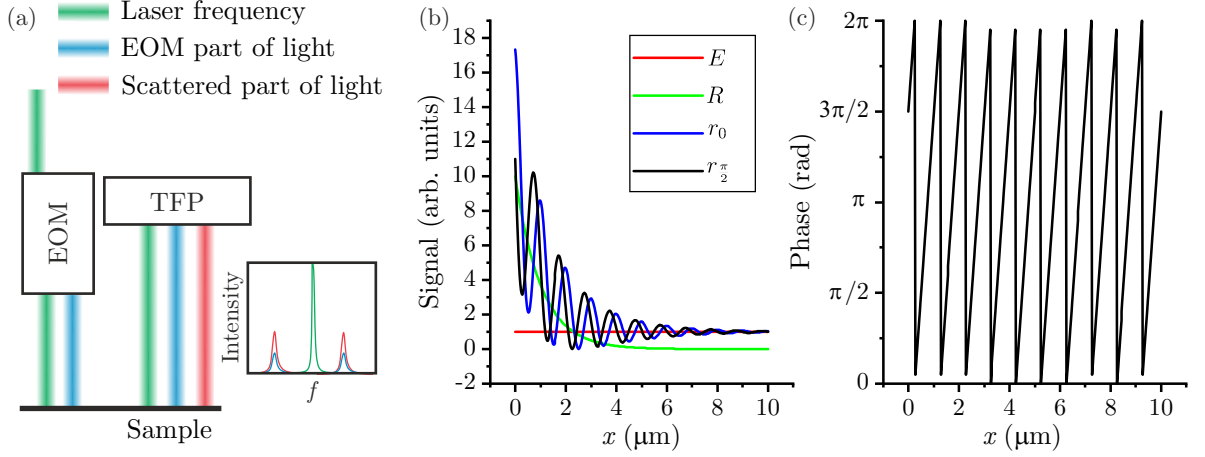


**Figure 2.15:** (a) Schematic of the phase-resolved BLS setup. (b) The four analytically modeled signals necessary for obtaining full phase from BLS measurements. The red curve is signal only from EOM, the green curve is intensity measurement, and blue and black curves are interference measurements, which are shifted with respect to each other by  $\frac{\pi}{2}$ . The modeling of these signals is discussed in appendix D. (c) Extracted phase from signals in panel (b) based on equation 2.19.

To add the reference signal, an electro-optical modulator (EOM) is added to the laser beam path before the microscope. The schematic of the phase-resolved setup is shown in Figure 2.15. The EOM is driven with the same frequency as the spin waves. This is realized by a 3 dB divider, which is placed after the high-frequency generator. A small fraction of the light is modulated in the EOM and shares the same beam path as the light with unchanged frequency. Then both parts are reflected from the sample, where a part of the laser light is shifted to the same frequency as the electrically modulated light, but the phase is affected by the spin-wave phase. These two signals then interfere on the detector.

The phase of the electrically modulated light can be changed via a phase shifter, which is placed between the power divider and the EOM. To reconstruct the full phase of spin waves, four measurements must be done. These are: two interference patterns between the EOM and the spin wave signal ( $r_0$  and  $r_{\pi/2}$ , which are shifted by  $\pi/2$  with respect to each other), the signal only from spin waves ( $R$ ) and the EOM signal ( $E$ ). Thus, for the experimental realization we need two RF switches. One switch controls the excitation of spin waves, while the second controls the EOM. If both switches are on, the interference pattern can be measured. If only the switch to the EOM is turned on, the intensity of electrically modulated light is measured and in the last case (only spin wave excitation), the exponential spin wave decay is measured. The analytic model of these data is shown in Figure 2.15 (a). The complex spin wave is then calculated as

$$\text{Re} \{ \Psi_{\text{SW}}(x) \} = \frac{r_0(x) - R(x) - E(x)}{2\sqrt{E(x)}}, \quad (2.19a)$$

$$\text{Im} \{ \Psi_{\text{SW}}(x) \} = \frac{r_{\pi/2}(x) - R(x) - E(x)}{2\sqrt{E(x)}}, \quad (2.19b)$$

where  $\Psi_{\text{SW}}$  is the complex wave function of the measured spin wave. From these two components the phase  $\Phi_{\text{SW}}$  is then obtained from the following formula

$$\Phi_{\text{SW}} = \text{atan} \left( \frac{\text{Im}}{\text{Re}} \right) + s\pi, \quad (2.20)$$

where  $s = 0, \pm 1$  and it depends on the quadrant of the complex spin wave. To calculate the wave vector for the single-mode spin wave, the dependency of the phase on the distance from the source has to be measured. The modeled phase of the plane wave single-mode spin-wave is shown in Figure 2.15 (b). The distance between two phase-jumps is equal to the wavelength of the spin wave. To perform a linear fit of the phase  $\Phi$ , which will reveal the  $k$ -vector, the measured phase has to be unwrapped. This means that the multiples of  $\pi$  have to be added when the phase reaches 0 or  $2\pi$ . The  $\Phi_0$  stands for the offset of phase and has no physical meaning. The calculated unwrapped phase is shown in Figure 2.15 (c). As such treated data should look like a linear increase or decrease, depending on the direction of the phase shift between two interference patterns. The following equation is used for fitting

$$\Phi = \Phi_0 + kx, \quad (2.21)$$

where  $\Phi_0$  stands for the offset of phase and has no physical meaning.

However, the spin-wave wavelength can be also obtained with a single interference linescan ( $r$ ). In this case, the measured data are fitted with the following model

$$r(x) = R(x) + E(x) + \sqrt{2R(x)E(x)} \cos \left( 2\pi \frac{x}{\lambda} + \Phi_0 \right), \quad (2.22)$$

where  $E(x)$  can be assumed as a constant for homogeneous samples,  $\lambda$  is the wavelength of spin waves,  $\Phi_0$  is the phase offset and the  $R(x)$  is assumed as exponentially decaying function

$$R = R_{\text{max}} \exp \left( -\frac{x}{l_{\text{att}}} \right), \quad (2.23)$$

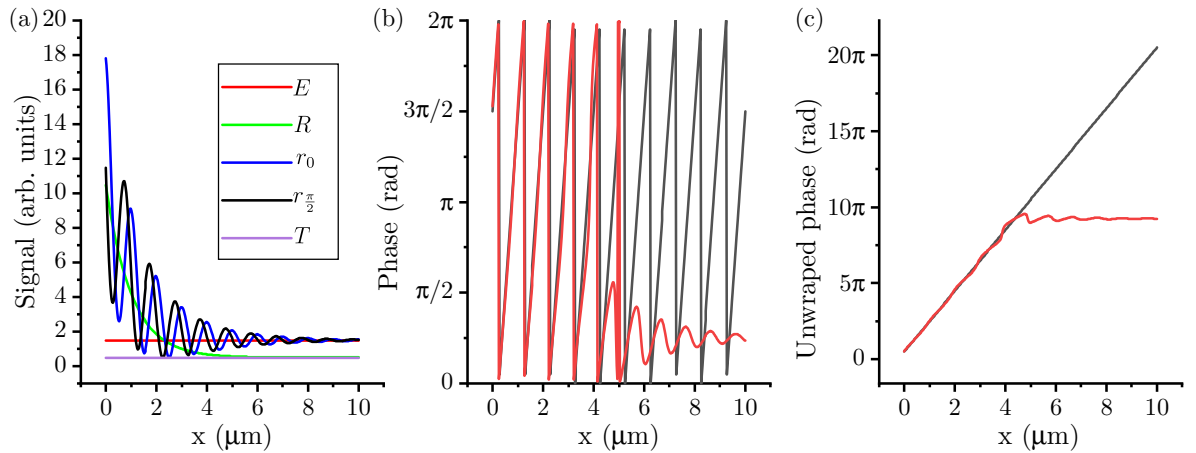


**Figure 2.16:** (a) The five analytically modeled signals used for obtaining full phase from BLS measurements. Red curve is signal only from EOM, green curve is intensity measurement, blue and black curves are interference measurements, which are shifted in respect to each other by  $\frac{\pi}{2}$  and the violet curve represents the incoherent thermal signal. The modeling of these signals is discussed in appendix D. (b) Extracted phase from signals in panel (a) based on equation 2.24 (red curve) and 2.19 black curve. (c) Unwrapped (added multiples of  $\pi$ ) phase from panel (b).

where  $R_{\max}$  is the maximum of spin wave intensity and  $l_{\text{att}}$  is the propagation length. If a sample with non-homogeneous reflectivity is measured, the BLS linescan with only EOM signal switched on can be measured and plugged into the fit.

In the samples where signal from the incoherent thermal magnon excitation is strong, it is necessary to take this into account. There will be an offset in each of the four measured signals. The thermal linescan ( $T$ ) with all switches off has to be measured and then subtracted from remaining signals. In this circumstances the equation 2.19 will be as follows

$$\text{Re} \{ \Psi_{\text{SW}}(x) \} = \frac{r_0(x) - R(x) - E(x) + T(x)}{2\sqrt{E(x) - T(x)}}, \quad (2.24a)$$

$$\text{Im} \{ \Psi_{\text{SW}}(x) \} = \frac{r_{\frac{\pi}{2}}(x) - R(x) - E(x) + T(x)}{2\sqrt{E - T(x)}}. \quad (2.24b)$$

The five modeled signals ( $E$ ,  $R$ ,  $r_0$ ,  $r_{\frac{\pi}{2}}$  and  $T$ ) with thermal signal taken into account are shown in Figure 2.16. In Figure 2.16 (b) the calculated phase is shown. The black line is calculated following equation 2.19, whereas the red line is calculated with the use of 2.24. The unwrapped phases of both calculations are shown in Figure 2.16 (c). The phases are similar when the thermal signal is low in comparison with the spin-wave signal. When the thermal signal starts to be significant, the calculated phase according to 2.19 starts to converge to a constant value. But even in the case of subtraction of the thermal background, the computation of the phase is limited by the signal to noise ratio.

### 2.6.1. Application of phase-resolved $\mu$ BLS

As was already discussed in section 2.6, the phase resolved Brillouin light scattering can be used to obtain the dispersion relation of thin films or magnetic waveguides [111, 112]. Similarly to  $k$ -resolved BLS, it can be also used for material or waveguide characterization [41, 111]. The advantage of the phase-resolved BLS over  $k$ -resolved is better spatial resolution, on the other hand the thermal excitation cannot be measured by phase-resolved BLS.

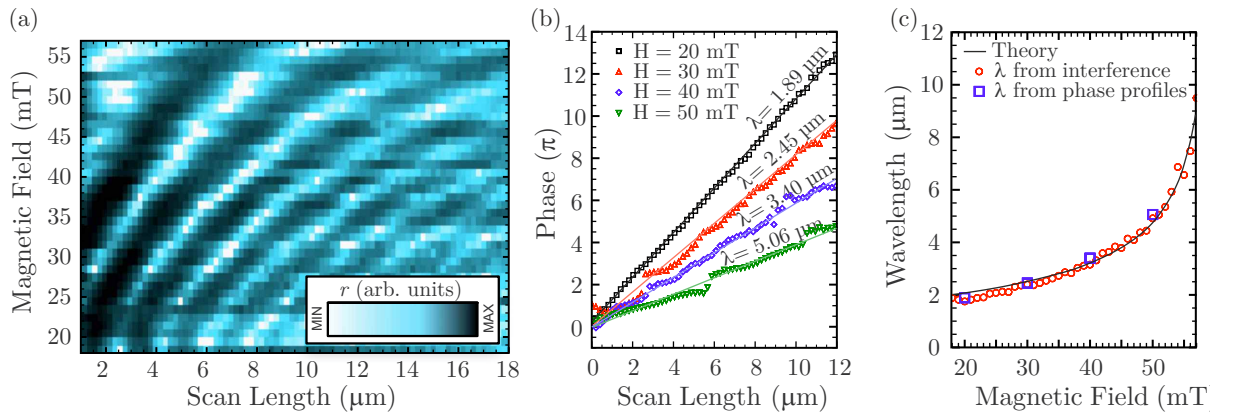


**Figure 2.17:** (a) Measured interference signal ( $R$ ) with respect to scan length and external magnetic field for permalloy stripe  $2.5 \times 100 \mu\text{m}^2$  and with nominal thickness of 40 nm. The black (white) regions represent positions of constructive (destructive) interference. (b) The full reconstruction of spin wave phase in selected fields. The calculated wavelengths from panel (a) and (b). Taken from [111].

## Material characterization

The material characterization is usually done by measuring only the interference pattern in dependence of the external magnetic field and determining the wavelength by fitting the equation 2.22. This map, where one axis is the spatial dimension along the propagation axis and the second is the external magnetic field is shown in Figure 2.17 (a). To compare approaches of full phase reconstruction and fitting of the equation 2.22, the phase evolutions for fields 20, 30, 40 and 50 mT were measured and are shown in the Figure 2.17 (b). According to equation 2.21, the wavelengths of spin waves were extracted. Figure 2.17 (c) shows extracted wavelengths from the fit, calculated dispersion relation, and four measured data points with employing the full phase reconstruction. These two approaches are in good agreement with respect to each other and the theory. Since the interference measurement is four times faster than the full phase reconstruction, it is usually used for material characterization in samples with sufficient signal.

The dependence of the wavelength to the external field with fixed frequency is measured instead of the dependence of the wavelength (wavenumber) to frequency (dispersion relation), because usually, EOMs suffer from a strong dependency of the signal strength on driving frequency. The signal could change even so much, that it could be dangerous for the single-photon detector, which makes automatized measurements impossible.

## Phase of excited spin waves

The phase-resolved BLS is also used to study microwave excitation from either an antenna or a coplanar waveguide. In the study done by Fallarino [113], the non-reciprocity in spin-wave amplitude for Damon-Eshbach geometry and coplanar waveguide was analyzed. One direction of spin waves is remarkably higher in amplitude, as shown in Figure 2.18 (a) black curve. This direction depends on the direction of static magnetization (which is usually steered by the external magnetic field). This behavior is present because of the near-

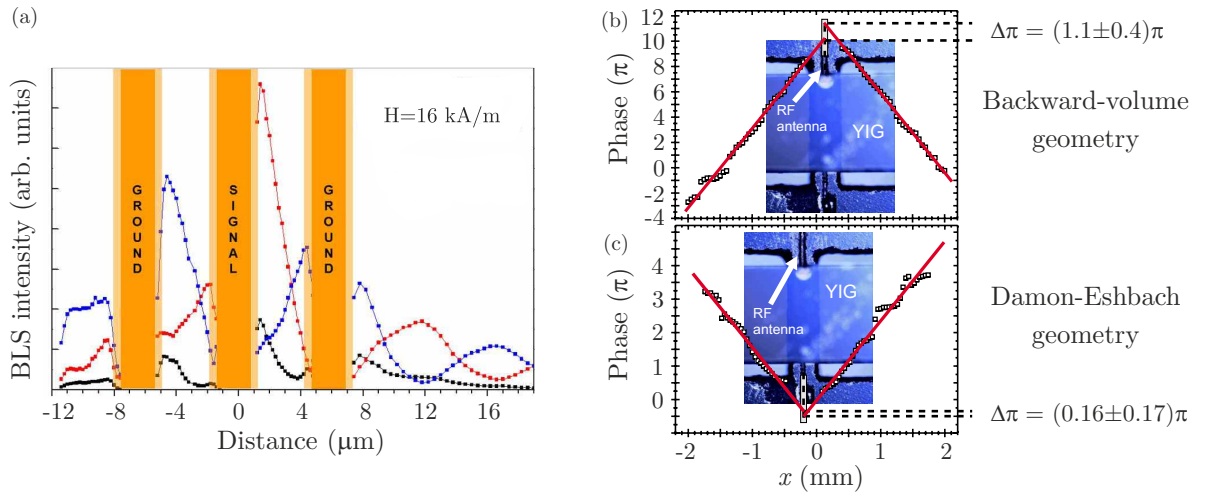


**Figure 2.18:** (a) The measured phase-resolved BLS signals. The black curve is pure spin-wave signal ( $R$ ), red (black) curve is interference (with  $\pi$  shift) signal  $r_0$  ( $r_{\frac{\pi}{2}}$ ). Note the non-reciprocity depending on the direction of emitted spin waves from coplanar waveguide. Taken from [113]. (b)-(c) The difference in spin-wave phase emitted from microstrip antenna for both, backward volume (b) and Damon-Eshbach (c) geometry. Taken from [109].

field effects of the excitation field on spin-wave precession, which results in a constructive (destructive) interference. This can be concluded from the interference signals [blue and red curves in Figure 2.18 (a)].

Another interesting non-reciprocity arises for backward volume spin waves excited by a microstrip antenna [109]. The phase shift of  $\pi$  is present between the counter-propagating excited spin waves, as can be seen in negative  $k$  in Figure 2.18 (b). On the other hand, the spin waves in Damon-Eshbach geometry, which are non-reciprocal in amplitude distribution along with film thickness, do not exhibit this shift and the measured difference in phase for both directions of propagation is within the measurement error as is shown in positive  $k$  in Figure 2.18 (b).

## 2.7. Time-resolved BLS

From the nature of Brillouin scattering, the BLS works in the frequency domain (Fourier transformation of the time-domain), so there is no need in achieving temporal resolution in the order of precession periods of magnetization (ps  $\rightarrow$  ns). But the evolution of spin waves in the order of 1 ns  $\rightarrow$   $\mu$ s can be captured with the use of time tagging technique.

The spin waves are usually excited by an electrical pump pulse to a microstrip antenna or a coplanar waveguide. This pulse is also used for setting the time  $t_0$  (start of the pulse) in the time-of-flight acquisition card. This card is also synchronized with the scanning of TFPi, so the frequency information can be recorded as well. It means that for every detected photon on the detector, the spatial position, the time difference to  $t_0$ , and the frequency of the photon can be saved.

Due to a rather low scattering cross-section of the BLS process, thousands of pulses are usually measured. This implies that all processes have to be stochastic and repeatable. This is ensured by a sufficient delay between the individual pulses.

### 2.7.1. Application of time-resolved $\mu$ BLS

The time-resolved BLS technique has the main usage in the study of non-linear processes or Bose-Einstein condensation. Also, the group velocity of spin-wave packets can be measured.

#### Group velocity

The time-resolved BLS technique can be used for the measurement of the group velocity of spin waves [114, 115]. This is achieved by measuring the arrival time of a spin-wave packet at a certain distance from the antenna. The group velocity is then

$$v_g = \frac{x}{\tau}, \quad (2.25)$$

where  $x$  is the distance from the antenna, and  $\tau$  is the time delay from the pulse.

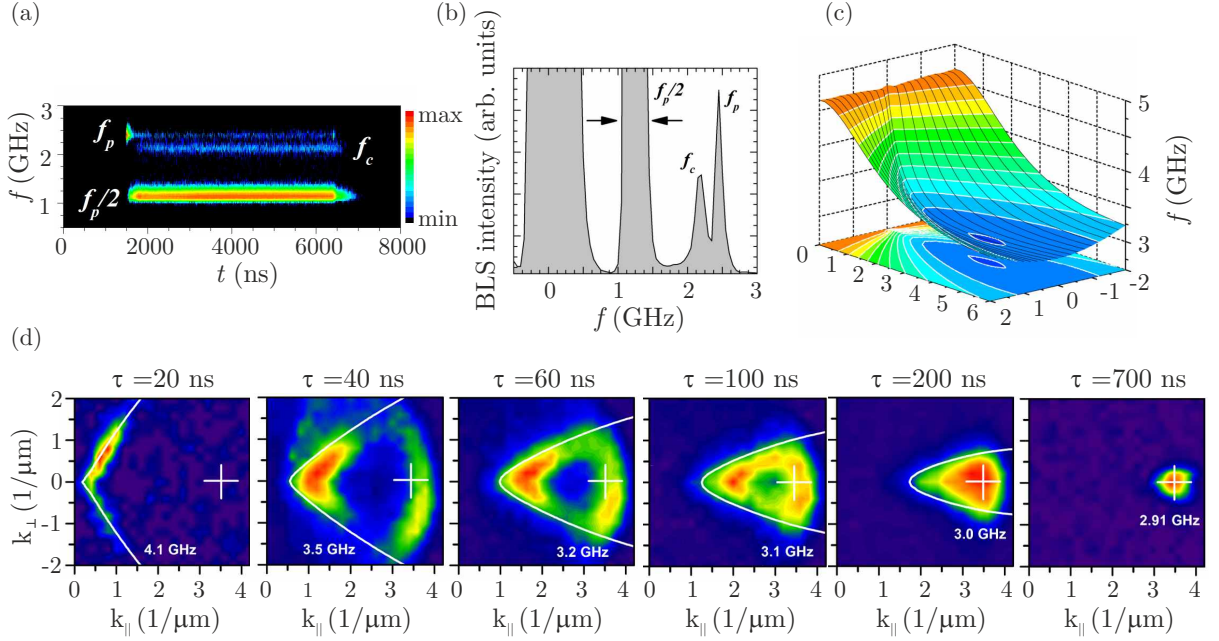


**Figure 2.19:** (a), (b) Time-resolved (a) and time-integrated (b) BLS measurement on the non-linear processes in YIG film with thickness of 2.2 mm. The lowering of the signal strength at  $f_p$  after 30 ns is visible. Also, in time-integrated signal the  $\frac{f_p}{2}$  is stronger than  $f_p$ . Taken from [118]. (c) Dispersion relation of YIG thin film with thickness 5.1  $\mu\text{m}$ . The global minimum occurs at 2.91 GHz. (d) Time-resolved BLS measurement of wavevector distribution during Bose-Einstein condensation. The white lines represent  $k$ -vectors with the same frequency. In the  $\tau = 700$  ns all magnons are condensed to the global energy minimum. Taken from [121].

### Non-linear processes

Another use of time-resolved BLS is in studies of non-linear magnon processes [116, 117]. In the study done by Liu, the three magnon process in YIG was investigated [118]. A current pulse with the duration of 5  $\mu\text{s}$ , the repetition rate of 5 kHz and the power of 575 mW was applied<sup>2</sup>. In the first 30 ns of the pulse the highest BLS signal was recorded for the pumping frequency, as can be seen in Figure 2.19 (a). This is due to the leading edge of the pulse. Not enough power is delivered to the system and spin waves are in the linear regime. After this 30 ns of the pulse, the non-linear processes dominate, and the peak is visible at half of the pumping frequency  $\frac{f_p}{2}$ . When the trailing edge of the pulse starts, there is again not enough power to be above the non-linear threshold and the majority of the signal comes again from spin waves at the pumping frequency. Time-integrated spectra further prove these findings, as is visible in Figure 2.19 (b). The frequency  $f_c$  results from the combination of two  $f_{p/2}$  magnons.

### Bose-Einstein condensation

The formation of Bose-Einstein condensate in magnon gas can also be investigated with the time-resolved BLS [119–121]. In Figure 2.19 (c), the dispersion relation for in-plane spin waves in YIG is shown. The global energy minimum is apparent at 2.91 GHz, in the so-called backward volume geometry. Due to the existence of the global energy minimum,

<sup>2</sup>which is above non-linear threshold ( $\sim 200$  mW)

the chemical potential is introduced to the system, which limits the number of magnons (quasi-particles). If the system is then overpopulated, the Bose-Einstein condensation occurs, and the confined peak at 2.91 GHz is formed as can be seen in Figure 2.19 (d). During the Bose-Einstein condensation, the number of particles in the system has to be conserved, so only four magnon scattering processes can occur. Another condition is, that the relaxation time of the spin precession has to be large enough.

# 3. Construction and characterization of the phase-resolved BLS setup

This chapter discusses the design, construction, and characterization of the phase-resolved BLS setup. The setup is based on the design of the intensity-resolved BLS setup built-in 2018-19 by Lukáš Flajšman [122]. The first part of the chapter shows the design of the setup, while the second section deals with the characterization of the individual parts and performance of the whole setup.

## 3.1. General overview

The overall schematic is shown in Figure 3.1 (a). The setup is designed in a way that it can use two lasers, which can be easily interchanged. Both lasers are shown in side-view in Figure 3.1 (c). This allows us to continue measuring, even if one of the lasers needs maintenance. The first optical component which light passes is Faraday isolator. Then, the light is guided to Fabry-Perot (FP) etalon. The 10% of the light is then split and steered towards the interferometer and used for stabilization. The rest of the light (90%) goes through the half-wave plate and polarizer. The beam is expanded with the use of two lenses. The electro-optical modulator (EOM) is placed in the focal point of this beam expander.

To achieve sub-micrometer spatial resolution, we used a commercially available scanning microscope. The laser light is routed to objective and back-scattered light is decoupled from the microscopic module. Before entering the interferometer, the polarization of the light can be adjusted with another half-wave plate. In order to spatially filter the light before passing through interferometer mirrors, we use the lens in a 3D positionable lens holder and a changeable aperture.

The interferometer was purchased from Table Stable ltd. After passing both interferometers, the light is led to a single-photon counter.

## 3.2. Light source

The first laser is Laser Quantum Torus, and the second one is Cobolt Samba. There are several requirements for the laser, which have to be fulfilled. The laser must have a single-mode operation, which means that the higher laser modes are suppressed. These modes are usually equidistantly distributed around the main mode in the span of several gigahertz. This range is of the main interest in the typical BLS measurement, so the undisturbed spectrum is necessary. The Torus laser suppresses these peaks by a factor of four, when compared to Samba laser.

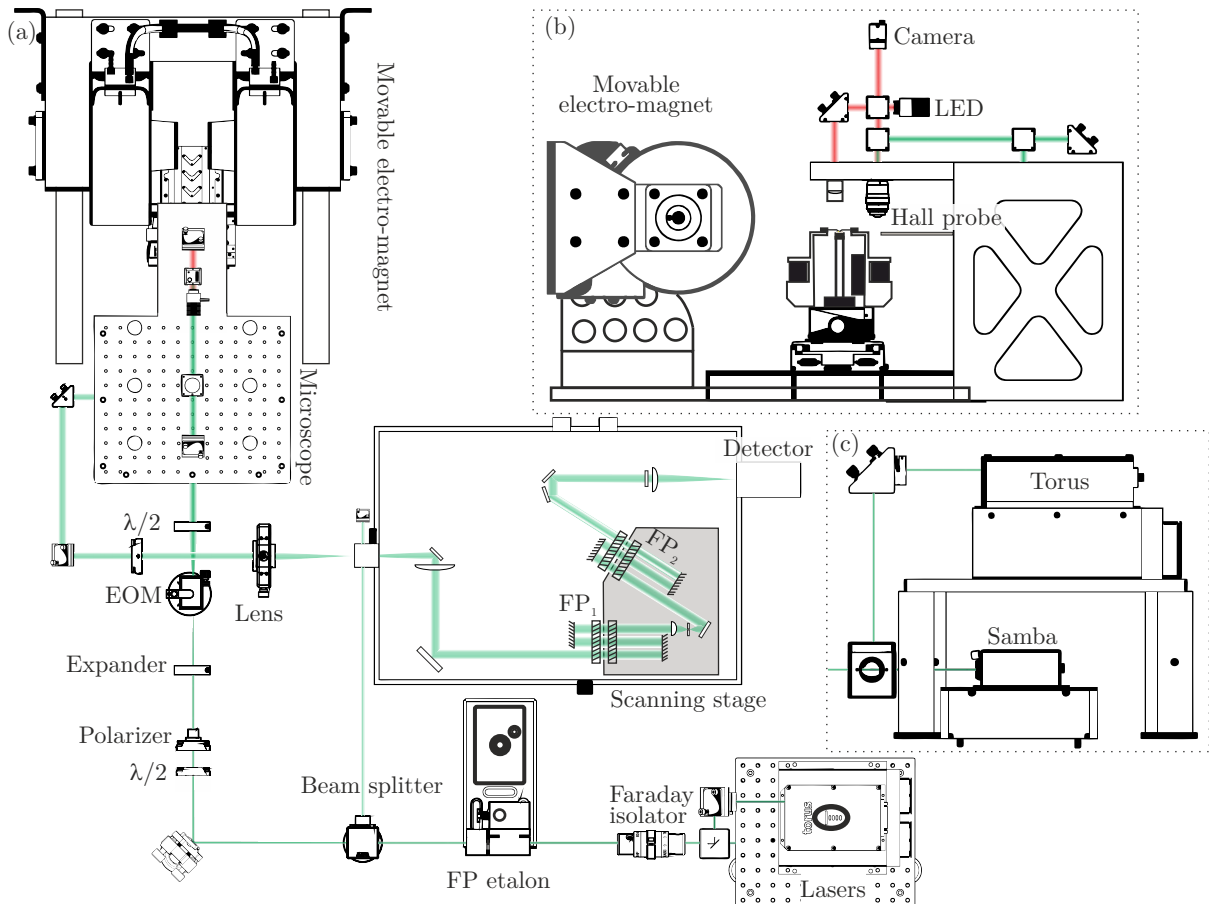


**Figure 3.1:** (a) Schematic of the used BLS setup. (b) Side-view of the microscope module and electro-magnet. (c) The side-view of the two used lasers.

To be able to measure the BLS spectra, sufficient laser power is needed. The Torus laser is specified to 250 mW, while Cobolt Samba is specified to 300 mW.

During the long-term measurement, the stability of the laser is crucial. We measured the stability of both lasers over the span of two hours. The measured data is shown in Figure 3.2 (a). Both lasers oscillate within 1.5 %.

### 3.2.1. Faraday isolator

The feedback loop of the laser can be compromised by the back-reflected light. To prevent the back-reflected light from entering the laser aperture, a Faraday isolator is placed right after the laser source.

The Faraday isolator consists of two polarizers, glass, and a permanent magnet. After passing the first polarizer, the polarization axis is rotated. The polarization axis of the second polarizer is then adjusted to be the same as the new polarization axis of the light. If the light enters the Faraday isolator from the other side, the sense of rotation is opposite, thus majority of intensity cannot pass. The attenuation is around 40 dB. Faraday isolator also decreases the primary laser intensity. In our setup, we lost approximately 7 % of the light intensity after the transmission through the Faraday isolator.

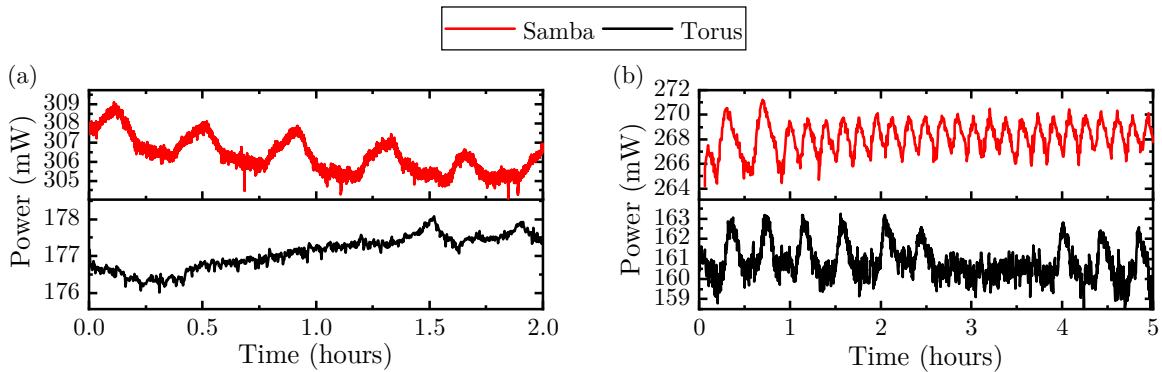


**Figure 3.2:** The stability of the light intensity of Cobolt Samba (red curves) and Torus (black curve) (a) after laser and (b) after Fabry-Perot etalon.

### 3.2.2. Fabry-Perot etalon

To further suppress the unwanted laser modes, we added a Fabry-Perot etalon to our setup. We use the solution developed by Table Stable ltd. The primary laser beam loses around 8% of the intensity upon transmission through the etalon. The stable state of the active stabilization is reached approximately after two hours of operation. We measured the stability of the etalon as the intensity fluctuation over the time span of 5 hours. The data were already acquired in the stable state of etalon active stabilization. The measured data are shown in Figure 3.2 (b). For both lasers, the fluctuations caused by the FP etalon are below 2%.

In the case of Cobolt Samba, the laser modes are suppressed by a factor of 55. The Torus has weaker laser modes than Cobolt Samba, so after the filtration in FP etalon, they are already in the order of the background noise.

### 3.2.3. Adjusting of incident laser intensity

The polarizer and a half-wave plate are used to change the incident light intensity on the sample. The polarizer is in a fixed holder, so the polarization axis is not changed between measurements. The change of the incident intensity is done by rotating the half-

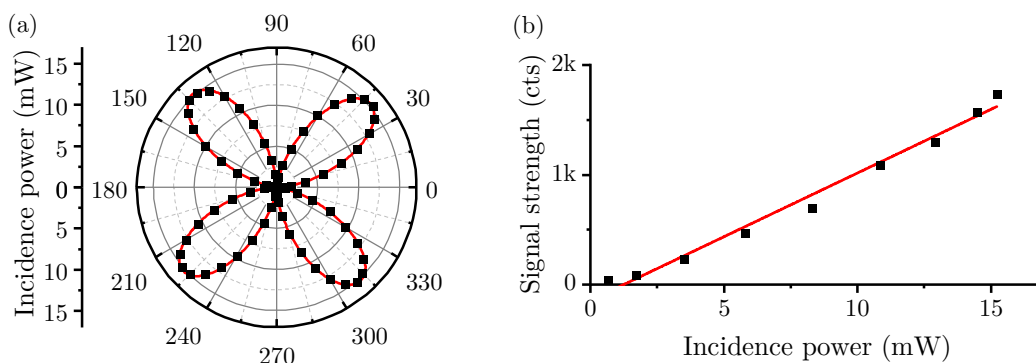


**Figure 3.3:** (a) The incident intensity versus the half-wave plate angle. The measured data (squares) were fitted with the  $\sin^2$  (red line). (b) signal strength in dependence on the incident intensity. The measured data (squares) were fitted with a linear function (red line).

wave plate, which is mounted on a motorized rotational holder. The dependence of the incident intensity of the Torus Laser on the angle of the half-wave plate ( $\kappa$ ) is shown in Figure 3.3 (a). The measured data ( $I$ ) was fitted with function

$$I = I_{\max} \sin(2\kappa), \quad (3.1)$$

where  $I_{\max}$  is maximal intensity. The fit reveals that the maximal possible incident intensity is  $I_{\max} = 15.21 \pm 0.05 \text{ mW}^1$ .

We measured the dependency of the signal strength on the incident intensity. The results are shown in Figure 3.3 (b). The measured data are fitted with the linear function, as is predicted by the equations 2.9 and 2.10. But this linear behavior will only hold to certain light intensity. After passing the threshold intensity, another effects can arise, such as a reduction in saturation magnetization or burning of the sample. This threshold intensity can vary a lot for different samples, for example, in thinner samples can be much lower.

### 3.3. Electro-optic modulator

To perform the phase-resolved measurement, the modulation of the phase of the light is essential. The electric schematic is shown in Figure 3.4 (a). As a signal generator, we use R&S SMB100A, which allows frequencies in the range of 100 kHz – 40 GHz. Then the signal is split in 3 dB power divider (P214H). To allow easy switching between different measurements, the RF-switches (CCR-33S8E-T) are in both branches. One branch is connected to the probe, which can be contacted to the excitation antenna.

The optional bias-tee can be added between the RF switch and the excitation antenna. The direct current (DC) from the antenna is put into the ohmmeter. The resistivity of measurement can then be used for checking if the contacting was successful. But in our setup, the probability of burning antennas was dramatically increased with mounted bias-tee, thus in the current version, this element is omitted.

The signal in the second branch passes through the attenuator (AV884H-10), the phase shifter (P1507-28), and the electro-optic modulator (QUBIG TW-15M1-VIS). The measured strength of the modulated signal versus the driving frequency is plotted in Figure 3.4 (b). We can see that the signal exhibits a strong maximum between the 2

<sup>1</sup>The light passes through several mirrors and and two 50:50 beam splitters.

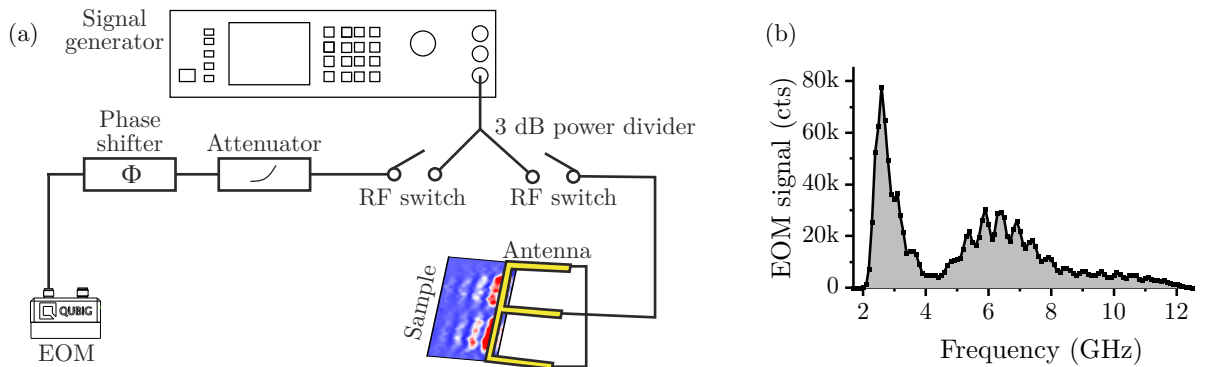


**Figure 3.4:** (a) The schematic of the RF signal in phase-resolved BLS. (b) The spectra of EOM obtained for different driving frequency.

and 4 GHz. This non-constant behavior can be compensated by the aforementioned RF attenuator.

To guide the light with minimal losses through the EOM, it is essential to focus the light into the input aperture. This is done by placing the EOM to the focal point of the beam expander and by careful positioning. The resulting power loss is around 1 %.

### 3.4. Microscope module

The microscope module was purchased from THATec Innovation gmbh. This scanning optical microscope also allows for easy sample contacting with the integrated micro-positionable probe station. The contacting is done in the so-called contacting position, where the microscope with lower magnification is used. The sample stage with contacted probes then can be moved under the high-resolution objective lens (LD EC Epiplan-Neofluar 100x/0.75 BD). Both optical systems use the same illumination and camera. The picture of the excitation antenna on the permalloy thin film obtained in the measurement position (with high-resolution objective lens) is shown in Figure 3.5 (a).

Used objective lens allows measurements with the spatial resolution below 300 nm. We characterized the width of the beam with a knife-edge technique. We scanned over the edge of the permalloy waveguide with the width of 4  $\mu\text{m}$  and the thickness of 20 nm in the field of 20 mT. The spatial step was 100 nm. The obtained data with fitted error function are shown in Figure 3.5 (b). The Gaussian beam width was fitted as  $w_{\text{Gauss}} = 270 \pm 30$  nm.

#### 3.4.1. Electromagnet

Usually, the spin-wave BLS experiments require an external magnetic field. In our setup, we use an electromagnet, which is mounted on the rails to allow moving of the sample stage between the contacting and the measurement positions without hitting the objective lens.

In some spin-wave experiments, such as measuring of the DMI constant, or Bose-Einstein condensation, the exact knowledge of the external magnetic field is essential. In order to characterize the field of the used magnet, we scanned with three dimensional Hall probe across the gap, while the current was set to the maximum value of 18 A. This

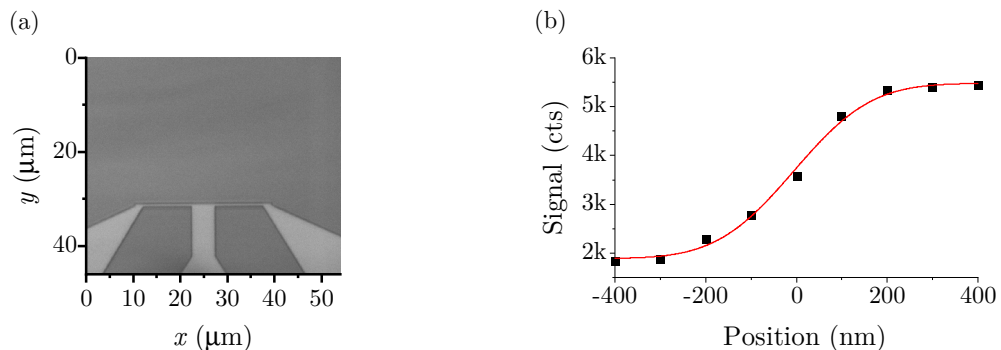


**Figure 3.5:** (a) The image taken from the microscope. This antenna was used in section 3.6. (b) The signal strength acquired while scanning over the edge of a permalloy stripe. The measured data (squares) are fitted with an error function (red line).

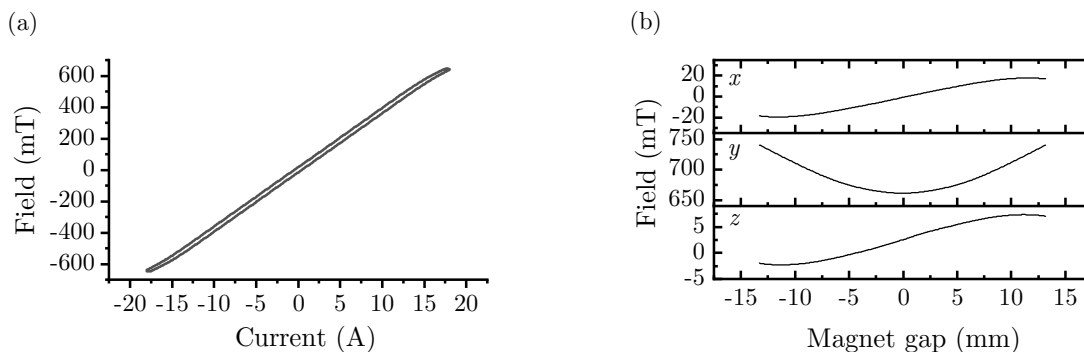


**Figure 3.6:** (a) The hysteresis loop measured in the sample position. (b) The evolution of the three components of the magnetic along the gap of the electromagnet.

measurement is shown in Figure 3.6 (c). The field in  $y$ -direction varies by approximately 10 %. The other components of the field are below 0.4 % in the center of the gap.

We measured two hysteresis loops, one at the sample position (center of the gap) and one at the usual position of the probe. The hysteresis loop at the position of the sample is shown in Figure 3.6 (b). The maximum field at the sample position is approximately 670 mT. This field is sufficient for the majority of a spin-wave experiments.

During the optical measurement in the BLS, the Hall probe needs to be slightly off-centered. It was verified that the magnetic field measured at the sample position is proportional to the magnetic field at the permanent probe position with a multiplication factor of 0.96. This value was found by dividing the slopes of hysteresis loops in both positions.

### 3.5. Tandem-Fabry-Perot interferometer

As the interferometer, we use TFP-2 HC from Table Stable ltd. The acquisition of the signal is done by the single-photon counter Hamamatsu C11202-050. The mirrors in the TFPi are coated with anti-reflexive layers tuned to 532 nm wavelength of the light. To ensure the mechanical stability, the whole interferometer is placed on the active vibration isolator.

We determined the stability of the alignment of the TFPi by measuring the strength of the reference signal. In this signal, the oscillation of the laser and FP etalon is also included. These oscillations are low in comparison to the oscillations of the TFPi itself, so the resulting signal is mainly affected by the drift of both mirrors. The strength of the reference signal over span of 12 hours is plotted in Figure 3.7 (a). On the right axis are voltages of all six stabilizing piezo actuators. There are two types of oscillations. The first type has period around half of an hour, and the relative change around 10 %. This fluctuation is caused by the active stabilization of the mirrors. The second fluctuation is caused by the gradual misalignment of the whole interferometer. This fluctuation can be optimized by the properly chosen dither parameter.

The dither parameter determines the change in the voltage of piezo actuators in individual steps during the stabilization. We investigated the dependence of the relative change in the reference signal on the dither parameter. With each dither value, we measured over the span of 12 hours. The result is shown in Figure 3.7 (b). If the dither parameter is too low, the changes of the signal are below the noise level, thus the alignment is gradually

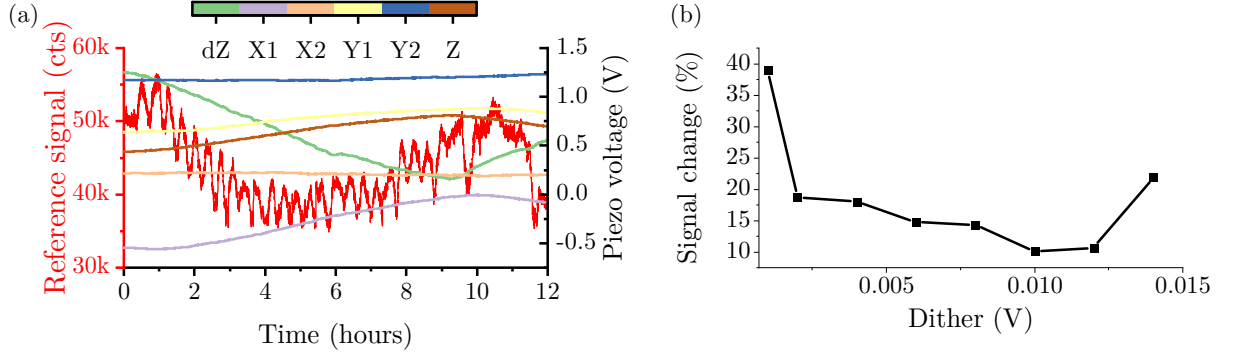


**Figure 3.7:** (a) The stability of TFPi over the span of 12 hours. The red curve (left axis) shows the strength of the reference signal. The right axis shows the voltage on the piezo actuators. X1 (X2) and Y1 (Y2) are the piezo compensating tilt of the first (second) interferometer, dZ piezo compensate for the relative change in cavity length and Z piezo compensates the shift from central frequency. (b) The relative change in reference signal strength versus dither parameter. The reference signal was measured for each point for 12 hours.

lost. On the other hand, if the dither parameter is too high, the alignment is crudely changed during each step of stabilization. Based on these findings, we decided to use the dither parameter 0.01 V for further measurements as it provides the most stable active stabilization of TFPi.

### 3.6. Verification of the setup

The setup was verified with the measurement of a well-known system. For this purpose, we decided to use a thin permalloy layer with lithographically prepared antennas for the excitation of spin waves. The width of the microstrip part of the antenna is 500 nm. This width allows to excite spin waves with  $k$ -vector from 0 to approximately 12 rad/ $\mu\text{m}$ . The thickness of the permalloy layer is 40 nm. The calculated dispersion relations of the sample for the first two thickness modes are shown in Figure 3.8 (a). The measurement of the thermally excited spin waves reveals both of these modes, as can be seen in Figure 3.8 (b).

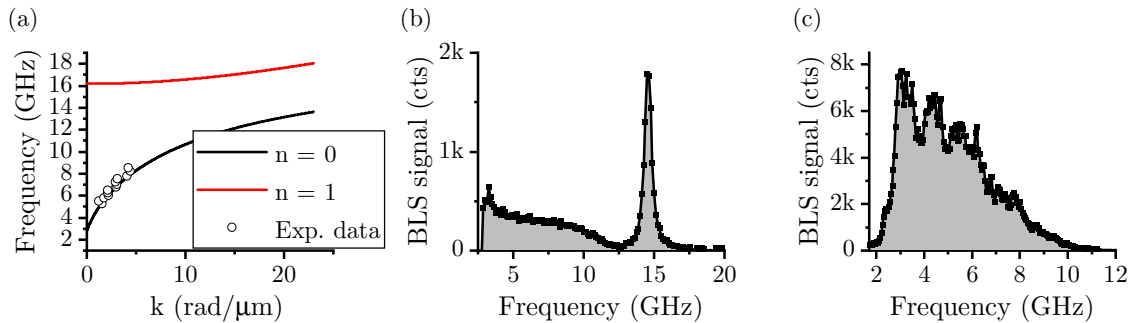


**Figure 3.8:** All panels assumes external field of 10 mT. (a) The calculated dispersion relation for studied 40 nm permalloy film. (b) The thermally excited spin waves. (c) RF sweep approximately 2  $\mu\text{m}$  away from the antenna.

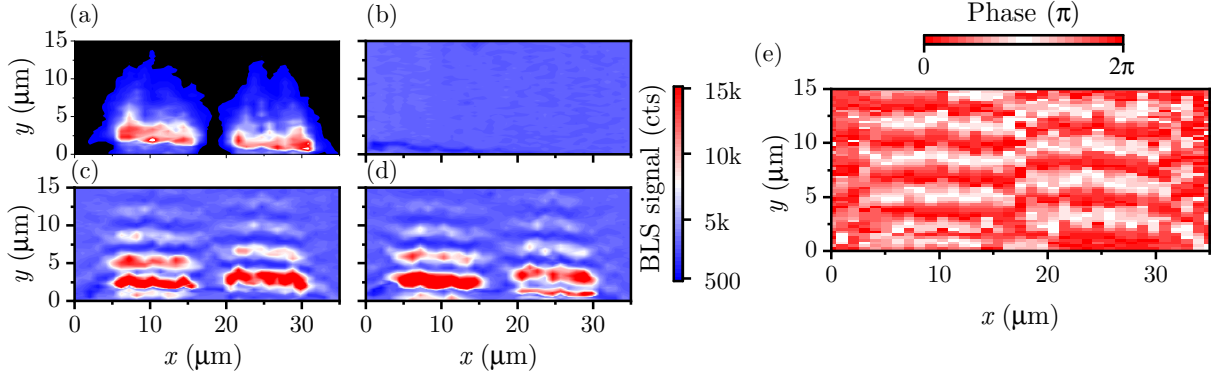


**Figure 3.9:** (a) - (d) The four BLS measurements needed for full phase reconstruction. (a) The intensity measurement. There is no electrically modulated part of the light. (b) Only electrically modulated light. There is no current in antenna. The interference between spin waves and EOM signal for two phases shifted by  $\pi/2$ . (d) Reconstructed phase from measurements (a)-(d).

To see the response of the system, we measured RF spectra, where spin waves were excited by microwave antenna. The laser spot was placed approximately  $2\ \mu\text{m}$  away from the antenna. Results are shown in Figure 3.8 (c). For the phase-resolved measurement, we chose 6 GHz, as it provided sufficient signal and the spin-wave wavelengths at this frequency are in the order of micrometers.

To reconstruct the full phase of spin waves, four measurements are needed, as was discussed in section 2.6. These four measurements are shown in Figure (a)-(d). From the intensity measurement [Figure 3.9 (a)], we can see that spin waves are excited only in the microstrip part of the antenna. The EOM signal is proportional to the reflectivity of the sample, which is constant for the thin film, as can be seen in Figure 3.9 (b). The two interference patterns [Figure 3.9 (c) and (d)] are phase-shifted by  $\pi/2$ , as is expected. The not-distorted phase fronts are apparent. We can observe a decrease of the signal in the vicinity of the antenna due to the scattering from the edges.

The reconstructed phase shows the phase shift between the two parts of the excitation antenna. This is caused by the opposite current flow in the antenna. The linear increase in the direction from the antenna is present after two micrometers. In this region, non-linear phenomena are present, which distorts the phase. From this slope we found the  $k$ -vector as  $k = 1.96 \pm 0.02 \frac{\text{rad}}{\mu\text{m}}$ , which is in agreement with the calculated dispersion relation.

# 4. Propagation of spin waves through Néel domain wall

The propagation of spin waves through domain walls (DW) is of high interest. Recently, it has been shown that domain walls can serve as a spin-wave valve depending on its magnetic state (head-to-head and tail-to-tail spin configurations) [123]. In samples with perpendicular magnetic anisotropy, it was demonstrated that domain walls could affect both spin-wave amplitude and phase and that spin waves can move the domain wall by spin torque phenomena [124–127]. Moreover, domain walls may also serve as a source and probe of spin waves with short wavelengths [128] or can be used as magnonic conduits by themselves [100, 129]. However, no experimental study was conducted to reveal the spatial evolution of spin waves transmitted through a domain wall in a magnonic waveguide. A thorough understanding of the behavior of spin waves in magnonic waveguides hosting domain walls is necessary for designing future integrated magnonic circuits as they present the most elementary building block of magnonic circuitry.

This chapter elaborates on the propagation of spin waves through the Néel type domain wall in a magnetic waveguide written in a metastable paramagnetic iron matrix. The static magnetic configuration is revealed with the use of micromagnetic modeling and confirmed experimentally by magnetic force microscopy (MFM) measurements. The dynamic properties of spin-wave propagation are investigated by means of  $\mu$ -BLS measurements, and further insight is provided via dynamic micromagnetic simulations.

## 4.1. Sample preparation

To prepare a sample suitable for this study, we used a metastable fcc  $\text{Fe}_{78}\text{Ni}_{22}$  thin film with a nominal thickness of 16 nm. The films were grown on a Cu(001) single crystal substrate under ultra-high vacuum conditions by the evaporation from  $\text{Fe}_{78}\text{Ni}_{22}$  rod (2 mm thick, purity 99.99%, heated by electron bombardment) at a residual CO pressure of  $5 \times 10^{-10}$  mbar [44]. After deposition, the sample was transferred to the scanning electron microscope for focused ion beam irradiation. We oriented the long axis of the waveguides along the fcc[010] direction of the Cu substrate in order to obtain the highest possible magnetocrystalline anisotropy [43]. To imprint the anisotropy direction perpendicularly to the long axis of the waveguide, we wrote the structures with a single pass of a 30 keV  $\text{Ga}^+$  ion beam (30 nm spot, beam current of 150 pA and 5  $\mu\text{s}$  dwell time) with the fast scanning direction rotated by  $80^\circ$  from the waveguide's long axis. The resulting ion dose of  $4 \times 10^{15} \text{ cm}^{-2}$  has given reliable growth conditions for all the waveguides. The dimensions of the waveguides were  $3 \times 20 \mu\text{m}^2$

For the excitation of spin waves, a stripline antenna was placed on top of the waveguide [see Figure 4.1 (a)]. The 1  $\mu\text{m}$  wide antenna, made of a multilayer structure consisting of

a 20 nm  $\text{SiO}_2$  insulating layer, 5 nm Ti, 85 nm Cu and a 10 nm Au capping layer was patterned by electron beam lithography using PMMA resist, followed by e-beam evaporation of the layers and subsequent lift-off process.

## 4.2. Static characterization

To be able to measure the spin-wave propagation through the domain wall, there has to be sufficiently long propagation length and the possibility to stabilize the domain wall. The propagation lengths of surface spin waves modes are usually one order of magnitude longer than for the backward-volume modes. So the Damon-Eshbach geometry is favorable. However, in zero magnetic field, the magnetization lies along the long edge of the waveguide in the aforementioned backward-volume geometry. For this reason, the uniaxial anisotropy with the in-plane easy-axis perpendicular to the long edge of the waveguide was imprinted by employing an appropriate focused ion beam scanning procedure [43].

The strength of this anisotropy was studied by means of Kerr microscopy. An effective anisotropy field of 40 mT was measured. The anisotropy field is called effective, as we see only the result of the two competing contributions – crystalline uniaxial magnetic anisotropy coming from the FIB writing process and from the uniaxial shape anisotropy having its origin in the shape of the waveguide (approx. 7 mT for the 1.5  $\mu\text{m}$  wide waveguide) [130]. The total magneto-crystalline anisotropy strength is then obtained as the difference of the two contributions.

### 4.2.1. Stabilization of the domain wall

The desired two-domain state of the waveguide was stabilized by applying an external magnetic field in  $+y$  direction while observing the magnetization by a Kerr microscope (evico magnetics GmbH). The position of the domain wall was stable in zero external magnetic field. To measure the depinning field, we slowly increased the external magnetic

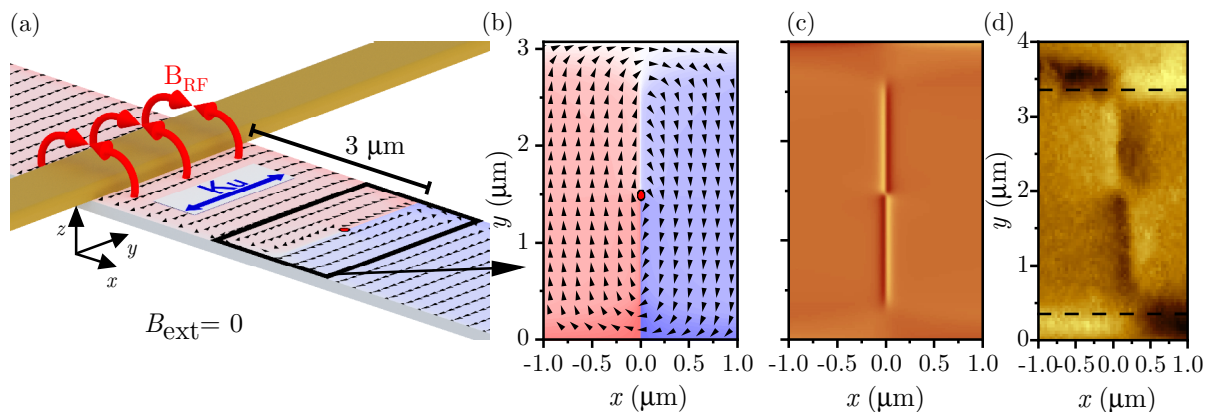


**Figure 4.1:** (a) Scheme of the experimental geometry. The other wire represents the excitation antenna producing the RF magnetic field. The uniaxial anisotropy (easy axis) created by the FIB irradiation is shown as a blue double arrow. The domain wall is positioned  $3 \mu\text{m}$  from the edge of the antenna. (b) Micromagnetic simulation of the domain wall state. (c) The computed MFM image from the micromagnetic simulation. (d) Magnetic force microscopy image of the domain wall.

field until the domain wall moved. This procedure was repeated multiple times, and the depinning field was measured as  $1.0 \pm 0.1$  mT.

### 4.2.2. Characterization of the type of the domain wall

To further reveal the internal structure of the domain wall, we performed MFM and micromagnetic simulations.

The MFM measurements were conducted in the Bruker Dimension Icon with the ASYMFMLM probe tip<sup>1</sup>. To avoid dragging the domain wall during the measurement, the scanning direction was perpendicular to the long axis of the waveguide. The resulting image is shown in Figure 4.1 (d). The change of the contrast on the borders of the waveguide confirms that the magnetization is pointing antiparallel on both sides of the domain wall. The pattern along the domain wall indicates a more complex structure of the magnetization.

This was further investigated by means of micromagnetic simulations, which were performed using the MuMax3 software [131] and the following parameters: simulation area  $3 \times 16 \mu\text{m}^2$ , cell size  $4 \times 4 \times 16 \text{ nm}^3$ ,  $M_s = 1409 \text{ kA/m}$ ,  $K_u = 28.9 \text{ kJ/m}^3$ ,  $A_{\text{ex}} = 11 \text{ pJ/m}$ . These material parameters were obtained from fitting the spin-wave dispersion measured by phase-resolved BLS and will be discussed later in this chapter. We also confirmed that the simulation with a twice smaller cell size gives an identical result.

The simulated MFM image is shown in Figure 4.1 (c). The simulated and measured MFM images are in good qualitative agreement. From the simulated spatial distribution of magnetization, which is shown in Figure 4.1 (b), it is apparent that the domain wall is a symmetric Néel wall with a circular Bloch line (vortex) in the middle [132, 133]. The Bloch line is enforced by the surrounding topology (antiparallel magnetization along the two edges). The occurrence of the Bloch line results in a better dipolar energy minimization between the charges of the wall and those on the sides of the strip.

## 4.3. Dynamic characterization

After the static characterization, we investigate the dynamic properties of spin waves. This was done employing the intensity and the phase-resolved  $\mu$ -BLS. The first subsection deals with the thermal excitations of spin waves, while the second section study the coherently excited spin waves.

### 4.3.1. Thermally excited spin waves

In order to get a better insight into the internal magnetic field structure, we measured thermally excited spin waves while scanning the  $\mu$ BLS spot (300 nm in diameter) in the center of the waveguide, in the single domain state [Figure 4.2 (a)] and across the domain wall [Figure 4.2 (b)]. The total length of the linescan was  $1 \mu\text{m}$ , with a spatial step of 50 nm. We observed an increase of spin-wave frequencies by approximately 2 GHz in the domain wall region (the domain wall is located at  $x = 0 \mu\text{m}$ ) in comparison to the waveguide in the single-domain state. This increase can be attributed to approximately 15 mT increase in the local effective magnetic field. The effective magnetic field obtained from the micromagnetic simulations [Figure 4.2 (a), (b), red curve] is plotted together with

---

<sup>1</sup>Asylum MFM low moment

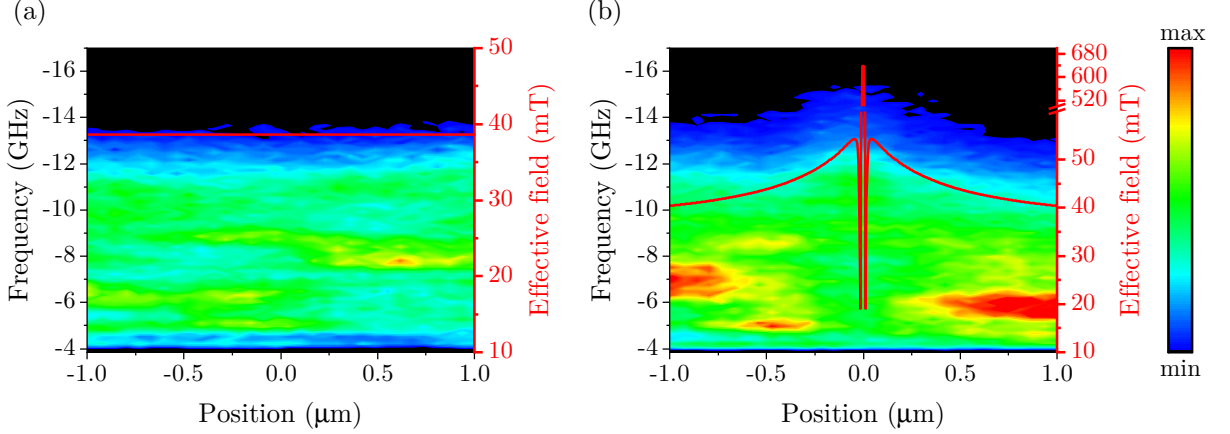


**Figure 4.2:** Plot of the BLS thermal spectra acquired while scanning the laser spot in the (a) single domain state or (b) across the domain wall (located at  $x = 0 \mu\text{m}$ ). The color code represents the spin-wave intensity, and the red curve (right axis) represents the magnitude of the local effective field. The negative frequencies stay for Stokes process.

the thermal spectra. Note, that at the exact position of the domain wall, the effective field exceeds 600 mT but this peak is spatially restricted only to a region of approximately 10 nm (an order of magnitude below the  $\mu\text{BLS}$  spatial resolution), and its contribution is not present in the acquired spectra.

### 4.3.2. Propagation of coherent spin waves

This section discusses the experiments with stimulated spin-wave excitation. The first part discusses the material characterization, the second part characterizes the frequency response of the studied system, and the third part investigates the spatial distribution of the spin-wave intensity. The last part examines the spin-wave phase.

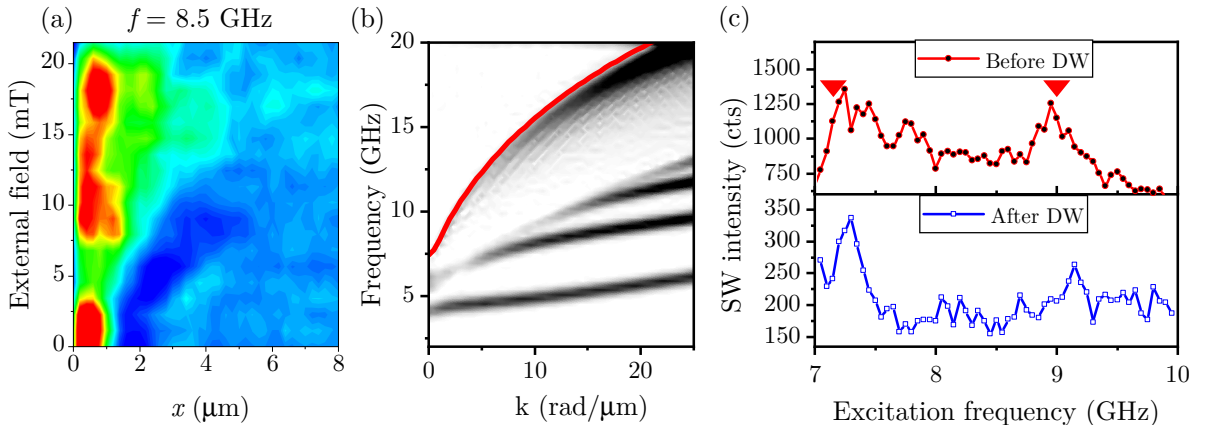


**Figure 4.3:** (a) The measured interference pattern for the excitation frequency of 8.5 GHz. (b) The dispersion relation obtained by means of micromagnetic simulation (color code) and analytical modeling (red curve). (c) Frequency sweeps for positions  $x = -0.5 \mu\text{m}$  (before the domain wall) and  $x = 0.5 \mu\text{m}$  (after the domain wall). The red arrows indicate prominent frequencies used in following experiments.

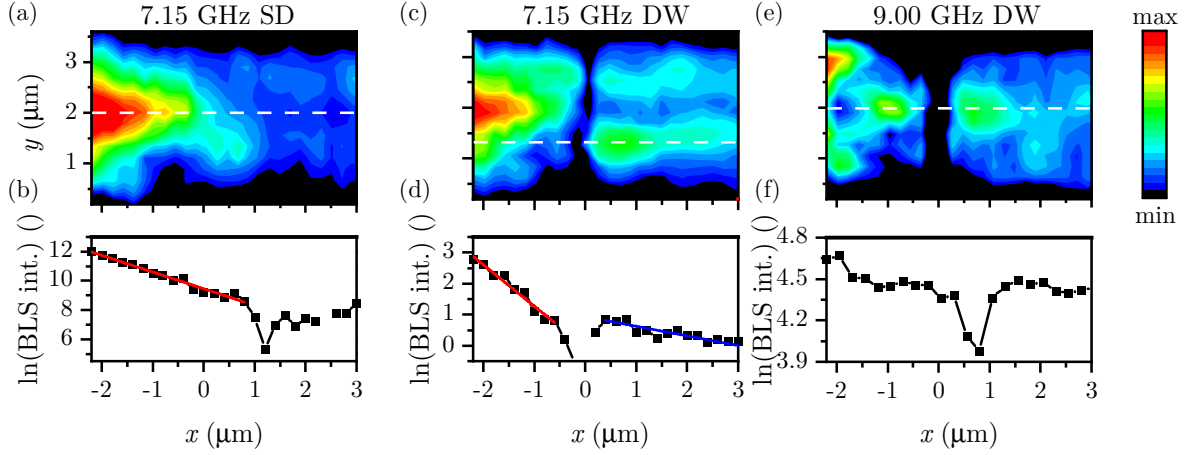


**Figure 4.4:** Spin-wave intensity maps for excitation frequency of 7.15 GHz (a) in single domain (SD) state and (c) in a two-domain state separated by the Néel domain wall (domain wall state) and (e) for excitation frequency of 9.00 GHz in domain wall state. The white dashed lines indicate the positions of the measured phase. (b), (e) The summed spin-wave intensity at the frequency of 7.15 GHz in (b) single domain state, and (e) domain wall state. The solid curves are linear fits of experimental data. (f) Summed spin-wave intensity for excitation frequency of 9.00 GHz in domain wall state.

### Dispersion measurement

To get the material parameters of the produced waveguides, we performed a phase-resolved measurement in order to obtain dispersion relation. This characterization was performed in a single domain state (without the domain wall). We measured field sweeps for three frequencies. The measured data for frequency 8.5 GHz is shown in Figure 4.3 (a). We obtained spin-wave  $k$ -vectors with the technique described in section 2.6. Then we fitted equation 1.17 and obtained following parameters:  $M_s = 1409 \text{ kA/m}$ ,  $K_u = 28.9 \text{ kJ/m}^3$ ,  $A_{\text{ex}} = 11 \text{ pJ/m}$ . The computed dispersion relation with obtained material parameters is shown in Figure 4.3 (b).

### Frequency sweep

To investigate the effect of the domain wall on the spin-wave propagation, it is essential to stabilize the domain wall in the vicinity of the source of coherent spin waves. In order to achieve this, the domain wall was positioned at a distance of approximately  $3 \mu\text{m}$  from the antenna.

In the following experiment, we excited spin waves by passing an RF signal (5 dBm, 7–10 GHz, frequency step 50 MHz) through the microwave antenna. The spin-wave intensity for each excitation frequency was acquired at two positions: the first position was  $x = -0.5 \mu\text{m}$  (before the domain wall), and the second position was  $x = 0.5 \mu\text{m}$  (after the domain wall). The resulting spectra are shown in Figure 4.3 (c). Based on these measurements, we selected two frequencies (7.15 GHz and 9.00 GHz, indicated by the red arrows), where we observed an increased spin-wave intensity at both positions, before and after the domain wall.

### Spatially-resolved BLS scans

For the selected frequencies, we performed intensity-resolved  $\mu$ BLS experiments. The measurements were done for the magnonic waveguide in a single domain state (SD), and in the domain wall (DW) state (here, domain wall state means two-domain state separated by the Néel domain wall). For the single domain state, we observe only the central waveguide mode, as is shown in Figure 4.4 (a). The summed intensity is shown in Figure 4.4 (b). The propagation length was extracted as  $1.8 \pm 0.2 \mu\text{m}$ .

The propagation of the spin waves excited at 7.15 GHz through the domain wall is shown in Figure 4.4 (c). The spin-wave propagation pattern before the domain wall resembles closely the one seen in Figure 4.4 (a). After passing the domain wall, the spin waves are split into two beams. A similar effect of splitting into two beams was observed in a different system by Demidov [93, 95]. The corresponding summed intensity is shown in Figure 4.4 (d). The change in the slope is apparent after the spin-wave passes the domain wall. The propagation length of the spin waves before the domain wall is  $1.4 \pm 0.2 \mu\text{m}$ , and after the domain wall  $7 \pm 2 \mu\text{m}$ . This change in propagation length also corresponds to the system presented by Demidov and suggests the occurrence of another spin-wave mode.

For the second measured frequency of 9.00 GHz, the 2D spin-wave intensity map looks remarkably different, as can be seen in Figure 4.4 (e). In this case, the transmitted spin-wave is confined to the middle of the waveguide.

The summed intensity for this frequency is shown Figure 4.4 (f). We can again observe the decrease of the intensity in the position of the domain wall, but the signal to noise ratio is not sufficient for any analysis.

### Phase-resolved linescans

The corresponding spin-wave phase ( $\Phi$ ), obtained by the technique described in [91, 111], shows a linear increase in the region  $-1 \mu\text{m} < x < 1 \mu\text{m}$  [Figure 4.5 (a), blue region] as expected for a propagating wave. Outside of this region, the phase could not be reconstructed due to either nonlinear spin-wave behavior (closer to the antenna) or insufficient spin-wave signal (farther from the antenna). We determine the wavelength of the excited spin waves from the slope of the fitted line [Figure 4.5 (a), red line],  $\lambda = 4.5 \pm 0.2 \mu\text{m}$ , which is in agreement with the calculated dispersion relation [26].

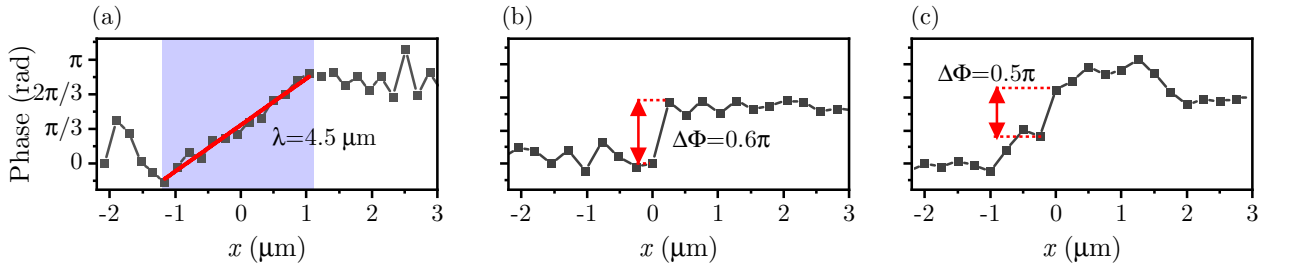


**Figure 4.5:** (a) Evolution of the spin-wave phase along with the white dashed line at the frequency of 7.15 GHz in single domain state, and (b) domain wall state. (c) Spin-wave phase for excitation frequency of 9.00 GHz in domain wall state. The blue region in (a) indicates a region of detectable linear phase evolution. The red line represents the linear fit of this data, and the spin-wave wavelength is calculated from the slope of the fitted line.

The phase evolution in the lower spin-wave beam [Figure 4.5 (b)] exhibits a clear discontinuity, a phase shift of approximately  $0.6\pi$  at the domain wall position. The phase shift is also apparent for the frequency of 9.00 GHz, with the value of  $0.5\pi$ .

### 4.3.3. Micromagnetic simulations

To further understand this frequency-dependent behavior and phase evolution, we conducted dynamic micromagnetic simulations, using the same material parameters as for the calculation of the static magnetization configuration. Spin waves were excited by a spatially varying field (the field from the rectangular antenna was calculated by FEMM [134]). To prevent reflections at the ends of the simulated waveguide, we implemented regions with increasing damping at both ends of the waveguide. A continuous RF excitation was applied during the initial 20 periods. Then the spatial distribution of the magnetization was sampled for two periods with a time step of 2 ps. The magnetization was transformed to in-plane ( $m_{\text{ip}}$ ) and out-of-plane ( $m_{\text{oop}}$ ) components

$$m_{\text{oop}} = \vec{e}_z \cdot \vec{M}_0(\vec{r}), \quad (4.1a)$$

$$m_{\text{ip}} = (\vec{M}_0(\vec{r}) \times \vec{e}_z) \cdot \vec{M}(\vec{r}, t), \quad (4.1b)$$

where  $\vec{M}(\vec{r}, t)$  is magnetization, and  $\vec{M}_0(\vec{r})$  is the static magnetization. The spin-wave phase ( $\Phi$ ) was calculated using

$$\Phi = \text{atan} \left( \frac{m_{\text{oop}}}{m_{\text{ip}}} \right), \quad (4.2)$$

following the procedure described in [135]. The summed simulated spin-wave intensity in dependence on  $x$  dimension are shown in Figure 4.6. In the case of single domain state at 7.15 GHz we can observe linear decrease of intensity. The change of the slope, thus the change of the propagation length, is apparent also in the simulation as can be seen in Figure 4.6 (b). The same dip in the intensity is apparent for the domain wall state at 9.00 GHz as can be seen in Figure 4.6 (c).

The 2D simulated maps are shown in Figure 4.7 (a-c) in the form of the time-averaged squared out-of-plane component of the magnetization. Panel (a) shows the spin-wave propagation in the single-domain state. Panel (b) shows the spin wave-propagation through the domain wall at the excitation frequency of 7.15 GHz. Panel (c) shows the spin-wave

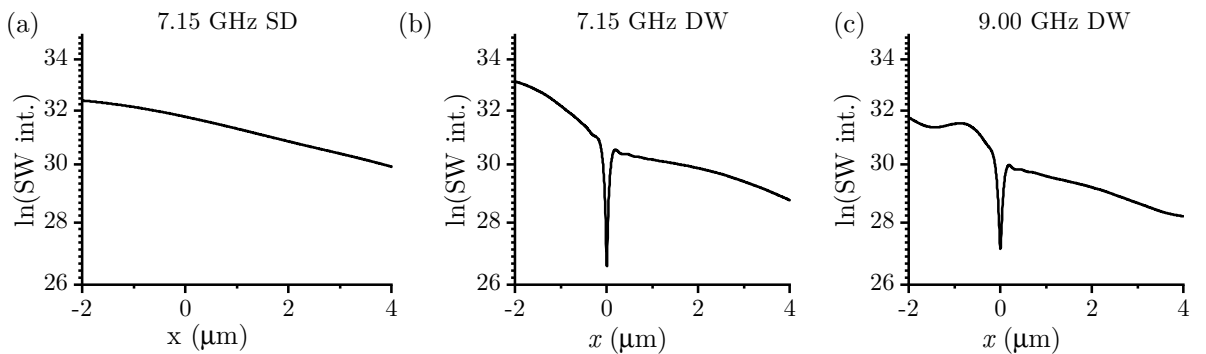


**Figure 4.6:** The intensity of spin waves in logarithmic scale at (a) 7.15 GHz single domain state, (b) domain wall state and at 9.00 GHz domain wall state (c).

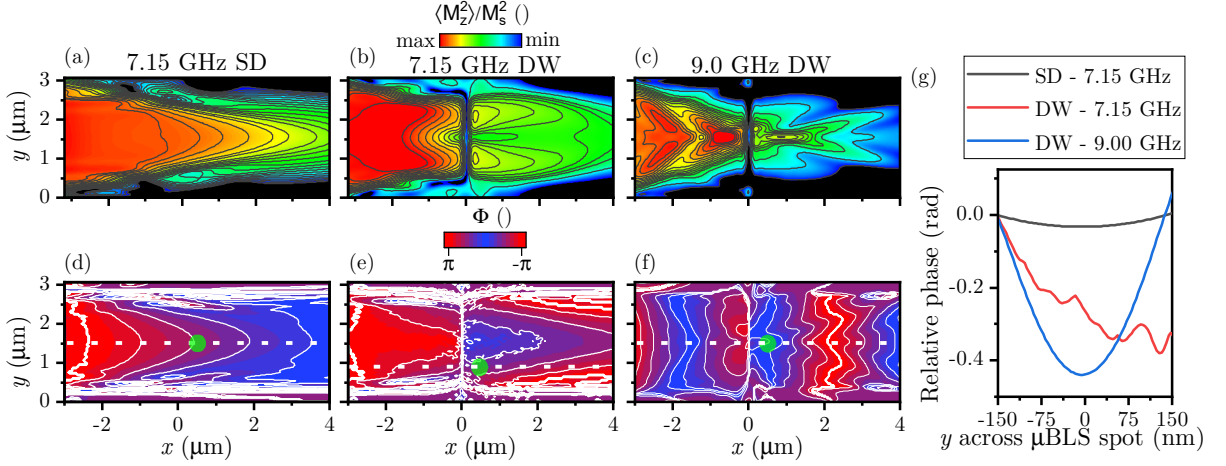


**Figure 4.7:** (a)-(c) Simulated 2D maps of the squared out-of-plane magnetization component averaged over two periods of excitation. (a) single-domain state, (b) domain wall state excited at 7.15 GHz and (c) domain wall state excited at 9.00 GHz. (d)-(f) Phase maps corresponding to the respective intensity maps. (d) single-domain state, (e) domain wall state excited at 7.15 GHz, and (f) domain wall state excited at 9.00 GHz. The white dashed lines indicate the positions where the phase was experimentally measured. The green dots represent  $\mu$ BLS spots at which the simulated relative phase is evaluated in panel (g).

propagation at the frequency of 9.00 GHz. We can observe qualitatively the same behavior as in the experiment.

In order to further explain the spin-wave intensity pattern we investigate reflection coefficient ( $R$ ) of the domain wall. We define the reflection coefficient as

$$R = 1 - \frac{I_{\text{DW}}}{I_{\text{SD}}}, \quad (4.3)$$

where  $I$  is the spin-wave intensity at  $x = 0.1 \mu\text{m}$  with and without the presence of domain wall) increases dramatically from  $R = 0.025$  to  $R = 0.221$  for 7.15 GHz and 9.00 GHz, respectively. Due to this enhanced reflection at 9 GHz, the spatial profile of the SW is strongly affected even before it reaches the domain wall. This can be further observed in the summed intensity, which is shown in Figure 4.6 (a) and (b).

The simulated phase maps corresponding to the previously described intensity maps are shown in Figure 4.7 (d-f). For the waveguide in the single domain state, we can observe that the phase is almost constant across the  $y$  coordinate of the  $\mu$ BLS spot [see a green dot in 4.7 (d) and black line in 4.7 (g)]. On the other hand, the phase after passing the domain wall is much more distorted across a relatively small distance [for 7.15 GHz see green dot in 4.7 (e) and the red line in 4.6 (c)] and the same applies to 9.00 GHz spin wave [see 4.7 (f), green dot and 4.6 (c), blue line]. This distortion explains why we were not able to see the linear phase evolution in our experiments. We were probing the spin waves with a 300 nm  $\mu$ BLS spot, and the phase is changing by more than 0.5 rad within the spot size.

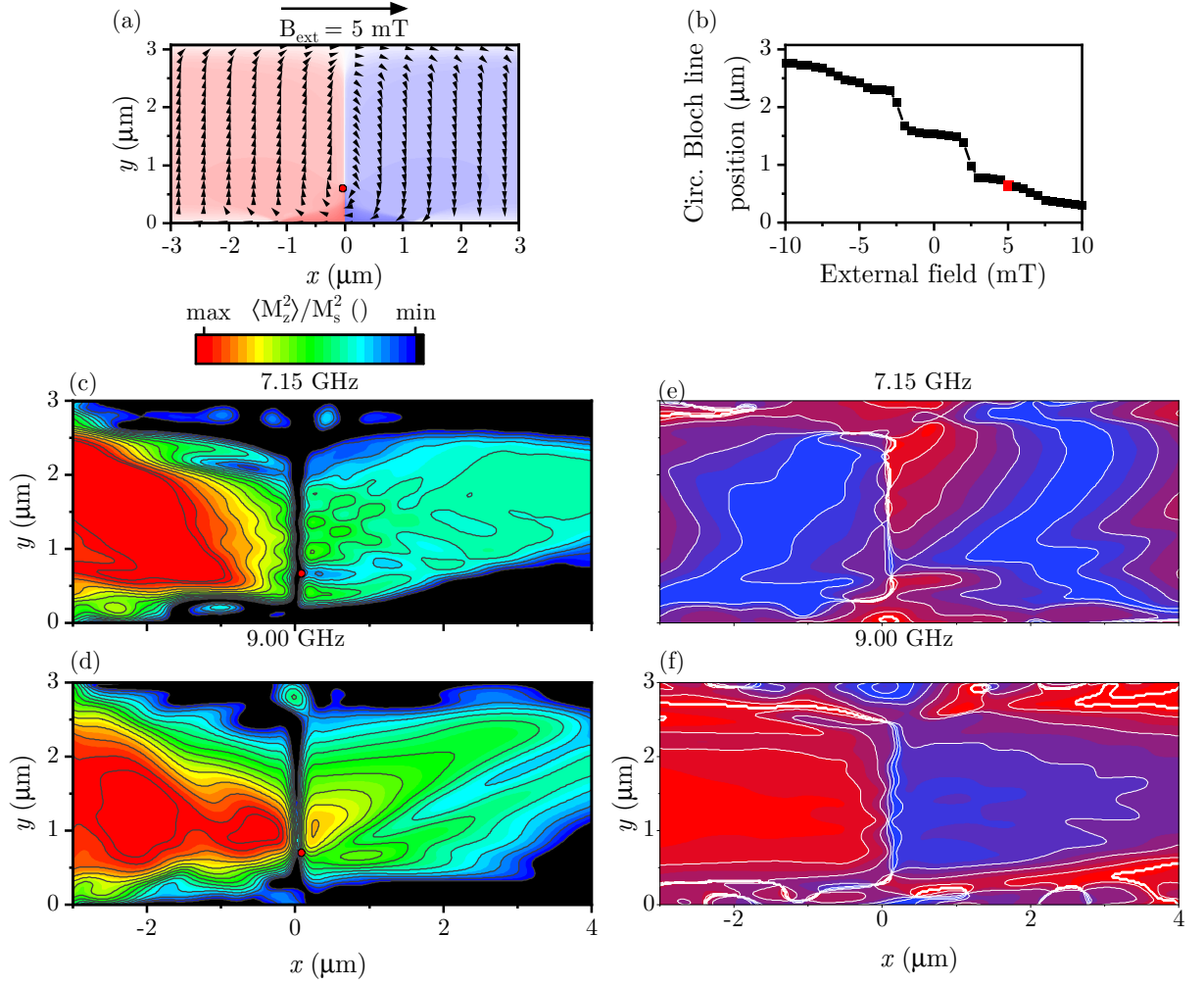


**Figure 4.8:** (a) Magnetization configuration with the external field of 5 mT applied along the  $x$  dimension. The red dots shown in all panels indicate the position of the circular Bloch line in this field. (b) Simulated circular Bloch line displacement as a function of the external field in  $x$  direction (c-d) Simulated 2D maps of spin-wave propagation in an applied field of 5 mT along the waveguide long axis (c) for frequency 7.15 GHz (d) and for the frequency 9.00 GHz. (e-f) Corresponding phases for the frequencies of 7.15 GHz and 9 GHz.

## 4.4. Displacement of the circular Bloch line

To check if a change in the internal configuration of the domain wall can be used to modify the spin-wave propagation, we performed a simulation where we applied a small external magnetic field of 5 mT along the  $x$  direction. This moves the circular Bloch line in  $y$ -direction towards the edge of the waveguide [see Figure 4.8 (a)]. The field dependence of the Bloch line position along the  $y$  axis is shown in Figure 4.8 (b).

This displacement of the circular Bloch line changes the transmitted spin-wave profile significantly. In Figure 4.8 (c) we can observe that for 7.15 GHz, the Bloch line still casts a shadow in the spin-wave intensity; only little space and intensity are left for the lower beam ( $y < 0.7 \mu\text{m}$ ). At  $f = 9 \text{ GHz}$ , as in Figure 4.8 (d), a maximum is seen downstream of the Bloch line, but now displaced sideways, and the wave pattern appears bent. The corresponding phases for the frequencies of 7.15 GHz and 9 GHz are shown in Figure 4.8 (e, f).

# Conclusion

Even though Brillouin light scattering has been used for decades, it still presents new challenges and motivation for further development. Originally the Brillouin light scattering was used for  $k$ -resolved measurements of thin films. Later it was transformed into a more versatile tool providing the sub-micrometer spatial resolution, time resolution and ability to extract a spin-wave phase. The last mentioned method is crucial for the design and development of the spin-wave logic circuits based on the phase manipulation. The goal of this thesis was to develop and characterize a setup with this capability. The setup was then used to conduct a recently published study on propagation of spin waves through a domain wall.

In the first chapter we discussed the basics of the theory of magnetism and spin waves. In the first section, the micromagnetic energies were introduced. These were further used to present an effective field. The full dipole-exchange dispersion relation was shown. We showed both cases, with totally pinned and totally unpinned boundary conditions. The case with a quantized  $k$ -vector was also investigated. This dispersion relation was then used to obtain group velocity, lifetime, and resulting propagation lengths of spin waves. The presented theory was used for the computation of these parameters for materials that are used in the current spin-wave research.

The second chapter discussed the theory of light scattering. The first section examined the scattering with a classical approach. The cases of elastic Rayleigh and Mie scattering were presented. The inelastic scattering was interpreted as the Doppler shift of the incident light on the moving grating of an index of refraction. Based on the quantum treatment, expressions for scattering cross-sections of quasi-elastic, Raman, and Brillouin light scattering were given. In the last section, the current types of Brillouin light scattering setups and their applications were reviewed.

The following chapter revealed the details of the design and characterization of the developed Brillouin light scattering experimental setup. We presented the scheme of the whole setup and discussed in detail characteristics of each part. We measured the stability of both used lasers. The output power of both lasers is oscillating in the range of 1.5%. The measurement after a Fabry-Perot etalon reveals that the oscillations increase to approximately 2%. This stability allows long term measurements. We characterized the electro-optic modulator efficiency for different driving frequencies. We found that the modulated power is the highest around 2.5 GHz and the highest achievable frequency is approximately 12 GHz. This characteristics allows us to perform a phase-resolved measurement in wide range of frequencies. Using the knife-edge technique we determined the optical resolution to be  $270 \pm 30$  nm. We also measured the stability of the alignment of our Tandem-Fabry-Perot interferometer as a function of the dither parameter to optimize long term measurements. The best value was found to be 0.01 V, where the reference signal oscillations were within 10% during 12-hour-long-measurement. At the end of the chapter, the setup was verified on the well-known system of thin permalloy

film with full phase reconstruction measurement. The obtained results were in agreement with theoretical predictions.

The last chapter presents a study done with the developed setup. We stabilized a symmetric Néel domain wall with a topologically enforced circular Bloch line confined in a magnetic waveguide with imprinted uniaxial anisotropy in the vicinity of a microwave antenna. This configuration allowed us to experimentally observe zero-magnetic-field propagation of Damon-Eshbach spin waves through a domain wall by phase-resolved  $\mu$ BLS. We observed two different regimes of spin-wave propagation appearing at frequencies of 7.15 GHz and 9.00 GHz. In the first regime, which was observed at the frequency of 7.15 GHz, spin-wave propagation in the vicinity of the circular Bloch line is suppressed, and two spin-wave beams are created. On the contrary, at 9.00 GHz spin waves propagate through the circular Bloch line and create a single spin-wave beam. Phase-resolved measurements reveal that spin waves exhibit a phase shift of approximately  $0.6\pi$  upon transmission through the domain wall. We observed that the domain wall spatially distorts the phase of the spin wave. This effect needs to be taken into account when designing domain wall-based phase shifters or other devices relying on the spin-wave phase manipulation. The other point, which needs to be taken into consideration, is the occurrence of topologically enforced spin structures which are unavoidable in certain geometries. They can limit the performance or functionality of domain wall-based devices. On the other hand, they can also be an advantage, as in the case where we propose an interesting technique for spin-wave guidance by manipulating the circular Bloch line position in the domain wall by external magnetic fields. This technique can be used for dynamical turning or blocking spin waves in future magnonic devices.

In summary, we developed a versatile tool for spin wave studies with sub-micrometer resolution and the possibilities to extract the spin-wave phase. This setup is currently used for spin-wave research. In the future, we plan to extend setup to be capable of time-resolved measurement and the possibility to measure only specific  $k$ -vectors.

# References

1. Von Neumann, J. First Draft of a Report on the EDVAC. *IEEE Annals of the History of Computing* **15**, 27–75 (1993) (cit. on p. 1).
2. Moore, G. E. Cramming more components onto integrated circuits. *Proceedings of the IEEE* **86**, 82–85 (1998) (cit. on p. 1).
3. Theis, T. N. & Wong, H.-S. P. The end of Moore’s law: A new beginning for information technology. *Computing in Science & Engineering* **19**, 41–50 (2017) (cit. on p. 1).
4. Track, E., Forbes, N. & Strawn, G. The end of Moore’s Law. *Computing in Science & Engineering* **19**, 4–6 (2017) (cit. on p. 1).
5. Nature, E. Big Data Needs a Hardware Revolution. *Nat* **554**, 145–146 (2018) (cit. on p. 1).
6. Stamps, R. L., Breitzkreutz, S., Åkerman, J., Chumak, A. V., Otani, Y., Bauer, G. E., Thiele, J.-U., Bowen, M., Majetich, S. A., Kläui, M., *et al.* The 2014 magnetism roadmap. *Journal of Physics D: Applied Physics* **47**, 333001 (2014) (cit. on p. 1).
7. Waldrop, M. M. More than Moore. *Nature* **530**, 144–148 (2016) (cit. on p. 1).
8. Leiserson, C. E., Thompson, N. C., Emer, J. S., Kuszmaul, B. C., Lampson, B. W., Sanchez, D. & Schardl, T. B. There’s plenty of room at the Top: What will drive computer performance after Moore’s law? *Science* **368** (2020) (cit. on p. 1).
9. Zhang, Y., Zhao, W., Klein, J.-O., Kang, W., Querlioz, D., Zhang, Y., Ravelosona, D. & Chappert, C. *Spintronics for low-power computing in 2014 Design, Automation & Test in Europe Conference & Exhibition (DATE)* (2014), 1–6 (cit. on p. 1).
10. Chumak, A. V. Fundamentals of magnon-based computing. *arXiv:1901.08934* (2019) (cit. on pp. 1, 9, 11).
11. Chumak, A., Serga, A. & Hillebrands, B. Magnonic crystals for data processing. *Journal of Physics D: Applied Physics* **50**, 244001 (2017) (cit. on pp. 1, 11).
12. Chumak, A. V., Serga, A. A. & Hillebrands, B. Magnon transistor for all-magnon data processing. *Nature communications* **5**, 1–8 (2014) (cit. on p. 1).
13. Prabhakar, A. & Stancil, D. D. *Spin waves: Theory and applications* (Springer, 2009) (cit. on pp. 1, 7, 9).
14. Chumak, A. V., Vasyuchka, V. I., Serga, A. A. & Hillebrands, B. Magnon spintronics. *Nature Physics* **11**, 453–461 (2015) (cit. on p. 1).
15. Schloemann, E. & Blight, R. E. Broad-band stripline circulators based on YIG and Li-ferrite single crystals. *IEEE transactions on microwave theory and techniques* **34**, 1394–1400 (1986) (cit. on p. 1).

16. Sebastian, T., Schultheiss, K., Obry, B., Hillebrands, B. & Schultheiss, H. Micro-focused Brillouin light scattering: imaging spin waves at the nanoscale. *Frontiers in Physics* **3**, 35 (2015) (cit. on p. 1).
17. Wojewoda, O., Hula, T., Flajšman, L., Vaňatka, M., Gloss, J., Holobrádek, J., Staňo, M., Stienen, S., Körber, L., Schultheiß, K., Schmid, M., Schultheiß, H. & Urbánek, M. Propagation of spin waves through a Néel domain wall. *arXiv preprint arXiv:2005.05690* (2020) (cit. on p. 2).
18. Hillebrands, B. & Ounadjela, K. *Spin dynamics in confined magnetic structures I* (Springer Science & Business Media, 2003) (cit. on p. 5).
19. Suhl, H. *et al. Relaxation processes in micromagnetics* (Oxford University Press, 2007) (cit. on p. 5).
20. Hickey, M. C. & Moodera, J. S. Origin of intrinsic Gilbert damping. *Physical review letters* **102**, 137601 (2009) (cit. on p. 6).
21. Kittel, C. On the theory of ferromagnetic resonance absorption. *Physical review* **73**, 155 (1948) (cit. on p. 6).
22. Turčan, I. *Study of magnonic crystals in a frequency domain* MA thesis (Brno University of Technology, July 2017) (cit. on p. 6).
23. Wojewoda, O. *Disperzní relace magnonických krystalů s netriviální prostorovou distribucí magnetické anizotropie* BA thesis (Brno University of Technology, July 2018) (cit. on p. 7).
24. Damon, R. W. & Eshbach, J. Magnetostatic modes of a ferromagnet slab. *Journal of Physics and Chemistry of Solids* **19**, 308–320 (1961) (cit. on p. 7).
25. Eshbach, J. & Damon, R. Surface magnetostatic modes and surface spin waves. *Physical Review* **118**, 1208 (1960) (cit. on p. 7).
26. Kalinikos, B. & Slavin, A. Theory of dipole-exchange spin wave spectrum for ferromagnetic films with mixed exchange boundary conditions. *Journal of Physics C: Solid State Physics* **19**, 7013 (1986) (cit. on pp. 7, 50, i).
27. Pirro, P., Brächer, T., Chumak, A., Lägel, B., Dubs, C., Surzhenko, O., Görnert, P., Leven, B. & Hillebrands, B. Spin-wave excitation and propagation in microstructured waveguides of yttrium iron garnet/Pt bilayers. *Applied Physics Letters* **104**, 012402 (2014) (cit. on pp. 11, 27).
28. Hahn, C., Naletov, V. V., de Loubens, G., Klein, O., d’Allivy Kelly, O., Anane, A., Bernard, R., Jacquet, E., Bortolotti, P., Cros, V., Prieto, J. L. & Muñoz, M. Measurement of the intrinsic damping constant in individual nanodisks of  $\text{Y}_3\text{Fe}_5\text{O}_{12}$  and  $\text{Y}_3\text{Fe}_5\text{O}_{12}$ |Pt. *Applied Physics Letters* **104**, 152410 (2014) (cit. on p. 11).
29. Dubs, C., Surzhenko, O., Linke, R., Danilewsky, A., Brückner, U. & Dellith, J. Sub-micrometer yttrium iron garnet LPE films with low ferromagnetic resonance losses. *Journal of Physics D: Applied Physics* **50**, 204005 (2017) (cit. on p. 11).
30. Sun, Y., Song, Y.-Y., Chang, H., Kabatek, M., Jantz, M., Schneider, W., Wu, M., Schultheiss, H. & Hoffmann, A. Growth and ferromagnetic resonance properties of nanometer-thick yttrium iron garnet films. *Applied Physics Letters* **101**, 152405 (2012) (cit. on p. 11).

31. Yu, H., Kelly, O. d., Cros, V., Bernard, R., Bortolotti, P., Anane, A., Brandl, F., Huber, R., Stasinopoulos, I. & Grundler, D. Magnetic thin-film insulator with ultra-low spin wave damping for coherent nanomagnonics. *Scientific reports* **4**, 1–5 (2014) (cit. on p. 11).
32. Onbasli, M., Kehlberger, A., Kim, D. H., Jakob, G., Kläui, M., Chumak, A. V., Hillebrands, B. & Ross, C. A. Pulsed laser deposition of epitaxial yttrium iron garnet films with low Gilbert damping and bulk-like magnetization. *APL Materials* **2**, 106102 (2014) (cit. on p. 11).
33. Liu, T., Chang, H., Vlaminc, V., Sun, Y., Kabatek, M., Hoffmann, A., Deng, L. & Wu, M. Ferromagnetic resonance of sputtered yttrium iron garnet nanometer films. *Journal of Applied Physics* **115**, 17A501 (2014) (cit. on p. 11).
34. Demidov, V. E. & Demokritov, S. O. Magnonic waveguides studied by microfocus Brillouin light scattering. *IEEE Transactions on Magnetics* **51**, 1–15 (2015) (cit. on pp. 11, 27).
35. Kalarickal, S. S., Krivosik, P., Wu, M., Patton, C. E., Schneider, M. L., Kabos, P., Silva, T. J. & Nibarger, J. P. Ferromagnetic resonance linewidth in metallic thin films: Comparison of measurement methods. *Journal of Applied Physics* **99**, 093909 (2006) (cit. on p. 11).
36. Patton, C. E. Linewidth and Relaxation Processes for the Main Resonance in the Spin-Wave Spectra of Ni–Fe Alloy Films. *Journal of Applied Physics* **39**, 3060–3068 (1968) (cit. on p. 11).
37. Křížáková, V. *Spin wave excitation and propagation in magnonic crystal prepared by focused ion beam direct writing* MA thesis (Brno University of Technology, July 2018) (cit. on p. 11).
38. Brunsch, A. Magnetic properties and corrosion resistance of (CoFeB) 100- xCr<sub>x</sub> thin films. *Journal of Applied Physics* **50**, 7603–7605 (1979) (cit. on p. 11).
39. Liu, X., Zhang, W., Carter, M. J. & Xiao, G. Ferromagnetic resonance and damping properties of CoFeB thin films as free layers in MgO-based magnetic tunnel junctions. *Journal of Applied Physics* **110**, 033910 (2011) (cit. on p. 11).
40. Conca, A., Greser, J., Sebastian, T., Klingler, S., Obry, B., Leven, B. & Hillebrands, B. Low spin-wave damping in amorphous Co<sub>40</sub>Fe<sub>40</sub>B<sub>20</sub> thin films. *Journal of Applied Physics* **113**, 213909 (2013) (cit. on p. 11).
41. Flajšman, L., Wagner, K., Vaňatka, M., Gloss, J., Křížáková, V., Schmid, M., Schultheiss, H. & Urbánek, M. Zero-field propagation of spin waves in waveguides prepared by focused ion beam direct writing. *Physical Review B* **101**, 014436 (2020) (cit. on pp. 11, 12, 27, 32).
42. Gloss, J., Horký, M., Křížáková, V., Flajšman, L., Schmid, M., Urbánek, M. & Varga, P. The growth of metastable fcc Fe<sub>78</sub>Ni<sub>22</sub> thin films on H-Si (100) substrates suitable for focused ion beam direct magnetic patterning. *Applied Surface Science* **469**, 747–752 (2019) (cit. on p. 11).
43. Urbánek, M., Flajšman, L., Křížáková, V., Gloss, J., Horký, M., Schmid, M. & Varga, P. Research Update: Focused ion beam direct writing of magnetic patterns with controlled structural and magnetic properties. *APL Materials* **6**, 060701 (2018) (cit. on pp. 11, 45, 46).

44. Gloss, J., Shah Zaman, S., Jonner, J., Novotny, Z., Schmid, M., Varga, P. & Urbánek, M. Ion-beam-induced magnetic and structural phase transformation of Ni-stabilized face-centered-cubic Fe films on Cu (100). *Applied Physics Letters* **103**, 262405 (2013) (cit. on pp. 11, 45).
45. Gloss, J. *Magnetic transformation of metastable fcc Fe/Cu (100) films by focused ion beam* MA thesis (Brno University of Technology, July 2014) (cit. on p. 11).
46. Lilienfeld, P. *A blue sky history* **6** (Optical Society of America, 2004) (cit. on p. 13).
47. Strutt, J. W. XV. On the light from the sky, its polarization and colour. *The London, Edinburgh, and Dublin Philosophical Magazine and Journal of Science* **41**, 107–120 (1871) (cit. on p. 13).
48. Lockwood, D. J. *Rayleigh and Mie Scattering* (ed Luo, M. R.) 1097–1107. ISBN: 978-1-4419-8071-7 (Springer New York, New York, NY, 2016) (cit. on p. 13).
49. Cox, A., DeWeerd, A. J. & Linden, J. An experiment to measure Mie and Rayleigh total scattering cross sections. *American Journal of Physics* **70**, 620–625 (2002) (cit. on p. 14).
50. Raman, C. Doppler effect in light-scattering. *Nature* **128**, 636–636 (1931) (cit. on p. 15).
51. Johnson, C. S. & Gabriel, D. A. *Laser light scattering* (Dover, 1981) (cit. on p. 15).
52. Loudon, R. *The quantum theory of light* (OUP Oxford, 2000) (cit. on p. 16).
53. Malard, L., Pimenta, M., Dresselhaus, G. & Dresselhaus, M. Raman spectroscopy in graphene. *Physics reports* **473**, 51–87 (2009) (cit. on p. 16).
54. Gala, U. & Chauhan, H. Principles and applications of Raman spectroscopy in pharmaceutical drug discovery and development. *Expert opinion on drug discovery* **10**, 187–206 (2015) (cit. on p. 16).
55. Evans, C. L. & Xie, X. S. Coherent anti-Stokes Raman scattering microscopy: chemical imaging for biology and medicine. *Annu. Rev. Anal. Chem.* **1**, 883–909 (2008) (cit. on p. 16).
56. Cottam, M. Theory of light scattering off the surface of a Heisenberg ferromagnet. *Journal of Physics C: Solid State Physics* **9**, 2137 (1976) (cit. on p. 17).
57. Cochran, J. & Dutcher, J. Calculation of the intensity of light scattered from magnons in thin films. *Journal of magnetism and magnetic materials* **73**, 299–310 (1988) (cit. on p. 18).
58. Le Gall, H. & Jamet, J. Theory of the Elastic and Inelastic Scattering of Light by Magnetic Crystals. I. First-Order Processes. *physica status solidi (b)* **46**, 467–482 (1971) (cit. on p. 18).
59. Le Gall, H., Vien, T. K. & Desormiere, B. Theory of the elastic and inelastic scattering of light by magnetic crystals. II. Second-order processes. *physica status solidi (b)* **47**, 591–606 (1971) (cit. on p. 18).
60. Meng, Z., Traverso, A. J. & Yakovlev, V. V. Background clean-up in Brillouin microspectroscopy of scattering medium. *Optics express* **22**, 5410–5415 (2014) (cit. on p. 18).

61. Shirasaki, M. Large angular dispersion by a virtually imaged phased array and its application to a wavelength demultiplexer. *Optics letters* **21**, 366–368 (1996) (cit. on p. 18).
62. Correa, N., Harding, S., Bailey, M., Brasselet, S. & Palombo, F. Image analysis applied to Brillouin images of tissue-mimicking collagen gels. *Biomedical optics express* **10**, 1329–1338 (2019) (cit. on p. 19).
63. Palombo, F. & Fioretto, D. Brillouin Light Scattering: Applications in Biomedical Sciences. *Chemical reviews* **119**, 7833–7847 (2019) (cit. on p. 19).
64. Bevilacqua, C., Sánchez-Iranzo, H., Richter, D., Diz-Muñoz, A. & Prevedel, R. Imaging mechanical properties of sub-micron ECM in live zebrafish using Brillouin microscopy. *Biomedical Optics Express* **10**, 1420–1431 (2019) (cit. on p. 19).
65. Shao, P., Eltony, A. M., Seiler, T. G., Tavakol, B., Pineda, R., Koller, T., Seiler, T. & Yun, S.-H. Spatially-resolved Brillouin spectroscopy reveals biomechanical changes in early ectatic corneal disease and post-crosslinking in vivo. *arXiv preprint arXiv:1802.01055* (2018) (cit. on pp. 19, 20).
66. Yun, S. H. & Chernyak, D. Brillouin microscopy: assessing ocular tissue biomechanics. *Current opinion in ophthalmology* **29**, 299 (2018) (cit. on p. 20).
67. Sandercock, J. *High contrast tandem Fabry-Perot interferometer* version 1703/1.5. Table Stable (Mar. 20, 2017). 87 pp. In press (cit. on p. 20).
68. Pine, A. Thermal Brillouin scattering in cadmium sulfide: velocity and attenuation of sound; acoustoelectric effects. *Physical Review B* **5**, 2997 (1972) (cit. on p. 21).
69. Cannell, D. S. & Benedek, G. B. Brillouin spectrum of xenon near its critical point. *Physical Review Letters* **25**, 1157 (1970) (cit. on p. 22).
70. Sandercock, J. R. *Fabry-perot interferometer* US Patent 4,225,236. Sept. 30, 1980 (cit. on p. 22).
71. Sandercock, J. R. *Stable Fabry-Perot interferometer* US Patent 6,989,906. Jan. 24, 2006 (cit. on p. 22).
72. Lindsay, S., Anderson, M. & Sandercock, J. Construction and alignment of a high performance multipass vernier tandem Fabry–Perot interferometer. *Review of scientific instruments* **52**, 1478–1486 (1981) (cit. on p. 22).
73. Mock, R., Hillebrands, B. & Sandercock, R. Construction and performance of a Brillouin scattering set-up using a triple-pass tandem Fabry-Perot interferometer. *Journal of Physics E: Scientific Instruments* **20**, 656 (1987) (cit. on p. 24).
74. Ordóñez-Romero, C. L., Kalinikos, B. A., Krivosik, P., Tong, W., Kabos, P. & Patton, C. E. Three-magnon splitting and confluence processes for spin-wave excitations in yttrium iron garnet films: Wave vector selective Brillouin light scattering measurements and analysis. *Physical Review B* **79**, 144428 (2009) (cit. on p. 24).
75. Harzer, J., Hillebrands, B., Stamps, R., Güntherodt, G., England, C. & Falco, C. M. Magnetic properties of Co/Pd multilayers determined by Brillouin light scattering and SQUID magnetometry. *Journal of applied physics* **69**, 2448–2454 (1991) (cit. on pp. 24, 25).

76. Fassbender, J., Güntherodt, G., Mathieu, C., Hillebrands, B., Jungblut, R., Kohlhepp, J., Johnson, M., Roberts, D. & Gehring, G. Correlation between structure and magnetic anisotropies of Co on Cu (110). *Physical Review B* **57**, 5870 (1998) (cit. on p. 24).
77. Demokritov, S., Mathieu, C., Bauer, M., Riedling, S., Büttner, O., De Gronckel, H. & Hillebrands, B. Interface anisotropy and magnetization reversal in epitaxial Fe (001)/Pd double layers. *Journal of magnetism and magnetic materials* **165**, 496–499 (1997) (cit. on p. 24).
78. Hillebrands, B., Mathieu, C., Bauer, M., Demokritov, S., Bartenlian, B., Chappert, C., Decanini, D., Rousseaux, F. & Carcenac, F. Brillouin light scattering investigations of structured permalloy films. *Journal of applied physics* **81**, 4993–4995 (1997) (cit. on p. 25).
79. Mathieu, C., Jorzick, J., Frank, A., Demokritov, S. O., Slavin, A. N., Hillebrands, B., Bartenlian, B., Chappert, C., Decanini, D., Rousseaux, F. & Cambril, E. Lateral quantization of spin waves in micron size magnetic wires. *Physical review letters* **81**, 3968 (1998) (cit. on p. 25).
80. Gubbiotti, G., Tacchi, S., Madami, M., Carlotti, G., Adeyeye, A. & Kostylev, M. Brillouin light scattering studies of planar metallic magnonic crystals. *Journal of Physics D: Applied Physics* **43**, 264003 (2010) (cit. on p. 25).
81. Tacchi, S., Duerr, G., Klos, J., Madami, M., Neusser, S., Gubbiotti, G., Carlotti, G., Krawczyk, M. & Grundler, D. Forbidden band gaps in the spin-wave spectrum of a two-dimensional bicomponent magnonic crystal. *Physical review letters* **109**, 137202 (2012) (cit. on p. 25).
82. Tacchi, S., Montoncello, F., Madami, M., Gubbiotti, G., Carlotti, G., Giovannini, L., Zivieri, R., Nizzoli, F., Jain, S., Adeyeye, A. O. & Singh, N. Band diagram of spin waves in a two-dimensional magnonic crystal. *Physical review letters* **107**, 127204 (2011) (cit. on p. 25).
83. Jorzick, J., Demokritov, S., Mathieu, C., Hillebrands, B., Bartenlian, B., Chappert, C., Rousseaux, F. & Slavin, A. Brillouin light scattering from quantized spin waves in micron-size magnetic wires. *Physical Review B* **60**, 15194 (1999) (cit. on p. 25).
84. Dzyaloshinsky, I. A thermodynamic theory of “weak” ferromagnetism of antiferromagnetics. *Journal of Physics and Chemistry of Solids* **4**, 241–255 (1958) (cit. on p. 25).
85. Belmeguenai, M., Adam, J.-P., Roussigné, Y., Eimer, S., Devolder, T., Kim, J.-V., Cherif, S. M., Stashkevich, A. & Thiaville, A. Interfacial Dzyaloshinskii-Moriya interaction in perpendicularly magnetized Pt/Co/AlO<sub>x</sub> ultrathin films measured by Brillouin light spectroscopy. *Physical Review B* **91**, 180405 (2015) (cit. on p. 25).
86. Soucaille, R., Belmeguenai, M., Torrejon, J., Kim, J.-V., Devolder, T., Roussigné, Y., Chérif, S.-M., Stashkevich, A., Hayashi, M. & Adam, J.-P. Probing the Dzyaloshinskii-Moriya interaction in CoFeB ultrathin films using domain wall creep and Brillouin light spectroscopy. *Physical Review B* **94**, 104431 (2016) (cit. on p. 25).
87. Cho, J., Kim, N.-H., Lee, S., Kim, J.-S., Lavrijsen, R., Solignac, A., Yin, Y., Han, D.-S., Van Hoof, N. J., Swagten, H. J., *et al.* Thickness dependence of the interfacial Dzyaloshinskii–Moriya interaction in inversion symmetry broken systems. *Nature communications* **6**, 1–7 (2015) (cit. on p. 25).

88. Weinhold, T. *Comparison of different approaches of wave vector resolved Brillouin light scattering spectroscopy for investigating interfacial Dzyaloshinskii–Moriya Interaction* MA thesis (Technische Universität Dresden, 2019) (cit. on p. 25).
89. Belmeguenai, M., Gabor, M., Roussigné, Y., Stashkevich, A., Chérif, S., Zighem, F. & Tiusan, C. Brillouin light scattering investigation of the thickness dependence of Dzyaloshinskii-Moriya interaction in  $\text{Co}_{0.5}\text{Fe}_{0.5}$  ultrathin films. *Physical Review B* **93**, 174407 (2016) (cit. on p. 25).
90. Kittel, C., McEuen, P. & McEuen, P. *Introduction to solid state physics* (Wiley New York, 1996) (cit. on p. 26).
91. Pirro, P., Brächer, T., Vogt, K., Obry, B., Schultheiss, H., Leven, B. & Hillebrands, B. Interference of coherent spin waves in micron-sized ferromagnetic waveguides. *physica status solidi (b)* **248**, 2404–2408 (2011) (cit. on pp. 27, 50).
92. Vogt, K., Fradin, F. Y., Pearson, J. E., Sebastian, T., Bader, S. D., Hillebrands, B., Hoffmann, A. & Schultheiss, H. Realization of a spin-wave multiplexer. *Nature communications* **5**, 1–5 (2014) (cit. on p. 27).
93. Demidov, V. E., Kostylev, M. P., Rott, K., Krzysteczko, P., Reiss, G. & Demokritov, S. O. Excitation of microwaveguide modes by a stripe antenna. *Applied Physics Letters* **95**, 112509 (2009) (cit. on pp. 27, 50).
94. Demidov, V. E., Demokritov, S. O., Rott, K., Krzysteczko, P. & Reiss, G. Mode interference and periodic self-focusing of spin waves in permalloy microstrips. *Physical Review B* **77**, 064406 (2008) (cit. on p. 27).
95. Demidov, V., Kostylev, M., Rott, K., Münchenberger, J., Reiss, G. & Demokritov, S. Excitation of short-wavelength spin waves in magnonic waveguides. *Applied Physics Letters* **99**, 082507 (2011) (cit. on pp. 27, 50).
96. Sadvnikov, A., Davies, C., Kruglyak, V., Romanenko, D., Grishin, S., Beginin, E., Sharaevskii, Y. & Nikitov, S. Spin wave propagation in a uniformly biased curved magnonic waveguide. *Physical Review B* **96**, 060401 (2017) (cit. on p. 27).
97. Vogt, K., Schultheiss, H., Jain, S., Pearson, J., Hoffmann, A., Bader, S. & Hillebrands, B. Spin waves turning a corner. *Applied Physics Letters* **101**, 042410 (2012) (cit. on p. 27).
98. Obry, B., Pirro, P., Brächer, T., Chumak, A. V., Osten, J., Ciubotaru, F., Serga, A. A., Fassbender, J. & Hillebrands, B. A micro-structured ion-implanted magnonic crystal. *Applied Physics Letters* **102**, 202403 (2013) (cit. on pp. 27, 28).
99. Chumak, A. V., Pirro, P., Serga, A. A., Kostylev, M., Stamps, R., Schultheiss, H., Vogt, K., Hermsdoerfer, S., Laegel, B., Beck, P., *et al.* Spin-wave propagation in a microstructured magnonic crystal. *Applied Physics Letters* **95**, 262508 (2009) (cit. on p. 27).
100. Wagner, K., Kákay, A., Schultheiss, K., Henschke, A., Sebastian, T. & Schultheiss, H. Magnetic domain walls as reconfigurable spin-wave nanochannels. *Nature nanotechnology* **11**, 432–436 (2016) (cit. on pp. 28, 45).
101. Sadvnikov, A. V., Davies, C. S., Grishin, S. V., Kruglyak, V., Romanenko, D., Sharaevskii, Y. P. & Nikitov, S. Magnonic beam splitter: The building block of parallel magnonic circuitry. *Applied Physics Letters* **106**, 192406 (2015) (cit. on p. 28).

102. Chang, L.-J., Chen, J., Qu, D., Tsai, L.-Z., Liu, Y.-F., Kao, M.-Y., Liang, J.-Z., Wu, T.-S., Chuang, T.-M., Yu, H., *et al.* Spin wave injection and propagation in a magnetic nano-channel from a vortex core. *Nano Letters* (2020) (cit. on p. 28).
103. Brächer, T., Pirro, P., Westermann, J., Sebastian, T., Lägel, B., Van de Wiele, B., Vansteenkiste, A. & Hillebrands, B. Generation of propagating backward volume spin waves by phase-sensitive mode conversion in two-dimensional microstructures. *Applied Physics Letters* **102**, 132411 (2013) (cit. on p. 28).
104. Brächer, T., Pirro, P., Heussner, F., Serga, A. & Hillebrands, B. Localized parallel parametric generation of spin waves in a Ni<sub>81</sub>Fe<sub>19</sub> waveguide by spatial variation of the pumping field. *Applied Physics Letters* **104**, 092418 (2014) (cit. on pp. 28, 29).
105. Demidov, V. E., Urazhdin, S., Ulrichs, H., Tiberkevich, V., Slavin, A., Baither, D., Schmitz, G. & Demokritov, S. O. Magnetic nano-oscillator driven by pure spin current. *Nature materials* **11**, 1028–1031 (2012) (cit. on pp. 28, 29).
106. Brächer, T., Pirro, P., Serga, A. & Hillebrands, B. Localized parametric generation of spin waves in a longitudinally magnetized Ni<sub>81</sub>Fe<sub>19</sub> waveguide. *Applied Physics Letters* **103**, 142415 (2013) (cit. on p. 28).
107. Melkov, G., Kobljanskyj, Y. V., Serga, A., Tiberkevich, V. & Slavin, A. Nonlinear amplification and compression of envelope solitons by localized nonstationary parametric pumping. *Journal of Applied Physics* **89**, 6689–6691 (2001) (cit. on p. 28).
108. Madami, M., Bonetti, S., Consolo, G., Tacchi, S., Carlotti, G., Gubbiotti, G., Mancoff, F., Yar, M. A. & Åkerman, J. Direct observation of a propagating spin wave induced by spin-transfer torque. *Nature nanotechnology* **6**, 635 (2011) (cit. on p. 28).
109. Schneider, T., Serga, A., Neumann, T., Hillebrands, B. & Kostylev, M. Phase reciprocity of spin-wave excitation by a microstrip antenna. *Physical Review B* **77**, 214411 (2008) (cit. on pp. 29, 33, 34).
110. Serga, A., Schneider, T., Hillebrands, B., Demokritov, S. & Kostylev, M. Phase-sensitive Brillouin light scattering spectroscopy from spin-wave packets. *Applied physics letters* **89**, 063506 (2006) (cit. on p. 29).
111. Vogt, K., Schultheiss, H., Hermsdoerfer, S., Pirro, P., Serga, A. & Hillebrands, B. All-optical detection of phase fronts of propagating spin waves in a Ni<sub>81</sub>Fe<sub>19</sub> microstripe. *Applied Physics Letters* **95**, 182508 (2009) (cit. on pp. 32, 50).
112. Demidov, V. E., Urazhdin, S. & Demokritov, S. O. Control of spin-wave phase and wavelength by electric current on the microscopic scale. *Applied Physics Letters* **95**, 262509 (2009) (cit. on p. 32).
113. Fallarino, L., Madami, M., Duerr, G., Grundler, D., Gubbiotti, G., Tacchi, S. & Carlotti, G. Propagation of spin waves excited in a permalloy film by a finite-ground coplanar waveguide: A combined phase-sensitive micro-focused Brillouin light scattering and micromagnetic study. *IEEE transactions on magnetics* **49**, 1033–1036 (2013) (cit. on p. 33).
114. Büttner, O., Bauer, M., Demokritov, S., Hillebrands, B., Kivshar, Y. S., Grimalsky, V., Rapoport, Y. & Slavin, A. N. Linear and nonlinear diffraction of dipolar spin waves in yttrium iron garnet films observed by space-and time-resolved Brillouin light scattering. *Physical Review B* **61**, 11576 (2000) (cit. on p. 34).

115. Büttner, O., Bauer, M., Demokritov, S., Hillebrands, B., Kostylev, M., Kalinikos, B. & Slavin, A. Collisions of spin wave envelope solitons and self-focused spin wave packets in yttrium iron garnet films. *Physical review letters* **82**, 4320 (1999) (cit. on p. 34).
116. Schultheiss, H., Vogt, K. & Hillebrands, B. Direct observation of nonlinear four-magnon scattering in spin-wave microconduits. *Physical Review B* **86**, 054414 (2012) (cit. on p. 35).
117. Mathieu, C., Synogatch, V. T. & Patton, C. E. Brillouin light scattering analysis of three-magnon splitting processes in yttrium iron garnet films. *Physical Review B* **67**, 104402 (2003) (cit. on p. 35).
118. Liu, H. J., Riley, G. A., Ordóñez-Romero, C. L., Kalinikos, B. A. & Buchanan, K. S. Time-resolved study of nonlinear three-magnon processes in yttrium iron garnet films. *Physical Review B* **99**, 024429 (2019) (cit. on p. 35).
119. Demokritov, S. O., Demidov, V. E., Dzyapko, O., Melkov, G. A., Serga, A. A., Hillebrands, B. & Slavin, A. N. Bose–Einstein condensation of quasi-equilibrium magnons at room temperature under pumping. *Nature* **443**, 430–433 (2006) (cit. on p. 35).
120. Demidov, V., Dzyapko, O., Demokritov, S., Melkov, G. & Slavin, A. Observation of spontaneous coherence in Bose-Einstein condensate of magnons. *Physical review letters* **100**, 047205 (2008) (cit. on p. 35).
121. Demidov, V., Dzyapko, O., Buchmeier, M., Stockhoff, T., Schmitz, G., Melkov, G. & Demokritov, S. Magnon kinetics and Bose-Einstein condensation studied in phase space. *Physical review letters* **101**, 257201 (2008) (cit. on p. 35).
122. Flajšman, L. *Magneto-optical study of the dynamic properties of magnetic nanostructures and nanostructured metamaterials* PhD thesis (Brno University of Technology, 2020) (cit. on p. 37).
123. Hämäläinen, S. J., Madami, M., Qin, H., Gubbiotti, G. & van Dijken, S. Control of spin-wave transmission by a programmable domain wall. *Nature communications* **9**, 1–8 (2018) (cit. on p. 45).
124. Han, J., Zhang, P., Hou, J. T., Siddiqui, S. A. & Liu, L. Mutual control of coherent spin waves and magnetic domain walls in a magnonic device. *Science* **366**, 1121–1125 (2019) (cit. on p. 45).
125. Han, D.-S., Kim, S.-K., Lee, J.-Y., Hermsdoerfer, S. J., Schultheiss, H., Leven, B. & Hillebrands, B. Magnetic domain-wall motion by propagating spin waves. *Applied Physics Letters* **94**, 112502 (2009) (cit. on p. 45).
126. Yan, P., Wang, X. & Wang, X. All-magnonic spin-transfer torque and domain wall propagation. *Physical Review Letters* **107**, 177207 (2011) (cit. on p. 45).
127. Seo, S.-M., Lee, H.-W., Kohno, H. & Lee, K.-J. Magnetic vortex wall motion driven by spin waves. *Applied Physics Letters* **98**, 012514 (2011) (cit. on p. 45).
128. Woo, S., Delaney, T. & Beach, G. S. Magnetic domain wall depinning assisted by spin wave bursts. *Nature Physics* **13**, 448–454 (2017) (cit. on p. 45).
129. Albisetti, E., Petti, D., Sala, G., Silvani, R., Tacchi, S., Finizio, S., Wintz, S., Calò, A., Zheng, X., Raabe, J., *et al.* Nanoscale spin-wave circuits based on engineered reconfigurable spin-textures. *Communications Physics* **1**, 1–8 (2018) (cit. on p. 45).

130. Aharoni, A. Demagnetizing factors for rectangular ferromagnetic prisms. *Journal of applied physics* **83**, 3432–3434 (1998) (cit. on p. 46).
131. Vansteenkiste, A., Leliaert, J., Dvornik, M., Helsen, M., Garcia-Sanchez, F. & Van Waeyenberge, B. The design and verification of MuMax3. *AIP advances* **4**, 107133 (2014) (cit. on p. 47).
132. Hubert, A. & Schäfer, R. *Domain theory* 99–335 (Springer, 1998) (cit. on p. 47).
133. Albisetti, E., Calò, A., Spieser, M., Knoll, A. W., Riedo, E. & Petti, D. Stabilization and control of topological magnetic solitons via magnetic nanopatterning of exchange bias systems. *Applied Physics Letters* **113**, 162401 (2018) (cit. on p. 47).
134. Baltzis, K. The FEMM Package: A Simple, Fast, and Accurate Open Source Electromagnetic Tool in Science and Engineering. *Journal of Engineering Science & Technology Review* **1** (2008) (cit. on p. 51).
135. Körber, L., Wagner, K., Kákay, A. & Schultheiss, H. Spin-wave reciprocity in the presence of Néel walls. *IEEE Magnetics Letters* **8**, 1–4 (2017) (cit. on p. 51).

# List of abbreviation and symbols

BLS	Brillouin light scattering
BV	backward-volume mode
CCD	charge-coupled device
CMOS	complementary metal oxide semiconductor
DC	direct current
DE	Damon-Eshbach mode
DMI	Dzyaloshinskii-Moriya interaction
DW	domain wall
ECM	extracellular matrix
EOM	electro-optical modulator
FMR	ferromagnetic resonance
FPI	Fabry-Perot interferometer
FSR	free spectral range
MFM	magnetic force microscopy
RF	radio frequency
SD	single domain
SHNO	spin hall nano oscillators
TEM	transverse electromagnetic mode
TFPI	tandem Fabry-Perot interferometer
VIPA	virtually imaged phased array

# A. Matlab code for calculation of the dispersion relation

Here we present the Matlab code used for computing dispersion relation following the model introduced by Kalinikos and Slavin [26].

```
function [f] = slavinKalinikosDisp(kxi)
%Function for computing general dipolar-exchange dispersion relation
%according to Slavin-Kalinikos 86 with totally pinned boundary condition
%for the sake of your mental health, feel free to copy & paste.
%Everybody likes a good copy paste especially
%when you save a lot of your hair from going gray
% Kxi - wavevector in direction of propagation (along x) rad/m
% theta - out of plane vector (90 deg totaly inplane) - rad
% phi - in plane vector (90 deg - DE) - rad
% n - quantization in z direction (out of plane) - number of nodes
% d - thickness of film
% w0 - mu0*gamma*Hext
% wM - mu0*gamma*Ms
% A = Aex*2/(Ms^2*mu0)
% weff - effective width of waveguide
% to compute this number
% nT - quantization in waveguide direction - number of nodes
global d w0 wM A weff n nT theta phi;

k = sqrt(kxi.^2 + (n*pi./d).^2 + (nT*pi/weff)^2);
Pnm = (kxi.^2)./(k.^2) - (kxi.^2)./(k.^2).*(1 - exp(-k.*d))./(k.*d);
% Totally pinned surface spins

% Totally unpinned boundary condition
% if n == 0
%     Pnm = (kxi.^2)./(k.^2) - (kxi.^4)./(k.^4).*(1/2).*...
%     (2./(kxi.*d).*(1-exp(-kxi.*d)));
% else
%     Pnm = (kxi.^2)./(k.^2) - (kxi.^4)./(k.^4).*...
%     (2./(kxi.*d).*(1-exp(-kxi*d)));
% end

% Pnm = 1 - ((1 - exp(-k*d))./(k.*d));

% Pnm = (kxi.^2)./(k.^2) - (kxi.^2)/(k.^2).*(1 - exp(-k.*d))./(k.*d);
% Pnm(1) = 0;

% Long wave limit
% if n == 0
%     Pnm = kxi*d./2;
```

```

%     else
%         Pnn = (kxi*d).^2./(n^2*pi^2);
%     end

Fnn = Pnn + (sin(theta).^2).*(1-Pnn.*(1+(cos(phi).^2)) + ...
wM*(Pnn.*(1 - Pnn).*(sin(phi).^2))./(w0 + A*wM*(k.^2)));
f = sqrt((w0 + A*wM*(k.^2)).*(w0 + A*wM*(k.^2) + wM.*Fnn));
end

```

## B. Group velocity and lifetime of spin waves

This appendix present derived analytic expression used in Figure 1.4.

### B.1. Group velocities of spin waves

The group velocity of Damon-Eshbach mode

$$v_g^{\text{DE}} = \frac{\omega_M \exp(-2kt) \left( 2A^2 k^6 t^2 \omega_M \exp(2kt) + Ak^4 t^2 \exp(2kt) (2\omega_H + \omega_M) + \omega_M (\exp(kt)(kt - 2) + 2)^2 \right)}{k^3 t^2 \sqrt{(Ak^2 \omega_M + \omega_H) \left( \frac{\omega_M^2 \exp(-2kt) (\exp(kt) - 1) (\exp(kt)(kt - 1) + 1)}{k^2 t^2 (Ak^2 \omega_M + \omega_H)} + Ak^2 \omega_M + \omega_H + \omega_M \right)}}. \quad (\text{B.1})$$

The group velocity of backward-volume mode

$$v_g^{\text{BV}} = \frac{\omega_M e^{-kt} \left( \omega_H \left( e^{kt} (2Ak^3 t + kt - 2) + 2 \right) + Ak^2 \omega_M \left( e^{kt} (2Ak^3 t + kt - 1) + 1 \right) \right)}{k^2 t \sqrt{\frac{e^{-kt} (Ak^2 \omega_M + \omega_H) (e^{kt} (Ak^3 t \omega_M + kt \omega_H + \omega_M) - \omega_M)}{kt}}}. \quad (\text{B.2})$$

### B.2. Lifetime of spin waves

The lifetime of Damon-Eshbach mode is given by

$$\tau_{\text{DE}} = \frac{2}{2A\alpha k^2 \omega_M + 2\alpha \omega_H + \alpha \omega_M}. \quad (\text{B.3})$$

The lifetime of backward-volume mode is given by

$$\tau_{\text{BV}} = \frac{2kt \exp(kt)}{\alpha \exp(kt) (2kt (Ak^2 \omega_M + \omega_H) + \omega_M) - \alpha \omega_M}. \quad (\text{B.4})$$

## C. Dependency of group velocity, lifetime, and frequency of spin waves on thickness and external magnetic field

This appendix shows the calculated dependencies of the group velocity, lifetime and frequency on the thickness and the external magnetic field. The used parameters are same as in the section 1.5.1. The dependencies on thickness and external field are shown in Figure C.1, C.2 respectively.

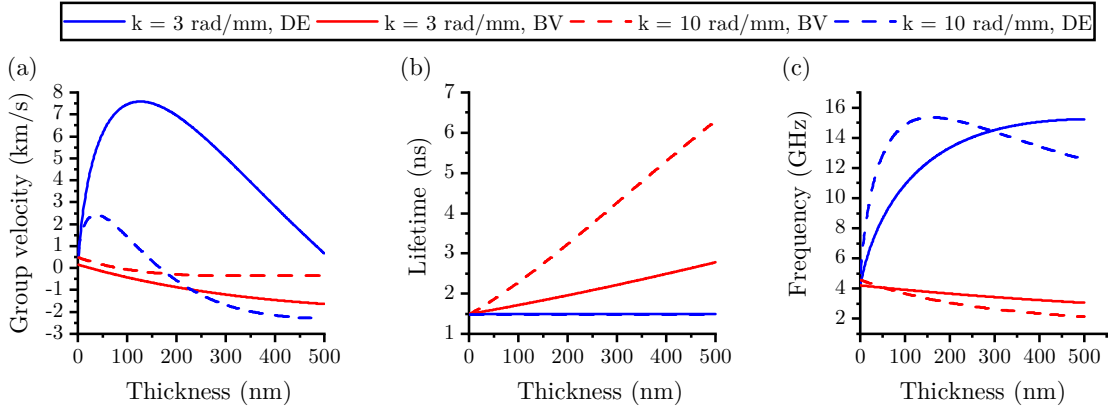


**Figure C.1:** Blue (red) curves show characteristics for spin waves with perpendicular (parallel)  $\vec{k}$  to the static magnetization. Solid (dashed) line shows  $k = 3 \frac{\text{rad}}{\mu\text{m}}$  ( $k = 10 \frac{\text{rad}}{\mu\text{m}}$ ). The dependence of the (a) group velocity, (b) lifetime, and (c) frequency on the thickness of the film. Other parameters are same as in Figure 1.4.

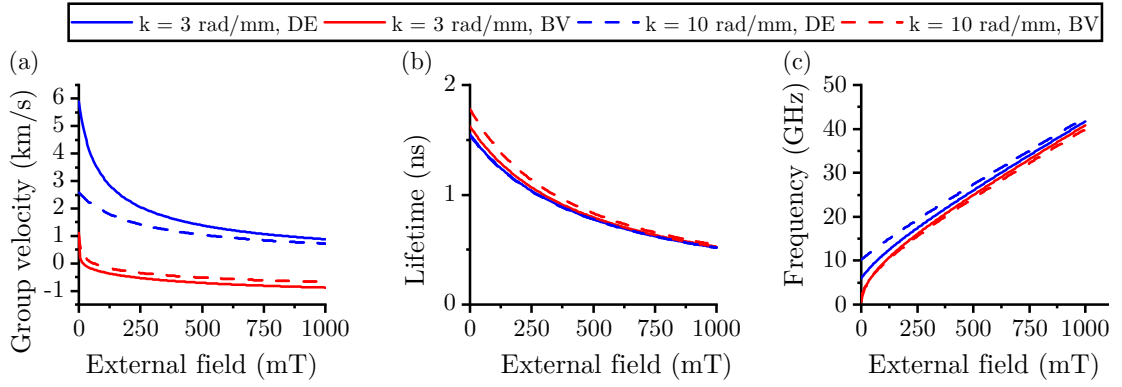


**Figure C.2:** Blue (red) curves show characteristics for spin waves with perpendicular (parallel)  $\vec{k}$  to the static magnetization. Solid (dashed) line shows  $k = 3 \frac{\text{rad}}{\mu\text{m}}$  ( $k = 10 \frac{\text{rad}}{\mu\text{m}}$ ). The dependence of the (a) group velocity, (b) lifetime, and (c) frequency on the external magnetic field. Other parameters are same as in Figure 1.4.

# D. Analytic modeling of phase resolved signals

This appendix consult the modeling of the signals shown in Figures 2.15 and 2.16.

## D.1. Signal without thermal background

These four signals ( $E, R, r_0$  and  $r_{\frac{\pi}{2}}$ ) were modeled as follows:

$$E = 1, \tag{D.1a}$$

$$R = 10\exp\left(-\frac{x}{l_{\text{att}}}\right), \tag{D.1b}$$

$$r_0 = E + R + 2\sqrt{E \cdot R} \cos\left(\pi\frac{x}{\lambda}\right), \tag{D.1c}$$

$$r_{\frac{\pi}{2}} = E + R + 2\sqrt{E \cdot R} \cos\left(\pi\frac{x}{\lambda} + \frac{\pi}{2}\right), \tag{D.1d}$$

where  $\lambda$  is a wavelength of modeled planar wave and was chosen as  $1 \mu\text{m}$  and  $l_{\text{att}}$  is attenuation length and was also chosen as  $1 \mu\text{m}$ .

## D.2. Signal with thermal background

These five signals ( $E, R, r_0, r_{\frac{\pi}{2}}$  and  $T$ ) were modeled as follows:

$$E = 1 + T_{\text{b}}, \tag{D.2a}$$

$$R = 10\exp\left(-\frac{x}{l_{\text{att}}}\right) + T_{\text{b}}, \tag{D.2b}$$

$$r_0 = E + T_{\text{b}} + R + 2\sqrt{E \cdot R} \cos\left(\pi\frac{x}{\lambda}\right), \tag{D.2c}$$

$$r_{\frac{\pi}{2}} = E + T_{\text{b}} + R + 2\sqrt{E \cdot R} \cos\left(\pi\frac{x}{\lambda} + \frac{\pi}{2}\right), \tag{D.2d}$$

$$T_{\text{b}} = 0.5. \tag{D.2e}$$

Constants were used same as is discussed in previous section. The thermal part of all signals were considered as incoherent, thus it does not contribute to interference.